Viscoelastic up-scaling rank-one effects in in-silico modelling of electro-active polymers

F. Marín[‡1], R. Ortigosa[†3], J. Martínez-Frutos[†2], A. J. Gil[‡4]

† *Computational Mechanics and Scientific Computing Group,*
Technical University of Cartagena, Campus Muralla del Mar, 30202, Cartagena (Murcia), Spain
‡ *Zienkiewicz Centre for Computational Engineering, Faculty of Science and Engineering*
Swansea University, Bay Campus, SA1 8EN, United Kingdom

Abstract

This paper analyses the viscoelastic up-scaling effects in electro-active polymers endowed with a micro-structure architecture in the form of a rank-one laminate. The principles of rank-n homogeneisation and thermodynamical consistency are combined in the context of extremely deformable dielectric elastomers actuated well beyond the onset of geometrical instabilities. To ensure the robustness of the resulting methodology, Convex Multi-Variable (CMV) energy density functionals enriched with a non-linear continuum viscoelastic description are used to describe the physics of the individual microscopic constituents. The high nonlinearity of the visco-electro-mechanical problem is resolved via a monolithic multi-scale Newton-Raphson scheme with a Backward-Euler (implicit) time integration scheme. A tensor cross product operation between vectors and tensors and an additive decomposition of the micro-scale deformation gradient (in terms of macro-scale and fluctuation components) are used to considerably reduce the complexity of the algebra. The resulting computational framework permits to explore the time-dependent in-silico analysis of rank-one electro-active polymer composites exhibiting extremely complex deformation patterns, paying particular attention to viscoelastic up-scaling effects. A comprehensive series of numerical examples is presented, where specially revealing conclusions about the rate-dependency of the composite electro-active polymer are observed as a function of its microstructure orientation and viscoelastic content. In a rectangular film subjected to extreme bending deformation, two different deformation modes are observed with one prevailing mode depending on the laminate composition. For the case of a square membrane where extreme deformation induces buckling, it is shown that the viscoelastic contribution leads to larger values of (stable) deformation, due to the regularisation that viscoelasticity inherently provides.

Keywords: viscoelasticity, finite element method, nonlinear electro-elasticity, rank-one laminates, electro-active polymer

1. Introduction

Electro-Active Polymers (EAPs) emerged as a class of smart materials capable of displaying significant change in shape in response to electrical stimuli. Among them, dielectric elastomers (DEs) are one of the most popular [52, 71, 72] due to their outstanding actuation capabilities (e.g. light weight, fast response time, flexibility, low stiffness properties). Among the numerous applications that they have, their use as soft robots [6, 7, 12, 15, 16, 49, 55, 66, 79] or flexible energy generators [50, 59] could be highlighted. Their potential drawback is that they generally require a large value of electric field to reach a significant deformation, which makes them susceptible to electromechanical instabilities or electrical breakdown [8].

[1]Corresponding author: francisco.marin@swansea.ac.uk
[2]Corresponding author: jesus.martinez@upct.es
[3]Corresponding author: rogelio.ortigosa@upct.es
[4]Corresponding author: a.j.gil@swansea.ac.uk

In order to reduce the necessary voltage applied to these DEs, composite designs have been introduced [30, 43, 44, 53, 65, 106] whose constituents are materials with distinct electromechanical properties; generally, one constituent is a soft elastomer with low permittivity whilst the other has opposite properties, so that it acts as a reinforcement [36, 74]. The improvement in the coupling performance of DE composites has been proved in [43, 90] experimentally, i.e., a smaller operational voltage is required in order to get the same actuation. Notwithstanding, in some cases the heterogeneous material may result weaker with respect to electric breakdown [51, 76].

A type of DE composites who has had an outstanding development in the past years is that of multi-layered DE laminated composites, specially due to the improvement in layer-by-layer fabrication techniques. To name but a few, Li et al. [53, 54] developed models which depict the strong non-linearity present in this kind of materials; deBotton [25] remarked the importance of the contrast betweeen properties of the constituents; Tian et al. [92] established the amplification that the performance of a composite can experiment while subjected to plane strain in the case of small deformations and electric fields; and Gei et al. [32] extended the work to the moderate strain regime, with an optimisation analysis in terms of the contrast and volume fractions of the constituents. Some authors study the onset of instabilities, e.g., Bertoldi and Gei [8] and Rudykh et al. [77, 78, 80] in rank-one DE laminated composites. A common feature of all of the above modelling studies lies in the search for closed-form solutions, which are achieved for the case of simple in-plane stretching deformation scenarios, primarily described by plane strain and exact incompressibility, in conjunction with the use of ideal dielectric neo-Hookean phases.

Nowadays, computational methods constructed on the basis of variational principles are used to simulate more complex deformation scenarios. From the theory stated in the early works of Toupin [93, 94] and the development performed by works such as [26, 27, 60, 91], there have been computational mechanics works developing it [28, 46, 96–99]. They all work with a single-phase material whose behaviour is modeled within a (phenomenologically) defined energy functional which depends upon appropriate strain measures, a Lagrangian electric variable and, if dissipative effects are considered, an electromechanical internal variable [56]. Other works important to mention are [47, 86, 88]. In previous publications [34, 67, 69, 70, 75], the authors put forward a new computational framework for single-phase reversible electro-mechanics, where the existence of solution is always ensured via the selection of objective (frame-invariant) and Convex Multi-Variable (CMV) energy functionals, that is, convex with respect to the minors of the deformation gradient tensor $\{\boldsymbol{F}, \boldsymbol{H}, J\}$, the Lagrangian electric displacement $\boldsymbol{D}_0$, and the spatial electric displacement $\boldsymbol{d} = \boldsymbol{F}\boldsymbol{D}_0$. CMV energy functionals (generally referred to as polyconvex [89]) guarantee ellipticity [34] in the quasi-static case and hyperbolicity in the dynamic case [67], thus precluding anomalous mesh dependency effects. In [58], the work was extended to laminated DE composites, where the individual constituents were modeled with CMV energy functionals.

All the works commented above are restricted to (reversible) hyperelastic material behaviour. However, dielectric elastomers can be rate dependent, and this can affect their coupling efficiency. The theory considering viscoelastic properties was first developed in [18, 37], and afterwards by [17, 73, 83]. In the past years, there have been works that consider a time-dependent behaviour in the deformation of DEs, both numerical [3, 13, 39, 62, 63, 87, 101, 102] and experimental [41, 42, 61, 63, 102, 104] studies. Restricted to finite strains, some works consider the electro-viscoelastic behaviour of the materials [2, 95, 100]: in [2], the numerical solution of some boundary value problems for a polyurethane-based dielectric elastomer; Vogel et al. [95] construct a general framework to model and simulate viscous electro-active materials, restricted also to finite strains; the author in [100] investigated creep and cyclic behaviours for a spring-connected dielectric actuator via a non-linear three-element viscoelastic model. Furthermore, Zhao et al. [107] and Hong [40] developed models for the electro-viscoelastic behaviour of dielectric elastomers at large deformations based on non-equilibrium thermodynamics. In [9], authors developed a coupled electro-viscoelastic model implemented into a commercial software. With respect to the characterization of the widely used dielectric elastomer VHB 4910, some studies show results under pure mechanical loading [1, 41] and electromechanical loading [9, 42, 63]. Other works calibrate some viscoelastic parameters [48, 102–104]. Out of the scope of this paper, some works study the electro-magneto-viscoelastic properties of some magnetorheological elastomers (MREs), for instance [31, 81, 82, 105]. In particular, Saxena et al. [81, 82] presented a general framework of finite deformation

magneto-vistoelasticity. Garcia [31] introduced a new framework to model time-dependent behaviour of MREs based on the multiplicative decomposition of deformation gradient tensor into elastic and viscous parts. To analyse thermo-electro-viscoelasticity of dielectrics, Mehnert et al. [62] developed a mathematical framework decomposing the free energy function into four parts: elastic, electric, time-dependent and thermal parts.

As a result, this paper will apply the principles of rank-n homogenisation of CMV phases in the context of extremely deformable dielectric elastomers actuated well beyond the onset of geometrical instabilities, with the consideration of viscoelasticity in the materials of the composite, adding further complexity and realism to that of the standard hyperelastic (reversible) incompressible ideal dielectric elastomer. From the numerical standpoint, a new computational framework takes into account the viscoelastic properties of the phases, and analyses their effect in the delayed response of deformation of the material. This contributes to a more realistic modeling of the materials, taking into account the effect of historic loading effects. Likewise, it facilitates numerical modelling, since viscous terms provide a regularising contribution. With this consideration, a next step could be to approach optimisation problems with realistic controls.

The outline of this paper is as follows. Section 2 describes the necessary elements of nonlinear continuum electro-mechanics. Section 3 revisits the concept of Multi-Variable Convexity as a basis for the constitutive models for the description of the individual microscopic components in multi-layered DE composites, and studies in depth the extension to the viscoelastic models. Section 4 presents the homogenisation theory applied to rank-one viscoelectro-mechanical laminates and demonstrates the necessary conditions of existence for the microscopic and macroscopic problems to be solved. Section 5 succinctly describes the variational principles and the finite element implementation method used in this work. Section 6 presents a series of numerical examples in order to assess the capabilities of the new computational framework. Specifically, in a first example, a local analysis is conducted at a quadrature (Gauss point) level where the effect of laminate orientation upon purely mechanical and electro-mechanical relaxation and loading/unloading tests is presented. In a second example, complex three-dimensional bending/torsion/stretching combined modes of deformation are studied for a soft robot actuator, monitoring macroscopic stability, and observing the effect that viscoelasticity has in the predominance of a deformation mode against others. This will be observed only when the material is subjected to extreme deformation as it is the case of the three-dimensional bending of a laminate. In a third example, the onset of first and second order buckling is explored in a prototypical laboratory configuration. In this, it is observed the regularising contribution provided by the time-dependent viscoelastic term, which allows to attain a much higher deformation without reaching the instabilities present in the hyperelastic case. Eventually, Section 7 provides some concluding remarks about the paper.

2. Nonlinear continuum electro-mechanics

2.1. Kinematics: motion and deformation

Let us consider the motion of an Electro-Active Polymer (EAP) with reference configuration given by the open bounded set $\mathcal{B}_0 \subset \mathbb{R}^3$ with boundary $\partial\mathcal{B}_0$ and unit outward normal $\boldsymbol{N}$. After the motion, the EAP occupies a deformed configuration given by the open bounded set $\mathcal{B} \subset \mathbb{R}^3$ with boundary $\partial\mathcal{B}$ and unit outward normal $\boldsymbol{n}$. The motion of the EAP is defined by a deformation mapping $\boldsymbol{\phi}$ linking material particles $\boldsymbol{X} \in \mathcal{B}_0$ to the deformed configuration $\boldsymbol{x} \in \mathcal{B}$ as

$$\begin{aligned} \boldsymbol{\phi} : \mathcal{B}_0 \subset \mathbb{R}^3 \times [0,T] &\to \mathcal{B} \subset \mathbb{R}^3 \\ \boldsymbol{X} &\mapsto \boldsymbol{x} = \boldsymbol{\phi}(\boldsymbol{X}, t)\,. \end{aligned} \tag{1}$$

This motion is represented in Figure 1. Associated with $\boldsymbol{\phi}(\boldsymbol{X})$, the deformation gradient tensor $\boldsymbol{F}$ [11, 21, 35] is defined as[5]

$$\boldsymbol{F} = \boldsymbol{\nabla}_0 \boldsymbol{\phi}(\boldsymbol{X})\,; \qquad F_{iI} = \frac{\partial \phi_i}{\partial X_I} = \partial_{X_I}(\phi_i). \tag{2}$$

[5]Lower case indices $\{i, j, k\}$ will be used to represent the spatial configuration, whereas capital case indices $\{I, J, K\}$ will be used to represent the material description.

Associated with $\boldsymbol{F}$, its co-factor $\boldsymbol{H}$ and its Jacobian J [10, 20] are defined as

$$\boldsymbol{H} = \frac{1}{2}\boldsymbol{F} \times \boldsymbol{F}; \qquad J = \frac{1}{3}\boldsymbol{H} : \boldsymbol{F}, \tag{3}$$

with $(\boldsymbol{A} \times \boldsymbol{B})_{iI} = \mathcal{E}_{ijk}\mathcal{E}_{IJK}A_{jJ}B_{kK}$, $\forall \boldsymbol{A}, \boldsymbol{B} \in \mathbb{R}^{3\times 3}$, where $\mathcal{E}_{ijk}$ (or $\mathcal{E}_{IJK}$) symbolises the third-order alternating tensor components and the use of repeated indices implies summation[6].

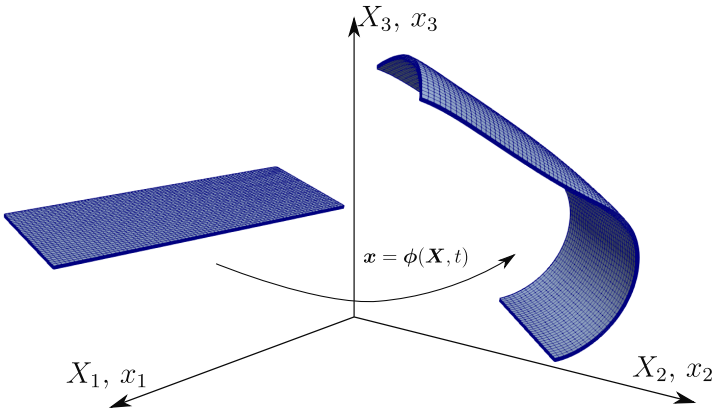

Figure 1: Deformation mapping $\boldsymbol{\phi}(\boldsymbol{X}, t)$.

The directional derivative of the deformation gradient tensor $\boldsymbol{F}$ with respect to vector fields $\delta\boldsymbol{x} \in \mathbb{R}^3$ can be obtained as

$$D\boldsymbol{F}[\delta\boldsymbol{x}] = \boldsymbol{\nabla}_0 \delta\boldsymbol{x}. \tag{4}$$

Using the notation $\delta\boldsymbol{F} := D\boldsymbol{F}[\delta\boldsymbol{x}]$, the directional derivative of the co-factor matrix $\boldsymbol{H} = \boldsymbol{H}(\boldsymbol{F})$ and of the determinant $J = J(\boldsymbol{F})$ with respect to tensor fields $\delta\boldsymbol{F} \in \mathbb{R}^{3\times 3}$ follow from their definitions in (3), i.e.,

$$D\boldsymbol{H}[\delta\boldsymbol{F}] = \boldsymbol{F} \times \delta\boldsymbol{F}; \qquad DJ[\delta\boldsymbol{F}] = \boldsymbol{H} : \delta\boldsymbol{F}. \tag{5}$$

Similarly, second directional derivatives of both $\boldsymbol{H}$ and J with respect to tensor fields $\delta\boldsymbol{F} \in \mathbb{R}^{3\times 3}$ yield

$$D^2\boldsymbol{H}[\delta\boldsymbol{F}; \delta\boldsymbol{F}] = \delta\boldsymbol{F} \times \delta\boldsymbol{F}; \qquad D^2 J[\delta\boldsymbol{F}; \delta\boldsymbol{F}] = \boldsymbol{F} : (\delta\boldsymbol{F} \times \delta\boldsymbol{F}). \tag{6}$$

2.2. Governing equations in nonlinear electromechanics

In the absence of inertia[7] and magnetic effects, the system of partial differential equations governing the behaviour of the EAP comprises the conservation of linear momentum and the compatibility equation $(2)_a$ along with the quasi-static version of the Gauss's and Faraday's laws. The complete Initial Boundary Value problem can be recast in a Total Lagrangian formalism as

$$\underbrace{\begin{aligned} \boldsymbol{F} &= \boldsymbol{\nabla}_0 \boldsymbol{\phi}; && \text{in } \mathcal{B}_0 \times [0,T]; \\ \mathrm{DIV}\boldsymbol{P} + \boldsymbol{f}_0 &= \boldsymbol{0}; && \text{in } \mathcal{B}_0 \times [0,T]; \\ \boldsymbol{P}\boldsymbol{N} &= \boldsymbol{t}_0; && \text{on } \partial_{\boldsymbol{t}}\mathcal{B}_0 \times [0,T]; \\ \boldsymbol{\phi} &= \bar{\boldsymbol{\phi}}; && \text{on } \partial_{\boldsymbol{\phi}}\mathcal{B}_0 \times [0,T]; \end{aligned}}_{\text{Conservation of linear momentum and kinematics}} \qquad \underbrace{\begin{aligned} \boldsymbol{E}_0 &= -\boldsymbol{\nabla}_0 \varphi; && \text{in } \mathcal{B}_0 \times [0,T]; \\ \mathrm{DIV}\boldsymbol{D}_0 - \rho_0 &= 0; && \text{in } \mathcal{B}_0 \times [0,T]; \\ \boldsymbol{D}_0 \cdot \boldsymbol{N} &= -\omega_0; && \text{on } \partial_{\omega}\mathcal{B}_0 \times [0,T]; \\ \varphi &= \bar{\varphi}; && \text{on } \partial_{\varphi}\mathcal{B}_0 \times [0,T], \end{aligned}}_{\text{Gauss and Faraday laws}} \tag{7}$$

where $\boldsymbol{f}_0$ represents a body force per unit undeformed volume $\mathcal{B}_0$; $\boldsymbol{t}_0$, the traction force per unit undeformed area on $\partial_{\boldsymbol{t}}\mathcal{B}_0 \subset \partial\mathcal{B}_0$; $\bar{\boldsymbol{\phi}}$, the value of the Dirichlet boundary condition on $\partial_{\boldsymbol{\phi}}\mathcal{B}_0 \subset \partial\mathcal{B}_0$, with $\partial_{\boldsymbol{t}}\mathcal{B}_0 \cup \partial_{\boldsymbol{\phi}}\mathcal{B}_0 = \partial\mathcal{B}_0$ and $\partial_{\boldsymbol{t}}\mathcal{B}_0 \cap \partial_{\boldsymbol{\phi}}\mathcal{B}_0 = \emptyset$. Furthermore, ρ_0 represents an electric volume charge per unit

[6] In addition, throughout the paper, the symbol $(\cdot)$ indicates the scalar product or contraction of a single index $\boldsymbol{a}\cdot\boldsymbol{b} = a_i b_i$; the symbol $(:)$, double contraction of two indices $\boldsymbol{A} : \boldsymbol{B} = A_{ij}B_{ij}$; the symbol $(\times)$, the cross product between vectors $(\boldsymbol{a} \times \boldsymbol{b})_i = \mathcal{E}_{ijk}a_j b_k$; and the symbol $(\otimes)$, the outer or dyadic product $(\boldsymbol{a} \otimes \boldsymbol{b})_{ij} = a_i b_j$.

[7] Although other time-dependent effects, such as viscoelasticity, will be present.

of undeformed volume $\mathcal{B}_0$; and ω_0, an electric surface charge per unit of undeformed area $\partial_\omega\mathcal{B}_0 \subset \partial\mathcal{B}_0$. In addition, $\boldsymbol{E}_0$ is the Lagrangian electric field vector; $\varphi : \mathcal{B}_0 \times [0,T] \to \mathbb{R}$, the scalar electric potential; and $\partial_\varphi\mathcal{B}_0$, the part of the boundary $\partial\mathcal{B}_0$ where essential electric potential boundary conditions are applied so that $\partial_\omega\mathcal{B}_0 \cup \partial_\varphi\mathcal{B}_0 = \partial\mathcal{B}_0$ and $\partial_\omega\mathcal{B}_0 \cap \partial_\varphi\mathcal{B}_0 = \emptyset$. Finally, $\boldsymbol{P}$ and $\boldsymbol{D}_0$ represent the first Piola-Kirchhoff stress tensor and the Lagrangian electric displacement field, respectively, which, in the reversible case, depend upon $\boldsymbol{F}$ and $\boldsymbol{E}_0$.

3. Constitutive equations in nonlinear electro-visco-elasticity: phenomenological macroscopic models

The scope of this paper is on analytical homogenisation of layered EAP composites. However, we devote the current section to the simpler case where a macroscopic phenomenological visco-electromechanical model is available, in order to introduce some key concepts which will be exploited in subsequent sections.

3.1. Constitutive framework in visco-electro-elasticity

In the case of visco-electro-elasticity, the internal energy density e per unit of undeformed volume can be defined in terms of the deformation, the electric displacement field and the strain-like tensorial internal variables, namely $e = e(\boldsymbol{F}, \boldsymbol{D}_0, \boldsymbol{\mathcal{A}})$, where $\boldsymbol{\mathcal{A}} = \{\boldsymbol{A}_1, \ldots, \boldsymbol{A}_{n_{\text{Maxw}}}\}$ represent the collection of internal variables $\boldsymbol{A}_i$, $i = 1, \cdots, n_{\text{Maxw}}$, and n_{Maxw} the number of Maxwell branches used to model the viscoelastic behaviour of the material [57, 64][8]. Furthermore, an additive decomposition of the energy density $e(\boldsymbol{F}, \boldsymbol{D}_0, \boldsymbol{\mathcal{A}})$ into a hyperelastic and a viscoelastic contribution is considered, as

$$e\left(\boldsymbol{F}, \boldsymbol{D}_0, \boldsymbol{\mathcal{A}}\right) = e^h\left(\boldsymbol{F}, \boldsymbol{D}_0\right) + e^v\left(\boldsymbol{F}, \boldsymbol{\mathcal{A}}\right). \tag{9}$$

In this work, as in others (e.g., [9, 57]), the viscous part of the internal energy is considered independent on the electric displacement field $\boldsymbol{D}_0$, as it can be deduced from equation (9). Using thermodynamical principles, the dissipation inequality $\mathcal{D}$ in the context of visco-electro-elasticity can be written as

$$\mathcal{D} = \underbrace{\boldsymbol{P} : \dot{\boldsymbol{F}} + \boldsymbol{E}_0 \cdot \dot{\boldsymbol{D}}_0}_{\mathcal{D}_{\text{int}}} - \dot{e} \geq 0, \tag{10}$$

where the time derivative of the energy density function $e(\boldsymbol{F}, \boldsymbol{D}_0, \boldsymbol{\mathcal{A}})$ is computed as

$$\dot{e} = \partial_{\boldsymbol{F}} e : \dot{\boldsymbol{F}} + \partial_{\boldsymbol{D}_0} e^h \cdot \dot{\boldsymbol{D}}_0 + \partial_{\boldsymbol{\mathcal{A}}} e^v \bullet \dot{\boldsymbol{\mathcal{A}}}, \tag{11}$$

where $(\dot{\bullet})$ denotes the time derivative of $(\bullet)$; $\partial_{\boldsymbol{B}}(\bullet)$, the partial derivative of $(\bullet)$ with respect to the field $\boldsymbol{B}$; and given $\boldsymbol{\mathcal{B}} = \{\boldsymbol{B}_1, \cdots, \boldsymbol{B}_n\}$, $\boldsymbol{\mathcal{C}} = \{\boldsymbol{C}_1, \cdots, \boldsymbol{C}_n\}$, the inner product $\boldsymbol{\mathcal{B}} \bullet \boldsymbol{\mathcal{C}}$ is defined as $\boldsymbol{\mathcal{B}} \bullet \boldsymbol{\mathcal{C}} = \sum_{i=1}^n \boldsymbol{B}_i : \boldsymbol{C}_i$. Use of the Coleman and Noll procedure in (10) and (11) (see [19]) yields the following standard constitutive equations,

$$\boldsymbol{P}(\boldsymbol{F}, \boldsymbol{D}_0, \boldsymbol{\mathcal{A}}) = \underbrace{\partial_{\boldsymbol{F}} e^h(\boldsymbol{F}, \boldsymbol{D}_0)}_{\boldsymbol{P}^h(\boldsymbol{F}, \boldsymbol{D}_0)} + \underbrace{\partial_{\boldsymbol{F}} e^v(\boldsymbol{F}, \boldsymbol{\mathcal{A}})}_{\boldsymbol{P}^v(\boldsymbol{F}, \boldsymbol{\mathcal{A}})}; \qquad \boldsymbol{E}_0(\boldsymbol{F}, \boldsymbol{D}_0) = \partial_{\boldsymbol{D}_0} e^h(\boldsymbol{F}, \boldsymbol{D}_0), \tag{12}$$

with the dissipation inequality given by

$$\mathcal{D}(\boldsymbol{F}, \boldsymbol{\mathcal{A}}, \dot{\boldsymbol{\mathcal{A}}}) = -\partial_{\boldsymbol{\mathcal{A}}} e^v(\boldsymbol{F}, \boldsymbol{\mathcal{A}}) \bullet \dot{\boldsymbol{\mathcal{A}}} \geq 0. \tag{13}$$

In addition to the strain energy density $e\left(\boldsymbol{F}, \boldsymbol{D}_0, \boldsymbol{\mathcal{A}}\right)$ in equation (9), the constitutive model must be endowed with a suitable definition of evolution equations, typically, first-order ordinary differential equations that determine the time evolution of the internal variables $\boldsymbol{A}_i$ as an implicit function of the

[8] The requirement of objectivity implies that the internal energy density $e(\boldsymbol{F}, \boldsymbol{D}_0, \boldsymbol{\mathcal{A}})$ can be re-expressed in terms of a set of objective arguments (namely, $\boldsymbol{D}_0$ and $\boldsymbol{C} = \boldsymbol{F}^T\boldsymbol{F}$) as

$$e\left(\boldsymbol{F}, \boldsymbol{D}_0, \boldsymbol{\mathcal{A}}\right) = \widetilde{e}\left(\boldsymbol{C}, \boldsymbol{D}_0, \boldsymbol{\mathcal{A}}\right), \tag{8}$$

where e and $\widetilde{e}$ denote alternative representations of the same internal energy density.

deformation $\boldsymbol{F}$ at each material point $\boldsymbol{X}$ and at any time instant t (namely, $\boldsymbol{A}_i = \boldsymbol{A}_i(\boldsymbol{F}(\boldsymbol{X},t))$), whilst complying with the dissipation inequality in equation (13) . Mathematically, these evolution equations can be generically recast as

$$\begin{aligned} &\boldsymbol{\mathcal{F}}_i : \mathbb{R}^{3\times3} \times \mathbb{R}^{3\times3} \times \mathbb{R}^{3\times3} \to \mathbb{R}^{3\times3}; && i = 1, \dots, n_{\text{Maxw}}; \\ &\dot{\boldsymbol{A}}_i = \boldsymbol{\mathcal{F}}_i\left(\boldsymbol{F}(\boldsymbol{X},t), \boldsymbol{A}_i\right); && \\ &\boldsymbol{A}_i = \boldsymbol{I}; && t = 0. \end{aligned} \tag{14}$$

3.2. Tangent operator

Linearisation of $\mathcal{D}_{\text{int}}$ with respect to $\delta\boldsymbol{F}$ and $\delta\boldsymbol{D}_0$ in (10) yields the high order constitutive tensors, necessary for any Newton-Raphson type of computational implementation. With that in mind, the time derivatives $\dot{\boldsymbol{F}}$ and $\dot{\boldsymbol{D}}_0$ are first replaced with virtual variations $\delta\boldsymbol{F}$ and $\delta\boldsymbol{D}_0$, respectively, and $\mathcal{D}_{\text{int}}$ is further decomposed into its hyperelastic and viscous contribution, $\mathcal{D}^h_{\text{int}}$ and $\mathcal{D}^v_{\text{int}}$, respectively, as

$$\mathcal{D}_{\text{int}}(\boldsymbol{F}, \boldsymbol{D}_0, \boldsymbol{\mathcal{A}}, \delta\boldsymbol{F}, \delta\boldsymbol{D}_0) = \mathcal{D}^h_{\text{int}}(\boldsymbol{F}, \boldsymbol{D}_0, \delta\boldsymbol{F}, \delta\boldsymbol{D}_0) + \mathcal{D}^v_{\text{int}}(\boldsymbol{F}, \boldsymbol{\mathcal{A}}, \delta\boldsymbol{F}), \tag{15}$$

where $\mathcal{D}^h_{\text{int}}$ and $\mathcal{D}^v_{\text{int}}$ are expressed as

$$\begin{aligned} \mathcal{D}^h_{\text{int}}(\boldsymbol{F}, \boldsymbol{D}_0, \delta\boldsymbol{F}, \delta\boldsymbol{D}_0) &= De^h(\boldsymbol{F}, \boldsymbol{D}_0)[\delta\boldsymbol{F}, \delta\boldsymbol{D}_0] = \boldsymbol{P}^h(\boldsymbol{F}, \boldsymbol{D}_0) : \delta\boldsymbol{F} + \boldsymbol{E}_0(\boldsymbol{F}, \boldsymbol{D}_0) \cdot \delta\boldsymbol{D}_0; \\ \mathcal{D}^v_{\text{int}}\left(\boldsymbol{F}, \boldsymbol{\mathcal{A}}, \delta\boldsymbol{F}\right) &= \boldsymbol{P}^v(\boldsymbol{F}, \boldsymbol{\mathcal{A}}) : \delta\boldsymbol{F}. \end{aligned} \tag{16}$$

It is important to notice that the hyperelastic contribution $\mathcal{D}^h_{\text{int}}(\boldsymbol{F}, \boldsymbol{D}_0, \delta\boldsymbol{F}, \delta\boldsymbol{D}_0)$ is equivalent to the linearisation of the hyperelastic energy density functional $e^h\left(\boldsymbol{F}, \boldsymbol{D}_0\right)$ with respect to $\delta\boldsymbol{F}$ and $\delta\boldsymbol{D}_0$, whereas $\mathcal{D}^v_{\text{int}}\left(\boldsymbol{F}, \boldsymbol{\mathcal{A}}, \delta\boldsymbol{F}\right)$ cannot be analogously understood due to the presence of the internal variables $\boldsymbol{\mathcal{A}}$ (irreversibility), which gives an implicit relationships between $\boldsymbol{\mathcal{A}}$ and $\boldsymbol{F}$. Indeed, the linearisation of both $\mathcal{D}^h_{\text{int}}\left(\boldsymbol{F}, \boldsymbol{D}_0, \delta\boldsymbol{F}, \delta\boldsymbol{D}_0\right)$ and $\mathcal{D}^v_{\text{int}}\left(\boldsymbol{F}, \boldsymbol{\mathcal{A}}, \delta\boldsymbol{F}\right)$ in (16) can be expressed as

$$\begin{aligned} D\mathcal{D}^h_{\text{int}}[\delta\boldsymbol{F}, \delta\boldsymbol{D}_0] &= D\Big(\boldsymbol{P}^h(\boldsymbol{F}, \boldsymbol{D}_0) : \delta\boldsymbol{F} + \boldsymbol{E}_0(\boldsymbol{F}, \boldsymbol{D}_0) \cdot \delta\boldsymbol{D}_0\Big)[\delta\boldsymbol{F}, \delta\boldsymbol{D}_0]; \\ D\mathcal{D}^v_{\text{int}}[\delta\boldsymbol{F}, \delta\boldsymbol{D}_0] &= D\Big(\boldsymbol{P}^v\big(\boldsymbol{F}, \boldsymbol{\mathcal{A}}(\boldsymbol{F})\big) : \delta\boldsymbol{F}\Big)[\delta\boldsymbol{F}, \delta\boldsymbol{D}_0], \end{aligned} \tag{17}$$

where the implicit dependence of $\boldsymbol{\mathcal{A}}$ and $\boldsymbol{F}$ is stated. Thus,

$$\begin{aligned} D\mathcal{D}^h_{\text{int}}[\delta\boldsymbol{F}, \delta\boldsymbol{D}_0] &= \delta\boldsymbol{F} : \underbrace{\partial_{\boldsymbol{F}}\boldsymbol{P}^h : \delta\boldsymbol{F}}_{D\boldsymbol{P}^h[\delta\boldsymbol{F}]} + \delta\boldsymbol{F} : \underbrace{\partial_{\boldsymbol{D}_0}\boldsymbol{P}^h \cdot \delta\boldsymbol{D}_0}_{D\boldsymbol{P}^h[\delta\boldsymbol{D}_0]} + \delta\boldsymbol{D}_0 \cdot \underbrace{\partial_{\boldsymbol{F}}\boldsymbol{E}_0 : \delta\boldsymbol{F}}_{D\boldsymbol{E}_0[\delta\boldsymbol{F}]} + \delta\boldsymbol{D}_0 \cdot \underbrace{\partial_{\boldsymbol{D}_0}\boldsymbol{E}_0\delta\boldsymbol{D}_0}_{D\boldsymbol{E}_0[\delta\boldsymbol{D}_0]}; \\ D\mathcal{D}^v_{\text{int}}[\delta\boldsymbol{F}, \delta\boldsymbol{D}_0] &= \delta\boldsymbol{F} : \underbrace{\left(\partial_{\boldsymbol{F}}\boldsymbol{P}^v + \partial_{\boldsymbol{\mathcal{A}}}\boldsymbol{P}^v \bullet \partial_{\boldsymbol{F}}\boldsymbol{\mathcal{A}}\right) : \delta\boldsymbol{F}}_{D\boldsymbol{P}^v[\delta\boldsymbol{F}]} \end{aligned} \tag{18}$$

Above equations in (18) can be carefully re-written in the following equivalent form

$$\begin{aligned} &D\mathcal{D}^h_{\text{int}}[\delta\boldsymbol{F}, \delta\boldsymbol{D}_0] = [\delta\boldsymbol{F} : \delta\boldsymbol{D}_0 \cdot] \left[\mathbb{H}^h_e\right] \begin{bmatrix} : \delta\boldsymbol{F} \\ \delta\boldsymbol{D}_0 \end{bmatrix}; && \left[\mathbb{H}^h_e\right] = \begin{bmatrix} \boldsymbol{\mathcal{C}}^h_e & \boldsymbol{\mathcal{Q}}^T \\ \boldsymbol{\mathcal{Q}} & \boldsymbol{\theta} \end{bmatrix}; && \left(\boldsymbol{\mathcal{Q}}^T\right)_{jJI} = (\boldsymbol{\mathcal{Q}})_{IjJ}; \\ &D\mathcal{D}^v_{\text{int}}[\delta\boldsymbol{F}, \delta\boldsymbol{D}_0] = [\delta\boldsymbol{F} : \delta\boldsymbol{D}_0 \cdot] \left[\mathbb{H}^v_e\right] \begin{bmatrix} : \delta\boldsymbol{F} \\ \delta\boldsymbol{D}_0 \end{bmatrix}; && \left[\mathbb{H}^v_e\right] = \begin{bmatrix} \boldsymbol{\mathcal{C}}^v_e & \boldsymbol{0} \\ \boldsymbol{0} & \boldsymbol{0} \end{bmatrix}, && \end{aligned} \tag{19}$$

where $\left[\mathbb{H}^h_e\right]$ includes the hyperelastic high order constitutive tensors, namely the fourth order elasticity tensor $\boldsymbol{\mathcal{C}}^h_e \in \mathbb{R}^{3\times3\times3\times3}$, the third order piezoelectric tensor $\boldsymbol{\mathcal{Q}} \in \mathbb{R}^{3\times3\times3}$ and the inverse of the dielectric tensor $\boldsymbol{\theta} \in \mathbb{R}^{3\times3}$, whilst $\left[\mathbb{H}^v_e\right]$ includes the viscous contribution in the elasticity tensor $\boldsymbol{\mathcal{C}}^v_e \in \mathbb{R}^{3\times3\times3\times3}$, being all of them defined as

$$\begin{aligned} \boldsymbol{\mathcal{C}}^h_e(\boldsymbol{F}, \boldsymbol{D}_0) &:= \partial_{\boldsymbol{F}}\boldsymbol{P}^h = \partial^2_{\boldsymbol{F}\boldsymbol{F}}e^h; & \boldsymbol{\mathcal{C}}^v_e(\boldsymbol{F}, \boldsymbol{\mathcal{A}}) &:= \partial_{\boldsymbol{F}}\boldsymbol{P}^v + \partial_{\boldsymbol{\mathcal{A}}}\boldsymbol{P}^v \bullet \partial_{\boldsymbol{F}}\boldsymbol{\mathcal{A}} = \partial^2_{\boldsymbol{F}\boldsymbol{F}}e^v + \partial^2_{\boldsymbol{F}\boldsymbol{\mathcal{A}}}e^v \bullet \partial_{\boldsymbol{F}}\boldsymbol{\mathcal{A}}; \\ \boldsymbol{\mathcal{Q}}(\boldsymbol{F}, \boldsymbol{D}_0) &:= \partial_{\boldsymbol{F}}\boldsymbol{E}_0 = \partial^2_{\boldsymbol{D}_0\boldsymbol{F}}e^h; & \boldsymbol{\theta}(\boldsymbol{F}, \boldsymbol{D}_0) &:= \partial_{\boldsymbol{D}_0}\boldsymbol{E}_0 = \partial^2_{\boldsymbol{D}_0\boldsymbol{D}_0}e^h, \end{aligned} \tag{20}$$

Finally, addition of both $D\mathcal{D}^h_{\text{int}}[\delta\boldsymbol{F}, \delta\boldsymbol{D}_0]$ and $D\mathcal{D}^v_{\text{int}}[\delta\boldsymbol{F}, \delta\boldsymbol{D}_0]$ in (19), permits to obtain the linearisation of the dissipation inequality $D\mathcal{D}_{\text{int}}[\delta\boldsymbol{F}, \delta\boldsymbol{D}_0]$ as

$$D\mathcal{D}_{\text{int}}[\delta\boldsymbol{F}, \delta\boldsymbol{D}_0] = [\delta\boldsymbol{F} : \delta\boldsymbol{D}_0 \cdot] \left[\mathbb{H}_e\right] \begin{bmatrix} : \delta\boldsymbol{F} \\ \delta\boldsymbol{D}_0 \end{bmatrix}; \qquad \left[\mathbb{H}_e\right] = \left[\mathbb{H}^h_e\right] + \left[\mathbb{H}^v_e\right]. \tag{21}$$

3.3. Specific form of the hyperelastic and viscous contributions and of the evolution laws for internal variables

In order to ensure existence of solutions for problem (7) in the vicinity of the origin, namely when $\boldsymbol{F} \approx \boldsymbol{I}$ (with $\boldsymbol{I}$ the second order identity matrix), $\boldsymbol{D}_0 \approx \boldsymbol{0}$ and $\boldsymbol{\mathcal{A}} \approx \boldsymbol{I}$[9], the directional derivative $D\mathcal{D}_{\text{int}}[\delta\boldsymbol{F}, \delta\boldsymbol{D}_0]$ in (21) must be strictly positive, namely

$$D\mathcal{D}_{\text{int}}[\delta\boldsymbol{F}, \delta\boldsymbol{D}_0]|_{\boldsymbol{F}=\boldsymbol{I},\boldsymbol{D}_0=\boldsymbol{0},\boldsymbol{\mathcal{A}}=\boldsymbol{I}} > 0; \qquad \forall\, \delta\boldsymbol{F}, \delta\boldsymbol{D}_0, \tag{22}$$

which requires positive definiteness of $[\mathbb{H}_e]$. However, positive definiteness of $[\mathbb{H}_e]$ (entailing uniqueness of such solutions) is not a physical restriction away from the origin as it precludes buckling, inherent to soft dielectric materials. Therefore, more physically realistic restrictions than that in (22) need to be imposed on the constitutive model of viscoelastic electro-active materials. Working on this idea, but in the context of reversible nonlinear electro-mechanics (i.e., no viscoelastic behaviour considered), Gil and Ortigosa [34, 67, 68, 70], motivated by considerations of material stability, extended the concept of polyconvexity [4, 5, 45, 84, 85] from elasticity to electro-magneto-elasticity and proposed new convexity restrictions on the (hyperelastic) internal energy density $e^h(\boldsymbol{F}, \boldsymbol{D}_0)$, postulating a Convex Multi-Variable (CMV) definition as

$$e^h\left(\boldsymbol{F}, \boldsymbol{D}_0\right) = W^h\left(\boldsymbol{\mathcal{V}}\right); \qquad \boldsymbol{\mathcal{V}} = \{\boldsymbol{F}, \boldsymbol{H}, J, \boldsymbol{D}_0, \boldsymbol{d}\}; \qquad \boldsymbol{d} = \boldsymbol{F}\boldsymbol{D}_0, \tag{23}$$

where W^h must be a convex function with respect to the extended set $\boldsymbol{\mathcal{V}}$. The new extended set of convex restrictions proved to be a sufficient condition for the satisfaction of the ellipticity condition [34]. Shortly after the work in [34], Šilhavý [89] proved that multi-variable convexity, or $\mathcal{A}$-polyconvexity, as he denoted it in his work, in conjunction with suitable growth conditions, ensures existence of minimisers in (reversible) nonlinear electro-magneto-elasticity.

In this work, we advocate for a convex multi-variable definition of the hyperelastic contribution $e^h\left(\boldsymbol{F}, \boldsymbol{D}_0\right)$, additively decomposed into its purely mechanical and electromechanical contributions [14, 45, 96], $e^h_m\left(\boldsymbol{F}\right)$ and $e^h_{em}\left(\boldsymbol{F}, \boldsymbol{D}_0\right)$, respectively, both complying with the definition of multi-variable convexity, namely

$$e^h\left(\boldsymbol{F}, \boldsymbol{D}_0\right) = e^h_m\left(\boldsymbol{F}\right) + e^h_{em}\left(\boldsymbol{F}, \boldsymbol{D}_0\right); \qquad e^h_m(\boldsymbol{F}) = W^h_m(\boldsymbol{F}, \boldsymbol{H}, J); \qquad e^h_{em}(\boldsymbol{F}, \boldsymbol{D}_0) = W^h_{em}(\boldsymbol{\mathcal{V}}), \tag{24}$$

where $W^h_m(\boldsymbol{F}, \boldsymbol{H}, J)$ and $W^h_{em}(\boldsymbol{\mathcal{V}})$ are convex functions with respect to their arguments. For the purely mechanical contribution $e_m(\boldsymbol{F})$, different models can be considered. A possible example includes the polyconvex Mooney-Rivlin model, i.e.,

$$e^h_m\left(\boldsymbol{F}\right) = W^h_m(\boldsymbol{F}, \boldsymbol{H}, J) = \frac{\mu_1}{2} II_{\boldsymbol{F}} + \frac{\mu_2}{2} II_{\boldsymbol{H}} + U(J); \qquad U(J) = -\left(\mu_1 + 2\mu_2\right) \ln J + \frac{\lambda}{2}\left(J-1\right)^2, \tag{25}$$

where $\{\mu_1, \mu_2, \lambda\}$ are material parameters, with units of stress, related to the shear modulus μ_0 and the bulk modulus λ_0 in the origin as $\mu_0 = \mu_1 + \mu_2$ and $\lambda_0 = \lambda + 2\mu_2$. With regards to the electro-mechanical contribution $e_{em}\left(\boldsymbol{F}, \boldsymbol{D}_0\right)$, the simplest expression corresponds with that of an ideal dielectric elastomer, convex with respect to $\{J, \boldsymbol{d}\}$, defined as

$$e^h_{em}\left(\boldsymbol{F}, \boldsymbol{D}_0\right) = \mathbb{W}^h_{em}\left(J, \boldsymbol{d}\right) = \frac{1}{2\epsilon_r\epsilon_0 J} II_{\boldsymbol{d}}; \qquad II_{\boldsymbol{d}} = \boldsymbol{d}\cdot\boldsymbol{d}, \tag{26}$$

where ϵ_0 represents the vacuum permittivity, with $\epsilon_0 = 8.8541 \times 10^{-12}\,\text{C}^2\text{N}^{-1}\text{m}^{-2}$ and ϵ_r, the relative permittivity. An alternative convex multi-variable electro-mechanical contribution, convex with respect to $\{J, \boldsymbol{D}_0, \boldsymbol{d}\}$, can be defined as

$$e^h_{em}\left(\boldsymbol{F}, \boldsymbol{D}_0\right) = W^h_{em}\left(J, \boldsymbol{d}, \boldsymbol{D}_0\right) = \frac{1}{2\epsilon_1 J^\alpha} II_{\boldsymbol{d}} + \frac{1}{2\epsilon_2 J^\alpha} II_{\boldsymbol{D}_0}; \qquad \alpha \in (0, 1], \tag{27}$$

[9] Strictly speaking, the condition on $\boldsymbol{\mathcal{A}}$ in the origin is correctly written as $\boldsymbol{\mathcal{A}} = \{\boldsymbol{A}_1, \boldsymbol{A}_2, \ldots, \boldsymbol{A}_{\text{n}_{\text{Maxw}}}\} = \{\boldsymbol{I}, \boldsymbol{I}, \ldots, \boldsymbol{I}\}$.

with $\{\epsilon_1, \epsilon_2\}$ material parameters with units of electric permittivity. Finally, with regards to the viscous contribution $e_v(\boldsymbol{F}, \boldsymbol{\mathcal{A}})$, the model followed in this paper is that in References [38, 57]:

$$e^v(\boldsymbol{F}, \boldsymbol{\mathcal{A}}) = \sum_{i=1}^{n_{\text{Maxw}}} \frac{\mu_i^v}{2}\left(\hat{\boldsymbol{C}} : \boldsymbol{A}_i - 3 - \ln\left(\det\left(\boldsymbol{A}_i\right)\right)\right); \qquad \hat{\boldsymbol{C}} = J^{-2/3}\boldsymbol{F}^T\boldsymbol{F}; \qquad i = 1, \cdots, n_{\text{Maxw}}, \tag{28}$$

where $\left\{\mu_1^v, \cdots, \mu_{n_{\text{Maxw}}}^v\right\}$ represent the viscous shear moduli associated with the viscous Maxwell branches. The specific form of the evolution equations of the strain-like internal variables [38, 57] in (14) is:

$$\begin{aligned} &\dot{\boldsymbol{A}}_i = \boldsymbol{\mathcal{F}}_i(\boldsymbol{F}(\boldsymbol{X}, t), \boldsymbol{A}_i); \qquad \boldsymbol{\mathcal{F}}_i = \frac{1}{\tau_i^v}\left(\hat{\boldsymbol{C}}^{-1} - \boldsymbol{A}_i\right), \qquad && i = 1, \ldots, n_{\text{Maxw}}; \\ &\boldsymbol{A}_i = \boldsymbol{I}; && t = 0, \end{aligned} \tag{29}$$

with $\left\{\tau_1^v, \cdots, \tau_{n_{\text{Maxw}}}^v\right\}$ being the relaxation times of the different Maxwell branches. Appendix 8.1 shows that the evolution equations in (29) for the internal variables $\boldsymbol{\mathcal{A}}$, in conjunction with the definition of the viscous contribution $e_v(\boldsymbol{F}, \boldsymbol{\mathcal{A}})$ in (28), are thermodynamically consistent, as they comply with the dissipation inequality in (13).

3.4. Numerical solution of thermodynamically consistent evolution laws for internal variables

Consider the time interval $[t_n, t]$ with $\Delta t = t - t_n$. The time integration of the ordinary differential equations in (29) permits to obtain the internal variables at time t, namely $\boldsymbol{A}_i$, in terms of a second order tensor $\boldsymbol{D}_{i,n} \in \mathbb{R}^{3\times3}$ and the current value of $\hat{\boldsymbol{C}}^{-1}$, as

$$\boldsymbol{A}_i = \boldsymbol{D}_{i,n}\left(\boldsymbol{A}_{i,n}, \hat{\boldsymbol{C}}_n^{-1}, t\right) + \beta_i\hat{\boldsymbol{C}}^{-1}; \qquad \beta_i \in \mathbb{R}, \tag{30}$$

where the tensor $\boldsymbol{D}_{i,n}$ is a function of the current time t and the values of $\boldsymbol{A}_i$ and $\hat{\boldsymbol{C}}^{-1}$ at time step t_n, i.e., $\boldsymbol{A}_{i,n}$ and $\hat{\boldsymbol{C}}_n^{-1}$, respectively. In the present paper, for the numerical experiments presented, we have made use of the Backward-Euler (implicit) time integration scheme. However, it is still interesting to study some relevant additional time integrators, since useful information with regards to ellipticity of the boundary value problem in (7) can be inferred.

Backward-Euler (implicit) scheme: the numerical integration of (29) yields

$$\frac{\boldsymbol{A}_i - \boldsymbol{A}_{i,n}}{\Delta t} = \boldsymbol{\mathcal{F}}_i(\boldsymbol{F}(\boldsymbol{X}, t), \boldsymbol{A}_i); \qquad \boldsymbol{\mathcal{F}}_i = \frac{1}{\tau_i^v}\left(\hat{\boldsymbol{C}}^{-1} - \boldsymbol{A}_i\right). \tag{31}$$

Equation (31) permits to identify matrix $\boldsymbol{D}_{i,n}$ and the coefficient β_i of the general solution of $\boldsymbol{A}_i$ in (30), as

$$\boldsymbol{D}_{i,n} = \frac{1}{1+\alpha_i}\boldsymbol{A}_{i,n}; \qquad \beta_i = \frac{\alpha_i}{1+\alpha_i}; \qquad \alpha_i = \frac{\Delta t}{\tau_i^v}. \tag{32}$$

Crank-Nicolson (implicit) scheme: this numerical integration scheme can be written as

$$\frac{\boldsymbol{A}_i - \boldsymbol{A}_{i,n}}{\Delta t} = \frac{1}{2}\left(\boldsymbol{\mathcal{F}}_i(\boldsymbol{F}(\boldsymbol{X}, t), \boldsymbol{A}_i) + \boldsymbol{\mathcal{F}}_i(\boldsymbol{F}(\boldsymbol{X}, t_n), \boldsymbol{A}_{i,n})\right) \tag{33}$$

yielding the following values for $\boldsymbol{D}_{i,n}$ and β_i in (30)

$$\boldsymbol{D}_{i,n} = \frac{2-\alpha_i}{2+\alpha_i}\boldsymbol{A}_{i,n} + \beta_i\hat{\boldsymbol{C}}_n^{-1}; \qquad \beta_i = \frac{\alpha_i}{2+\alpha_i}; \tag{34}$$

Semi-analytical time integration scheme: the analytical solution of the ordinary differential equation in (29) yields

$$\boldsymbol{A}_i = \boldsymbol{K}_i(t)e^{-t/\tau_i^v}; \qquad \dot{\boldsymbol{K}}_i(t) = \frac{1}{\tau_i^v}e^{t/\tau_i^v}\hat{\boldsymbol{C}}^{-1}(\boldsymbol{X}, t) \tag{35}$$

The numerical integration of the ordinary differential equation for $\boldsymbol{K}_i(t)$ over the interval $[t_n, t]$ can be approximated as

$$\boldsymbol{K}_i(t) - \boldsymbol{K}_{i,n} \approx \Big(\frac{1}{\tau_i^v}\int_{t_n}^{t} e^{s/\tau_i^v}\, ds\Big)\hat{\boldsymbol{C}}^{-1}(\boldsymbol{X},t) = (e^{t/\tau_i^v} - e^{t_n/\tau_i^v})\hat{\boldsymbol{C}}^{-1}, \tag{36}$$

yielding

$$\boldsymbol{D}_{i,n} = \boldsymbol{K}_{i,n}e^{-t/\tau_i^v}; \qquad \beta_i = 1 - e^{-\Delta t/\tau_i^v}, \tag{37}$$

with

$$\boldsymbol{K}_{i,0} = \boldsymbol{I}; \qquad \boldsymbol{K}_{i,n} = \boldsymbol{K}_{i,n-1} + \hat{\boldsymbol{C}}_n^{-1} e^{t_n/\tau_i^v}\left(1 - e^{-\Delta t/\tau_i^v}\right) \tag{38}$$

Forward-Euler (explicit) scheme: the numerical integration of (29) according to this scheme entails:

$$\frac{\boldsymbol{A}_i - \boldsymbol{A}_{i,n}}{\Delta t} = \boldsymbol{\mathcal{F}}_i(\boldsymbol{F}(\boldsymbol{X},t_n), \boldsymbol{A}_{i,n}), \tag{39}$$

which yields

$$\boldsymbol{D}_{i,n} = \left(1 - \frac{\Delta t}{\tau_i^v}\right)\boldsymbol{A}_{i,n} + \frac{\Delta t}{\tau_i^v}\hat{\boldsymbol{C}}_n^{-1}; \qquad \beta_i = 0. \tag{40}$$

The results for the matrix $\boldsymbol{D}_{i,n}$ and the coefficient β_i for the general solution of the internal variables according to equation (30) can be summarised in Table 1.

Time integration scheme	$\boldsymbol{D}_{i,n}$ (always positive definite)	β_i (always positive)
Backward-Euler	$\frac{1}{1+\alpha_i}\boldsymbol{A}_{i,n}$	$\frac{\alpha_i}{1+\alpha_i} > 0$
Crank-Nicholson	$\frac{2-\alpha_i}{2+\alpha_i}\boldsymbol{A}_{i,n} + \beta_i\hat{\boldsymbol{C}}_n^{-1}$ $(\alpha_i < 2)$	$\frac{\alpha_i}{2+\alpha_i} > 0$
Semi-Analytical	$\boldsymbol{K}_{i,n}e^{-t/\tau_i^v}$	$1 - e^{-\alpha_i} > 0$
Forward-Euler	$(1-\alpha_i)\,\boldsymbol{A}_{i,n} + \alpha_i\hat{\boldsymbol{C}}_n^{-1}$	0

Table 1: Time integration schemes and their respective quantities $\boldsymbol{D}_{i,n}$ and β_i (see (30)).

Remark 1. Some authors advocate for formulations where a multiplicative decomposition of the deformation gradient is made into elastic and viscous contributions. In that context, it is customary to use isochoric-preserving time integrators for the ODE associated with the viscous deformation gradient tensor. These have not been explored in our work.

3.5. Ellipticity of the visco-electro-mechanical constitutive model

In order to determine the ellipticity of the underlying system of partial differential equations in (7), we introduce the following quantities $\mathcal{D}^h_{\text{int},E} := \mathcal{D}^h_{\text{int}}(\boldsymbol{F}, \boldsymbol{D}_0, \boldsymbol{u}\otimes\boldsymbol{V}, \boldsymbol{V}_\perp)$ and $\mathcal{D}^v_{\text{int},E} := \mathcal{D}^v_{\text{int}}(\boldsymbol{F}, \boldsymbol{\mathcal{A}}(\boldsymbol{F}), \boldsymbol{u}\otimes\boldsymbol{V})$ by replacing in (15) $\delta\boldsymbol{F}$ with $\boldsymbol{u}\otimes\boldsymbol{V}$ ($\boldsymbol{u},\boldsymbol{V}\in\mathbb{R}^3$, i.e., $\delta\boldsymbol{F}$ is replaced with a rank-one tensor) and $\delta\boldsymbol{D}_0$ with $\boldsymbol{V}_\perp$ (with $\boldsymbol{V}_\perp\cdot\boldsymbol{V} = 0$), yielding

$$\begin{aligned}
&\mathcal{D}^h_{\text{int},E} = De^h(\boldsymbol{F},\boldsymbol{D}_0)[\boldsymbol{u}\otimes\boldsymbol{V}, \boldsymbol{V}_\perp] = \boldsymbol{P}^h : D\boldsymbol{F}[\boldsymbol{u}\otimes\boldsymbol{V}] + \boldsymbol{E}_0\cdot D\boldsymbol{D}_0[\boldsymbol{V}_\perp];\\
&\mathcal{D}^v_{\text{int},E} = \boldsymbol{P}^v : D\boldsymbol{F}[\boldsymbol{u}\otimes\boldsymbol{V}].
\end{aligned} \tag{41}$$

As it was stated in [58], the hyperelastic contribution complies with a strict positiveness, i.e.,

$$D\Big(\mathcal{D}^h_{\text{int},E}\Big)[\boldsymbol{u}\otimes\boldsymbol{V}, \boldsymbol{V}_\perp] > 0. \tag{42}$$

For the viscous contribution, particularisation of $(41)_b$ yields

$$\mathcal{D}^v_{\text{int},E} = \partial_{\boldsymbol{F}} e^v : (\boldsymbol{u} \otimes \boldsymbol{V}) = \sum_{i=1}^{n_{\text{Maxw}}} \frac{\mu_i^v}{2} D(J^{-2/3}\boldsymbol{C})[\boldsymbol{u} \otimes \boldsymbol{V}] : \boldsymbol{A}_i. \tag{43}$$

In equation (30), we showed that the numerical integration of the evolution equations for the different internal variables $\boldsymbol{A}_i$ in (29) permits to express $\boldsymbol{A}_i$ in the current time step according to the following additive decomposition

$$\boldsymbol{A}_i = \boldsymbol{D}_{i,n} + \beta_i \hat{\boldsymbol{C}}^{-1} = \boldsymbol{D}_{i,n} + \beta_i \left(J^{2/3} \boldsymbol{C}^{-1} \right). \tag{44}$$

Introduction of (44) into (43) yields

$$\mathcal{D}^v_{\text{int},E} = \sum_{i=1}^{n_{\text{Maxw}}} \frac{\mu_i^v}{2} D(J^{-2/3}\boldsymbol{C})[\boldsymbol{u} \otimes \boldsymbol{V}] : \left(\boldsymbol{D}_{i,n} + \beta_i J^{2/3} \boldsymbol{C}^{-1} \right). \tag{45}$$

We can compute the directional derivative of $\mathcal{D}^v_{\text{int},E}$, i.e., $D(\mathcal{D}^v_{\text{int}})[\boldsymbol{u} \otimes \boldsymbol{V}]$, included in Appendix 8.2, and then conclude that

$$D(\mathcal{D}^v_{\text{int},E})[\boldsymbol{u} \otimes \boldsymbol{V}] = \underbrace{\sum_{i=1}^{n_{\text{Maxw}}} \frac{\mu_i^v}{J^{8/3}} \left(\left(\frac{1}{2} \boldsymbol{M}^T \boldsymbol{M} + \frac{1}{9} \delta J^2 \boldsymbol{C} \right) : \boldsymbol{D}_{i,n} \right)}_{\text{Viscous regularisation contribution}} > 0 \Leftrightarrow \boldsymbol{a} \cdot \boldsymbol{D}_{i,n} \boldsymbol{a} > 0; \;\; \forall \boldsymbol{a} \in \mathbb{R}^3, \boldsymbol{a} \not\succeq \boldsymbol{0}, \tag{46}$$

where positiveness of $D(\mathcal{D}^v_{\text{int},E})[\boldsymbol{u} \otimes \boldsymbol{V}]$ is ensured provided that $\boldsymbol{D}_{i,n}$ is positive definite. As shown in Table 1, this is guaranteed unconditionally for the Backward-Euler, the semi-analytical method and Forward-Euler integration schemes considered. For the Crank-Nicholson scheme, this is ensured provided that the constant $\alpha_i = \frac{\Delta t}{\tau_i^v}$ complies with $\alpha_i < 2$, which is a reasonable condition, entailing that the time step used Δt for the numerical integration of the evolution equation (29) should be smaller than twice the minimum of the relaxation times for the different internal variables considered in the model, namely

$$\Delta t \leq 2 \min\{\tau_1^v, \tau_2^v, \ldots, \tau_{\text{nMaxw}}^v\}. \tag{47}$$

The result shown in equation (47) is in fact in agreement with the literature, since visco-elasticity has a regularising effect that can even balance the loss or lack of ellipticity of the hyperelastic contribution of the energy density of the material. For instance, this has been reported in the context of materials with negative hardening modulus, where the use of visco-elasticity has a regularising effect restoring the well-posedness of the boundary value problem. In the context of homogenisation, we will see that the visco-elastic contribution can also have a similar beneficial effect.

3.6. The Helmholtz energy function

Alternatively to the internal energy density function $e(\boldsymbol{F}, \boldsymbol{D}_0, \boldsymbol{\mathcal{A}})$, electro-mechanical constitutive models can be formulated in terms of a Helmholtz energy functional $\Psi(\boldsymbol{F}, \boldsymbol{E}_0, \boldsymbol{\mathcal{A}})$, defined as

$$\Psi(\boldsymbol{F}, \boldsymbol{E}_0, \boldsymbol{\mathcal{A}}) = \Psi^h(\boldsymbol{F}, \boldsymbol{E}_0) + \Psi^v(\boldsymbol{F}, \boldsymbol{\mathcal{A}}); \qquad \Psi^h(\boldsymbol{F}, \boldsymbol{E}_0) = \Psi^h_m(\boldsymbol{F}) + \Psi^h_{em}(\boldsymbol{F}, \boldsymbol{E}_0), \tag{48}$$

where an additive decomposition of the hyperelastic contribution $\Psi^h(\boldsymbol{F}, \boldsymbol{E}_0)$ into its mechanical and electro-mechanical contributions is adopted. The relation between the Helmholtz energy density function and its internal energy counterpart is obtained through the following Legendre transformation

$$\Psi^h_m(\boldsymbol{F}) = e^h_m(\boldsymbol{F}); \quad \Psi^h_{em}(\boldsymbol{F}, \boldsymbol{E}_0) = -\sup_{\boldsymbol{D}_0} \left\{ \boldsymbol{E}_0 \cdot \boldsymbol{D}_0 - e^h_{em}(\boldsymbol{F}, \boldsymbol{E}_0) \right\}; \quad \Psi^v(\boldsymbol{F}, \boldsymbol{\mathcal{A}}) = e^v(\boldsymbol{F}, \boldsymbol{\mathcal{A}}). \tag{49}$$

Using thermodynamical principles, the dissipation inequality $\mathcal{D}$ can be written as

$$\mathcal{D} = \underbrace{\boldsymbol{P} : \dot{\boldsymbol{F}} - \boldsymbol{D}_0 \cdot \dot{\boldsymbol{E}}_0}_{\mathcal{D}_{\Psi_{\text{int}}}} - \dot{\Psi} \geq 0, \tag{50}$$

where the time derivative of the energy density function $\Psi(\boldsymbol{F}, \boldsymbol{E}_0, \boldsymbol{\mathcal{A}})$ is computed as

$$\dot{\Psi} = \partial_{\boldsymbol{F}}\Psi : \dot{\boldsymbol{F}} + \partial_{\boldsymbol{E}_0}\Psi^h \cdot \dot{\boldsymbol{E}}_0 + \partial_{\boldsymbol{\mathcal{A}}}\Psi^v \bullet \dot{\boldsymbol{\mathcal{A}}}. \tag{51}$$

Use of the Coleman and Noll procedure in (50) and (51) (see [19]) yields the following standard constitutive equations,

$$\boldsymbol{P}(\boldsymbol{F}, \boldsymbol{E}_0, \boldsymbol{\mathcal{A}}) = \underbrace{\partial_{\boldsymbol{F}}\Psi^h(\boldsymbol{F}, \boldsymbol{E}_0)}_{\boldsymbol{P}^h(\boldsymbol{F}, \boldsymbol{E}_0)} + \underbrace{\partial_{\boldsymbol{F}}\Psi^v(\boldsymbol{F}, \boldsymbol{\mathcal{A}})}_{\boldsymbol{P}^v(\boldsymbol{F}, \boldsymbol{\mathcal{A}})}; \qquad \boldsymbol{D}_0(\boldsymbol{F}, \boldsymbol{E}_0) = -\partial_{\boldsymbol{E}_0}\Psi^h(\boldsymbol{F}, \boldsymbol{E}_0), \tag{52}$$

with the dissipation inequality given by

$$\mathcal{D}(\boldsymbol{F}, \boldsymbol{\mathcal{A}}, \dot{\boldsymbol{\mathcal{A}}}) = -\partial_{\boldsymbol{\mathcal{A}}}\Psi^v(\boldsymbol{F}, \boldsymbol{\mathcal{A}}) \bullet \dot{\boldsymbol{\mathcal{A}}} \geq 0. \tag{53}$$

Replacing the time derivatives $\dot{\boldsymbol{F}}$ and $\dot{\boldsymbol{E}}_0$ in (50) with virtual fields $\delta\boldsymbol{F}$ and $\delta\boldsymbol{E}_0$, respectively, and splitting $\mathcal{D}_{\Psi_{\text{int}}}$ into hyperelastic and viscous contributions, it yields

$$\mathcal{D}_{\Psi_{\text{int}}}(\boldsymbol{F}, \boldsymbol{E}_0, \boldsymbol{\mathcal{A}}, \boldsymbol{\delta F}, \boldsymbol{\delta E_0}) = \mathcal{D}^h_{\Psi_{\text{int}}}(\boldsymbol{F}, \boldsymbol{E}_0, \boldsymbol{\mathcal{A}}, \boldsymbol{\delta F}, \boldsymbol{\delta E_0}) + \mathcal{D}^v_{\Psi_{\text{int}}}(\boldsymbol{F}, \boldsymbol{\mathcal{A}}, \delta\boldsymbol{F}), \tag{54}$$

where

$$\begin{aligned} \mathcal{D}^h_{\Psi_{\text{int}}}(\boldsymbol{F}, \boldsymbol{E}_0, \boldsymbol{\mathcal{A}}, \boldsymbol{\delta F}, \boldsymbol{\delta E_0}) &= \boldsymbol{P}^h(\boldsymbol{F}, \boldsymbol{E}_0) : \delta\boldsymbol{F} - \boldsymbol{D}_0(\boldsymbol{F}, \boldsymbol{E}_0) \cdot \delta\boldsymbol{E}_0; \\ \mathcal{D}^v_{\Psi_{\text{int}}}(\boldsymbol{F}, \boldsymbol{\mathcal{A}}, \delta\boldsymbol{F}) &= \boldsymbol{P}^v(\boldsymbol{F}, \boldsymbol{\mathcal{A}}(\boldsymbol{F})) : \delta\boldsymbol{F}. \end{aligned} \tag{55}$$

It is possible to show that the directional derivative of both terms in equation (55) with respect to $\delta\boldsymbol{F}$ and $\delta\boldsymbol{E}_0$ yields

$$\begin{aligned} D\mathcal{D}^h_{\Psi_{\text{int}}}[\delta\boldsymbol{F}, \delta\boldsymbol{E}_0] &= [\delta\boldsymbol{F} : \delta\boldsymbol{E}_0 \cdot] \, [\mathbb{H}^h_\Psi] \begin{bmatrix} : \delta\boldsymbol{F} \\ \delta\boldsymbol{E}_0 \end{bmatrix}; \qquad [\mathbb{H}^h_\Psi] = \begin{bmatrix} \boldsymbol{\mathcal{C}}^h_\Psi & -\boldsymbol{\mathcal{P}}^T \\ -\boldsymbol{\mathcal{P}} & -\boldsymbol{\epsilon} \end{bmatrix}; \qquad \left(\boldsymbol{\mathcal{P}}^T\right)_{jJI} = (\boldsymbol{\mathcal{P}})_{IjJ}; \\ D\mathcal{D}^v_{\Psi_{\text{int}}}[\delta\boldsymbol{F}, \delta\boldsymbol{E}_0] &= [\delta\boldsymbol{F} : \delta\boldsymbol{E}_0 \cdot] \, [\mathbb{H}^v_\Psi] \begin{bmatrix} : \delta\boldsymbol{F} \\ \delta\boldsymbol{E}_0 \end{bmatrix}; \qquad [\mathbb{H}^v_\Psi] = \begin{bmatrix} \boldsymbol{\mathcal{C}}^v_\Psi & \boldsymbol{0} \\ \boldsymbol{0} & \boldsymbol{0} \end{bmatrix}, \end{aligned} \tag{56}$$

where $[\mathbb{H}^h_\Psi]$ includes the hyperelastic high order constitutive tensors, namely the fourth order elasticity tensor $\boldsymbol{\mathcal{C}}^h_\Psi \in \mathbb{R}^{3\times3\times3\times3}$, the third order piezoelectric tensor $\boldsymbol{\mathcal{P}} \in \mathbb{R}^{3\times3\times3}$ and the dielectric tensor $\boldsymbol{\epsilon} \in \mathbb{R}^{3\times3}$, whilst $[\mathbb{H}^v_\Psi]$ includes the viscous contribution in the elasticity tensor $\boldsymbol{\mathcal{C}}^v_\Psi \in \mathbb{R}^{3\times3\times3\times3}$, being all of them defined as

$$\begin{aligned} \boldsymbol{\mathcal{C}}^h_\Psi(\boldsymbol{F}, \boldsymbol{E}_0) &:= \partial_{\boldsymbol{F}}\boldsymbol{P}^h = \partial^2_{\boldsymbol{F}\boldsymbol{F}}\Psi^h; & \boldsymbol{\mathcal{C}}^v_\Psi(\boldsymbol{F}, \boldsymbol{\mathcal{A}}) &:= \partial_{\boldsymbol{F}}\boldsymbol{P}^v + \partial_{\boldsymbol{\mathcal{A}}}\boldsymbol{P}^v \bullet \partial_{\boldsymbol{F}}\boldsymbol{\mathcal{A}} = \partial^2_{\boldsymbol{F}\boldsymbol{F}}\Psi^v + \partial^2_{\boldsymbol{F}\boldsymbol{\mathcal{A}}}\Psi^v : \partial_{\boldsymbol{F}}\boldsymbol{\mathcal{A}}; \\ \boldsymbol{\mathcal{P}}(\boldsymbol{F}, \boldsymbol{E}_0) &:= \partial_{\boldsymbol{F}}\boldsymbol{D}_0 = -\partial^2_{\boldsymbol{E}_0\boldsymbol{F}}\Psi^h; & \boldsymbol{\epsilon}(\boldsymbol{F}, \boldsymbol{E}_0) &:= \partial_{\boldsymbol{E}_0}\boldsymbol{D}_0 = -\partial^2_{\boldsymbol{E}_0\boldsymbol{E}_0}\Psi^h. \end{aligned} \tag{57}$$

The tensors in (57) can be related with those emerging from the internal energy density in (20) as (see [70])

$$\boldsymbol{\epsilon} = (\boldsymbol{\theta})^{-1}; \qquad \boldsymbol{\mathcal{P}}^T = -\boldsymbol{\mathcal{Q}} \cdot \boldsymbol{\epsilon}; \qquad \boldsymbol{\mathcal{C}}^h_\Psi = \boldsymbol{\mathcal{C}}^h_e + \boldsymbol{\mathcal{Q}}^T \cdot \boldsymbol{\mathcal{P}}; \qquad \boldsymbol{\mathcal{C}}^v_\Psi = \boldsymbol{\mathcal{C}}^v_e, \tag{58}$$

where the inner product $\cdot$ above indicates contraction of the indices placed immediately before and after. It is now interesting to compute the second directional derivative of the internal energy e with respect to arguments $\boldsymbol{F}$ and $\boldsymbol{E}_0$ (instead of the natural $\boldsymbol{D}_0$). With that in mind, it is necessary to consider $\boldsymbol{D}_0$ expressed (implicitly) as a function of $\boldsymbol{F}$ and $\boldsymbol{E}_0$, namely $\boldsymbol{D}_0 = \tilde{\boldsymbol{D}}_0(\boldsymbol{F}, \boldsymbol{E}_0)$, to obtain

$$D\tilde{\boldsymbol{D}}_0[\delta\boldsymbol{F}, \delta\boldsymbol{E}_0] = \partial_{\boldsymbol{F}}\tilde{\boldsymbol{D}}_0 : \delta\boldsymbol{F} + \partial_{\boldsymbol{E}_0}\tilde{\boldsymbol{D}}_0 \, \delta\boldsymbol{E}_0 = -\partial^2_{\boldsymbol{E}_0\boldsymbol{F}}\Psi : \delta\boldsymbol{F} - \partial^2_{\boldsymbol{E}_0\boldsymbol{E}_0}\Psi\delta\boldsymbol{E}_0 = \boldsymbol{\mathcal{P}} : \delta\boldsymbol{F} + \boldsymbol{\epsilon} \, \delta\boldsymbol{E}_0, \tag{59}$$

where we have made use of equation (57) in the last line of above equation. Making now use of (58) and (59), we can express, after some algebraic manipulation, the second directional derivative of the internal energy e with respect to $\boldsymbol{F}$ and $\boldsymbol{E}_0$ in terms of the second derivatives of the Helmholtz functional $\Psi(\boldsymbol{F}, \boldsymbol{E}_0)$ as

$$D\mathcal{D}_{\Psi_{\text{int}}}(\boldsymbol{F}, \tilde{\boldsymbol{D}}_0)[\delta\boldsymbol{F}, D\tilde{\boldsymbol{D}}_0[\delta\boldsymbol{F}, \delta\boldsymbol{E}_0]] = \delta\boldsymbol{F} : \left(\boldsymbol{\mathcal{C}}^h_\Psi + \boldsymbol{\mathcal{C}}^v_\Psi\right) : \delta\boldsymbol{F} + \delta\boldsymbol{E}_0 \cdot \boldsymbol{\epsilon} \, \delta\boldsymbol{E}_0. \tag{60}$$

Therefore, the ellipticity condition in terms of the Helmholtz energy density function taking $\delta\boldsymbol{F} = \boldsymbol{u} \otimes \boldsymbol{V}$, and then $D\tilde{\boldsymbol{D}}_0[\delta\boldsymbol{F}, \delta\boldsymbol{E}_0] = \boldsymbol{V}_\perp \Rightarrow \delta\boldsymbol{E}_0 = \boldsymbol{\epsilon}^{-1}(\boldsymbol{V}_\perp - \boldsymbol{\mathcal{P}} \cdot \boldsymbol{u} \otimes \boldsymbol{V}))$ yields

$$D\mathcal{D}_{\Psi_{\text{int}}}(\boldsymbol{F}, \tilde{\boldsymbol{D}}_0)[\boldsymbol{u} \otimes \boldsymbol{V}, \boldsymbol{V}_\perp] > 0 \Rightarrow \boldsymbol{u} \otimes \boldsymbol{V} : \left(\boldsymbol{\mathcal{C}}^h_\Psi + \boldsymbol{\mathcal{C}}^v_\Psi\right) : \boldsymbol{u} \otimes \boldsymbol{V} > 0; \qquad \delta\boldsymbol{E}_0 \cdot \boldsymbol{\epsilon} \, \delta\boldsymbol{E}_0 > 0. \tag{61}$$

4. Constitutive equations in nonlinear electro-visco-elasticity: Application to Rank-One layered EAPs

4.1. Effective or macroscopic internal energy functional

In this paper we study the homogenised behaviour of rank-one layered EAPs. The resulting biphasic layered structure is comprised of constituents or phases a and b with volume fractions $c^a = h_0^a / \left(h_0^a + h_0^b\right)$ and $c^b = 1 - c^a$, respectively, where h_0^a and h_0^b denote the thickness of phases a and b in the undeformed configuration $\mathcal{B}_0$, with $h_0^a, h_0^b << 1$ to comply with homogenisation theory. The interface between both phases is characterised by the normal vector $\boldsymbol{N}$[10], spherically parametrised as $\boldsymbol{N} = \left[\sin\bar{\beta}\cos\bar{\alpha}, \quad \sin\bar{\beta}\sin\bar{\alpha}, \quad \cos\bar{\beta}\right]^T$. A scheme illustrating the structure of the rank-one layered composite is shown in Figure 2.

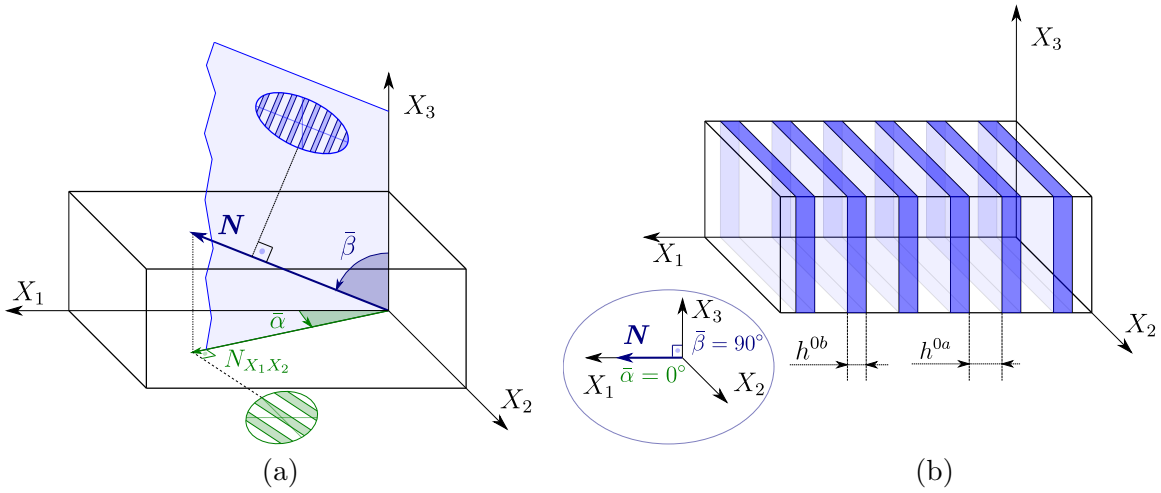

Figure 2: Description of a 3-D rank-one laminated composite material: (a) general case, (b) particularisation for $\bar{\alpha} = 0°, \bar{\beta} = 0°$, for visualisation purposes.

Under the assumption of a homogeneous response in each phase, the macroscopic deformation gradient $\boldsymbol{F}$ and the macroscopic electric displacement field $\boldsymbol{D}_0$ are defined as the weighted sum of those in each phase [23, 24], namely

$$\boldsymbol{F} = c^a \boldsymbol{F}^a + c^b \boldsymbol{F}^b; \qquad \boldsymbol{D}_0 = c^a \boldsymbol{D}_0^a + c^b \boldsymbol{D}_0^b, \tag{62}$$

where the upper indices a and b are used to indicate the respective microscale phases. In addition, we enforce strong continuity of the tangential and normal components of the deformation gradient and the electric displacement, respectively, across the laminate interface, that is,

$$[\![\boldsymbol{F}]\!] \times \boldsymbol{N} = \boldsymbol{0}; \qquad [\![\boldsymbol{D}_0]\!] \cdot \boldsymbol{N} = 0, \tag{63}$$

where $[\![\bullet]\!]$ denotes the standard jump operator across the interface, defined as $[\![\bullet]\!] = (\bullet)^a - (\bullet)^b$. Above jump conditions (63) can alternatively be written in a more convenient form as

$$[\![\boldsymbol{F}]\!] = \boldsymbol{\alpha} \otimes \boldsymbol{N}; \qquad [\![\boldsymbol{D}_0]\!] = \boldsymbol{\mathcal{T}}_{\boldsymbol{N}}\, \boldsymbol{\beta}, \tag{64}$$

where $\boldsymbol{\alpha} \in \mathbb{R}^3$ denotes the microscale deformation gradient amplitude vector [24] ; $\boldsymbol{\beta} \in \mathbb{R}^2$, the microscale electric displacement amplitude vector; and $\boldsymbol{\mathcal{T}}_{\boldsymbol{N}} \in \mathbb{R}^{3\times 2}$, a projection operator onto the plane normal to the unit vector $\boldsymbol{N}$ defined as $\boldsymbol{\mathcal{T}}_{\boldsymbol{N}} = \boldsymbol{T}_1 \otimes \boldsymbol{E}_1 + \boldsymbol{T}_2 \otimes \boldsymbol{E}_2$, where $\boldsymbol{T}_1$ and $\boldsymbol{T}_2$ are two linearly independent unit vectors contained within the laminate plane, and $\boldsymbol{E}_1 = [1\ 0]^T$ and $\boldsymbol{E}_2 = [0\ 1]^T$.

[10] Throughout this Section, this unit normal is not to be confused with the outward unit normal to the boundary presented in Section 2.

Combination of equations (62) and (64) permits to obtain the microscale deformation gradient $\boldsymbol{F}^{a,b}$ and electric displacement $\boldsymbol{D}_0^{a,b}$ as

$$\boldsymbol{F}^a(\boldsymbol{F},\boldsymbol{\alpha}) = \boldsymbol{F} + c^b\boldsymbol{\alpha}\otimes\boldsymbol{N}; \qquad \boldsymbol{D}_0^a(\boldsymbol{D}_0,\boldsymbol{\beta}) = \boldsymbol{D}_0 + c^b\boldsymbol{\mathcal{T}}_{\boldsymbol{N}}\boldsymbol{\beta}; \tag{65a}$$

$$\boldsymbol{F}^b(\boldsymbol{F},\boldsymbol{\alpha}) = \boldsymbol{F} - c^a\boldsymbol{\alpha}\otimes\boldsymbol{N}; \qquad \boldsymbol{D}_0^b(\boldsymbol{D}_0,\boldsymbol{\beta}) = \boldsymbol{D}_0 - c^a\boldsymbol{\mathcal{T}}_{\boldsymbol{N}}\boldsymbol{\beta}, \tag{65b}$$

from where their time derivatives can be computed as

$$\dot{\boldsymbol{F}}^a = \dot{\boldsymbol{F}} + c^b\dot{\boldsymbol{\alpha}}\otimes\boldsymbol{N}; \qquad \dot{\boldsymbol{F}}^b = \dot{\boldsymbol{F}} - c^a\dot{\boldsymbol{\alpha}}\otimes\boldsymbol{N}; \tag{66a}$$

$$\dot{\boldsymbol{D}}_0^a = \dot{\boldsymbol{D}}_0 + c^b\boldsymbol{\mathcal{T}}_{\boldsymbol{N}}\dot{\boldsymbol{\beta}}; \qquad \dot{\boldsymbol{D}}_0^b = \dot{\boldsymbol{D}}_0 - c^a\boldsymbol{\mathcal{T}}_{\boldsymbol{N}}\dot{\boldsymbol{\beta}}. \tag{66b}$$

Remark 2. The expression for the microscopic deformation gradient tensors $\{\boldsymbol{F}^a,\boldsymbol{F}^b\}$ in terms of the macroscopic deformation gradient tensor $\boldsymbol{F}$ and the spatial amplitude vector $\boldsymbol{\alpha}$ in equation (65) follows an unconventional additive decomposition. Although it has been previously used in [58], a multiplicative decomposition [8, 24] has been traditionally preferred, whereby $\{\boldsymbol{F}^a,\boldsymbol{F}^b\}$ are defined in terms of a material amplitude vector $\widetilde{\boldsymbol{\alpha}}$ as

$$\boldsymbol{F}^a = \boldsymbol{F}\left(\boldsymbol{I} + c^b\widetilde{\boldsymbol{\alpha}}\otimes\boldsymbol{N}\right); \qquad \boldsymbol{F}^b = \boldsymbol{F}\left(\boldsymbol{I} - c^a\widetilde{\boldsymbol{\alpha}}\otimes\boldsymbol{N}\right). \tag{67}$$

Notice that both additive and multiplicative decompositions are equivalent, with the relationship between the material amplitude vector $\widetilde{\boldsymbol{\alpha}}$ in (67) and its Eulerian or spatial counterpart $\boldsymbol{\alpha}$, associated with the additive decomposition, in (65) is given as $\boldsymbol{\alpha} = \boldsymbol{F}\widetilde{\boldsymbol{\alpha}}$.

This choice of the additive decomposition entails a considerable simplification from the algebraic standpoint, due to the lower degree of nonlinearity associated. Specifically, this reflects in a higher tractability of the second directional derivatives of the effective internal energy functional $e(\boldsymbol{F},\boldsymbol{D}_0)$, and hence of the effective constitutive tensors associated with it, namely $\{\boldsymbol{\mathcal{C}}_e,\boldsymbol{\mathcal{Q}},\boldsymbol{\theta}\}$.

The homogenised or effective internal energy density functional of the composite $e\left(\boldsymbol{F},\boldsymbol{D}_0,\boldsymbol{\mathcal{A}}\right)$ can be postulated as[11]

$$e\left(\boldsymbol{F},\boldsymbol{D}_0,\boldsymbol{\mathcal{A}}\right) = \begin{cases} \hat{e}(\boldsymbol{F},\boldsymbol{D}_0,\boldsymbol{\mathcal{A}},\boldsymbol{\alpha},\boldsymbol{\beta}), \\ \text{s.t.} \begin{cases} \mathcal{D}^a \geq 0; & \text{(Dissipation inequality in micro phase a)} \\ \mathcal{D}^b \geq 0; & \text{(Dissipation inequality in micro phase b)} \\ \mathcal{D} \geq 0; & \text{(Dissipation inequality at the macro level)} \end{cases} \end{cases} \tag{68}$$

with

$$\begin{aligned} \hat{e}(\boldsymbol{F},\boldsymbol{D}_0,\boldsymbol{\mathcal{A}},\boldsymbol{\alpha},\boldsymbol{\beta}) &= c^a e^a\left(\boldsymbol{F}^a\left(\boldsymbol{F},\boldsymbol{\alpha}\right),\boldsymbol{D}_0^a\left(\boldsymbol{D}_0,\boldsymbol{\beta}\right),\boldsymbol{\mathcal{A}}^a\right) + c^b e^b\left(\boldsymbol{F}^b\left(\boldsymbol{F},\boldsymbol{\alpha}\right),\boldsymbol{D}_0^b\left(\boldsymbol{D}_0,\boldsymbol{\beta}\right),\boldsymbol{\mathcal{A}}^b\right); \\ e^a(\boldsymbol{F}^a,\boldsymbol{D}_0^a,\boldsymbol{\mathcal{A}}^a) &= e^{a,h}(\boldsymbol{F}^a,\boldsymbol{D}_0^a) + e^{a,v}(\boldsymbol{F}^a,\boldsymbol{\mathcal{A}}^a); \\ e^b(\boldsymbol{F}^b,\boldsymbol{D}_0^b,\boldsymbol{\mathcal{A}}^b) &= e^{b,h}(\boldsymbol{F}^b,\boldsymbol{D}_0^b) + e^{b,v}(\boldsymbol{F}^b,\boldsymbol{\mathcal{A}}^b), \end{aligned} \tag{69}$$

where $e^a = e^a\left(\boldsymbol{F}^a,\boldsymbol{D}_0^a,\boldsymbol{\mathcal{A}}^a\right)$ and $e^b = e^b\left(\boldsymbol{F}^b,\boldsymbol{D}_0^b,\boldsymbol{\mathcal{A}}^b\right)$ are the microscale internal energy density functions expressed in terms of their respective microscale fields, additively decomposed into their hyperelastic contributions $\{e^{a,h},e^{b,h}\}$ and their visco-elastic contributions $\{e^{a,v},e^{b,v}\}$. With regards to the constraints that the effective internal energy density functional $e\left(\boldsymbol{F},\boldsymbol{D}_0,\boldsymbol{\mathcal{A}}\right)$ must satisfy in (68), the first two, namely $\mathcal{D}^a$ and $\mathcal{D}^b$, represent the dissipation inequalities in the microscopic phases a and b, respectively. Dissipation in phase a (analogously in phase b)

$$\mathcal{D}^a = \underbrace{\boldsymbol{P}^a : \dot{\boldsymbol{F}}^a + \boldsymbol{E}_0^a\cdot\dot{\boldsymbol{D}}_0^a}_{\mathcal{D}^a_{\text{int}}} - \dot{e}^a \geq 0, \tag{70}$$

[11] Note that 's.t.' stands for 'subject to'.

where the time derivative of the internal energy density function in phase a (analogously in phase b) is

$$\dot{e}^a = \partial_{\boldsymbol{F}^a} e^a : \dot{\boldsymbol{F}}^a + \partial_{\boldsymbol{D}_0^a} e^{a,h} \cdot \dot{\boldsymbol{D}}_0^a + \partial_{\boldsymbol{\mathcal{A}}^a} e^{a,v} : \dot{\boldsymbol{\mathcal{A}}}^a. \tag{71}$$

Introduction of (71) into the dissipation inequality $\mathcal{D}^a$ (70) yields the final form of the microscopic dissipation inequality as (analogously for phase b)

$$\mathcal{D}^a = (\boldsymbol{P}^a - \partial_{\boldsymbol{F}^a} e^a) : \dot{\boldsymbol{F}}^a + \left(\boldsymbol{E}_0^a - \partial_{\boldsymbol{D}_0^a} e^{a,h}\right) \cdot \dot{\boldsymbol{D}}_0^a - \partial_{\boldsymbol{\mathcal{A}}^a} e^{a,v} : \dot{\boldsymbol{\mathcal{A}}}^a \tag{72}$$

Application of the Coleman-Noll procedure in (72) permits to obtain the following constitutive equations at phase a (analogously for phase b)

$$\boldsymbol{P}^a(\boldsymbol{F}^a, \boldsymbol{D}_0^a, \boldsymbol{\mathcal{A}}^a) = \underbrace{\partial_{\boldsymbol{F}^a} e^{a,h}(\boldsymbol{F}^a, \boldsymbol{D}_0^a)}_{\boldsymbol{P}^{a,h}(\boldsymbol{F}^a, \boldsymbol{D}_0^a)} + \underbrace{\partial_{\boldsymbol{F}^a} e^{a,v}(\boldsymbol{F}^a, \boldsymbol{\mathcal{A}}^a)}_{\boldsymbol{P}^{a,v}(\boldsymbol{F}^a, \boldsymbol{\mathcal{A}})}; \qquad \boldsymbol{E}_0^a(\boldsymbol{F}^a, \boldsymbol{D}_0^a, \boldsymbol{\mathcal{A}}^a) = \partial_{\boldsymbol{D}_0^a} e^{a,h}(\boldsymbol{F}^a, \boldsymbol{D}_0^a, \boldsymbol{\mathcal{A}}^a), \tag{73}$$

with the dissipation inequality at phase a (analogously for phase b)

$$\mathcal{D}^a(\boldsymbol{F}^a, \boldsymbol{\mathcal{A}}^a, \dot{\boldsymbol{\mathcal{A}}}^a) = -\partial_{\boldsymbol{\mathcal{A}}^a} e^{a,v}(\boldsymbol{F}^a, \boldsymbol{\mathcal{A}}^a) \bullet \dot{\boldsymbol{\mathcal{A}}}^a \geq 0. \tag{74}$$

The constraint $\mathcal{D}$ in equation (68) represents the dissipation inequality in the macroscopic level. This can be written exactly as in the case of a single phase material, and hence, as in equation (10), namely

$$\mathcal{D} = \underbrace{\boldsymbol{P} : \dot{\boldsymbol{F}} + \boldsymbol{E}_0 \cdot \dot{\boldsymbol{D}}_0}_{\mathcal{D}_{\text{int}}} - \dot{e} \geq 0. \tag{75}$$

The time derivative of the macroscopic internal energy density $e(\boldsymbol{F}, \boldsymbol{D}_0, \boldsymbol{\mathcal{A}}, \boldsymbol{\alpha}, \boldsymbol{\beta})$ can be computed by differentiating with respect to time the right-hand side on equation (69), yielding

$$\begin{aligned} \dot{e}(\boldsymbol{F}, \boldsymbol{D}_0, \boldsymbol{\mathcal{A}}, \boldsymbol{\alpha}, \boldsymbol{\beta}) = {} & c^a \left(\partial_{\boldsymbol{F}^a} e^a : \dot{\boldsymbol{F}}^a + \partial_{\boldsymbol{D}_0^a} e^a \cdot \dot{\boldsymbol{D}}_0^{a,h} + \partial_{\boldsymbol{\mathcal{A}}^a} e^{a,v} \bullet \dot{\boldsymbol{\mathcal{A}}}^a\right) \\ & + c^b \left(\partial_{\boldsymbol{F}^b} e^b : \dot{\boldsymbol{F}}^b + \partial_{\boldsymbol{D}_0^b} e^b \cdot \dot{\boldsymbol{D}}_0^{b,h} + \partial_{\boldsymbol{\mathcal{A}}^b} e^{b,v} \bullet \dot{\boldsymbol{\mathcal{A}}}^b\right). \end{aligned} \tag{76}$$

Making use of the time derivatives of the microscopic field $\{\boldsymbol{F}^a, \boldsymbol{F}^b, \boldsymbol{D}_0^a, \boldsymbol{D}_0^b\}$ in (66) permits to conveniently re-write $\dot{e}(\boldsymbol{F}, \boldsymbol{D}_0, \boldsymbol{\mathcal{A}}, \boldsymbol{\alpha}, \boldsymbol{\beta})$ in (76) in terms of the time derivatives of its arguments, namely $\{\boldsymbol{F}, \boldsymbol{D}_0, \boldsymbol{\mathcal{A}}, \boldsymbol{\alpha}, \boldsymbol{\beta}\}$, as

$$\begin{aligned} \dot{e}(\boldsymbol{F}, \boldsymbol{D}_0, \boldsymbol{\mathcal{A}}, \boldsymbol{\alpha}, \boldsymbol{\beta}) = {} & \left(c^a \partial_{\boldsymbol{F}^a} e^a + c^b \partial_{\boldsymbol{F}^b} e^b\right) : \dot{\boldsymbol{F}} + \left(c^a \partial_{\boldsymbol{D}_0^a} e^{a,h} + c^b \partial_{\boldsymbol{D}_0^b} e^{b,h}\right) \cdot \dot{\boldsymbol{D}}_0 \\ & + c^a c^b \left(\partial_{\boldsymbol{F}^a} e^a - \partial_{\boldsymbol{F}^b} e^b\right) : \dot{\boldsymbol{\alpha}} \otimes \boldsymbol{N} + c^a c^b \left(\partial_{\boldsymbol{D}_0^a} e^{a,h} - \partial_{\boldsymbol{D}_0^b} e^{b,h}\right) \cdot \boldsymbol{\mathcal{T}}_{\boldsymbol{N}} \dot{\boldsymbol{\beta}} \\ & + c^a \partial_{\boldsymbol{\mathcal{A}}^a} e^{a,v} \bullet \dot{\boldsymbol{\mathcal{A}}}^a + c^b \partial_{\boldsymbol{\mathcal{A}}^b} e^{b,v} \bullet \dot{\boldsymbol{\mathcal{A}}}^b. \end{aligned} \tag{77}$$

Introduction of the constitutive relationships obtained in equations (73) permits to re-write (77) as

$$\begin{aligned} \dot{e}(\boldsymbol{F}, \boldsymbol{D}_0, \boldsymbol{\mathcal{A}}, \boldsymbol{\alpha}, \boldsymbol{\beta}) = {} & \left(c^a \boldsymbol{P}^a + c^b \boldsymbol{P}^b\right) : \dot{\boldsymbol{F}} + \left(c^a \boldsymbol{E}_0^a + c^b \boldsymbol{E}_0^b\right) \cdot \dot{\boldsymbol{D}}_0 \\ & + c^a c^b \left(\boldsymbol{P}^a - \boldsymbol{P}^b\right) : \dot{\boldsymbol{\alpha}} \otimes \boldsymbol{N} + c^a c^b \left(\boldsymbol{E}_0^a - \boldsymbol{E}_0^b\right) \cdot \boldsymbol{\mathcal{T}}_{\boldsymbol{N}} \dot{\boldsymbol{\beta}} \\ & + c^a \partial_{\boldsymbol{\mathcal{A}}^a} e^{a,v} \bullet \dot{\boldsymbol{\mathcal{A}}}^a + c^b \partial_{\boldsymbol{\mathcal{A}}^b} e^{b,v} \bullet \dot{\boldsymbol{\mathcal{A}}}^b. \end{aligned} \tag{78}$$

Introduction of (78) into the macroscopic dissipation inequality $\mathcal{D}$ in (75) yields

$$\begin{aligned} \mathcal{D} = {} & \left(\boldsymbol{P} - \left(c^a \boldsymbol{P}^a + c^b \boldsymbol{P}^b\right)\right) : \dot{\boldsymbol{F}} + \left(\boldsymbol{E}_0 - \left(c^a \boldsymbol{E}_0^a + c^b \boldsymbol{E}_0^b\right)\right) \cdot \dot{\boldsymbol{D}}_0 \\ & - \left(c^a \partial_{\boldsymbol{\mathcal{A}}^a} e^{v,a} \bullet \dot{\boldsymbol{\mathcal{A}}}^a + c^b \partial_{\boldsymbol{\mathcal{A}}^b} e^{v,b} \bullet \dot{\boldsymbol{\mathcal{A}}}^b\right) \geq 0. \end{aligned} \tag{79}$$

Application of the Coleman-Noll procedure yields the following constitutive relationships

$$\begin{aligned} \boldsymbol{P}(\boldsymbol{F},\boldsymbol{D}_0,\boldsymbol{\mathcal{A}}) &= c^a\boldsymbol{P}^a + c^b\boldsymbol{P}^b; & \boldsymbol{E}_0 &= c^a\boldsymbol{E}_0^a + c^b\boldsymbol{E}_0^b; \\ \boldsymbol{f}_{\boldsymbol{P}} &= [\![\boldsymbol{P}]\!]\boldsymbol{N} = \boldsymbol{0}; & \boldsymbol{f}_{\boldsymbol{E}_0} &= \boldsymbol{\mathcal{T}}_{\boldsymbol{N}}{}^T[\![\boldsymbol{E}_0]\!] = \boldsymbol{0} \iff [\![\boldsymbol{E}_0]\!]\times\boldsymbol{N} = \boldsymbol{0}; \\ \mathcal{D} &= c^a\partial_{\boldsymbol{\mathcal{A}}^a}e^{v,a}\bullet\dot{\boldsymbol{\mathcal{A}}}^a + c^b\partial_{\boldsymbol{\mathcal{A}}^b}e^{v,b}\bullet\dot{\boldsymbol{\mathcal{A}}}^b \geq 0. \end{aligned} \tag{80}$$

Crucially, equation $(80)_a$ yields the macroscopic expressions for the first Piola-Kirchhoff stress tensor $\boldsymbol{P}$ and the electric field $\boldsymbol{E}_0$ in terms of their microscopic counterparts. Furthermore, equation $(80)_b$ represents the strong enforcement of the normal and tangential components of the traction vector and the electric field vector, respectively. Finally, it must be noticed that the dissipation inequality $\mathcal{D}$ in $(80)_c$ is automatically fulfilled if the dissipation inequalities in the micro-structural phases, namely $\mathcal{D}^a$ and $\mathcal{D}^b$ are satisfied. Thus, above homogenised energy functional $e(\boldsymbol{F},\boldsymbol{D}_0,\boldsymbol{\mathcal{A}})$ in (68) can be re-written as

$$e\left(\boldsymbol{F},\boldsymbol{D}_0,\boldsymbol{\mathcal{A}}\right) = \begin{cases} \hat{e}(\boldsymbol{F},\boldsymbol{D}_0,\boldsymbol{\mathcal{A}},\boldsymbol{\alpha},\boldsymbol{\beta}), \\ \text{s.t.} \begin{cases} \boldsymbol{P} = c^a\boldsymbol{P}^a + c^b\boldsymbol{P}^b; & \text{(First Piola-Kirchoff in macro and micro scales)} \\ \boldsymbol{E}_0 = c^a\boldsymbol{E}_0^a + c^b\boldsymbol{E}_0^b; & \text{(Electric field in macro and micro scales)} \\ \boldsymbol{f}_{\boldsymbol{P}} = [\![\boldsymbol{P}]\!]\boldsymbol{N} = \boldsymbol{0}; & \text{(Traction jump across microscopic interface)} \\ \boldsymbol{f}_{\boldsymbol{E}_0} = \boldsymbol{\mathcal{T}}_{\boldsymbol{N}}{}^T[\![\boldsymbol{E}_0]\!] = \boldsymbol{0}; & \text{(Electric field jump across microscopic interface)} \\ \mathcal{D}^a \geq 0; & \text{(Dissipation inequality at micro phase a)} \\ \mathcal{D}^b \geq 0; & \text{(Dissipation inequality at micro phase b)} \end{cases} \end{cases} \tag{81}$$

4.2. Solution of the amplitude vectors $\boldsymbol{\alpha}$ and $\boldsymbol{\beta}$

The equivalent jump conditions in equation $(80)_b$ represent a system of nonlinear equations where the microscale amplitude vectors $\{\boldsymbol{\alpha},\boldsymbol{\beta}\}$ can be resolved in terms of the macroscale homogenised fields $\boldsymbol{F},\boldsymbol{D}_0$ and the set of internal variables $\boldsymbol{\mathcal{A}} = \{\boldsymbol{\mathcal{A}}^a,\boldsymbol{\mathcal{A}}^b\}$. To ensure existence of solutions for $\{\boldsymbol{\alpha},\boldsymbol{\beta}\}$, the Jacobian matrix of the vector of nonlinear equations given by $\begin{bmatrix}\boldsymbol{f}_{\boldsymbol{P}}^T & \boldsymbol{f}_{\boldsymbol{E}_0}^T\end{bmatrix}^T$ must be positive definite, which is equivalent to the following condition

$$\begin{bmatrix}\delta\boldsymbol{\alpha}\cdot & \delta\boldsymbol{\beta}\cdot\end{bmatrix}\begin{bmatrix}D\boldsymbol{f}_{\boldsymbol{P}}\left[\delta\boldsymbol{\alpha},\delta\boldsymbol{\beta}\right] \\ D\boldsymbol{f}_{\boldsymbol{E}_0}\left[\delta\boldsymbol{\alpha},\delta\boldsymbol{\beta}\right]\end{bmatrix} > 0. \tag{82}$$

Following a similar procedure to that described in [58] for the hyperelastic case, we can reach the following expression:

$$\begin{bmatrix}\delta\boldsymbol{\alpha}\cdot & \delta\boldsymbol{\beta}\cdot\end{bmatrix}\begin{bmatrix}D\boldsymbol{f}_{\boldsymbol{P}}\left[\delta\boldsymbol{\alpha},\delta\boldsymbol{\beta}\right] \\ D\boldsymbol{f}_{\boldsymbol{E}_0}\left[\delta\boldsymbol{\alpha},\delta\boldsymbol{\beta}\right]\end{bmatrix} = \begin{bmatrix}\delta\boldsymbol{\alpha}\otimes\boldsymbol{N} : \boldsymbol{N}_\perp\cdot\end{bmatrix}\begin{bmatrix}\hat{\mathbb{H}}_e\end{bmatrix}\begin{bmatrix}: \delta\boldsymbol{\alpha}\otimes\boldsymbol{N} \\ \boldsymbol{N}_\perp\end{bmatrix} > 0 \tag{83}$$

where $\boldsymbol{\mathcal{T}}_{\boldsymbol{N}}\delta\boldsymbol{\beta}$ has been renamed as $\boldsymbol{N}_\perp$ by noticing that it represents a vector contained within the laminate plane, and

$$[\hat{\mathbb{H}}_e] = \begin{bmatrix}\hat{\boldsymbol{\mathcal{C}}}_e & \hat{\boldsymbol{\mathcal{Q}}}^T \\ \hat{\boldsymbol{\mathcal{Q}}} & \hat{\boldsymbol{\theta}}\end{bmatrix}, \tag{84}$$

with the symbol $(\hat{\bullet})$ representing an average term of the form: $(\hat{\bullet}) = c^b\left(\bullet^a\right) + c^a\left(\bullet^b\right)$. The main difference with respect to the hyperelastic case described in [58] is that the constitutive tensor includes a viscoelastic contribution for the purely mechanical component, in the following way, for phase a:

$$\boldsymbol{\mathcal{C}}_e^{a,h}(\boldsymbol{F},\boldsymbol{D}_0) := \partial^2_{\boldsymbol{F}\boldsymbol{F}}e^{a,h}; \qquad \boldsymbol{\mathcal{C}}_e^{a,v}(\boldsymbol{F},\boldsymbol{\mathcal{A}}) := \partial^2_{\boldsymbol{F}\boldsymbol{F}}e^{a,v} + \partial^2_{\boldsymbol{F}\boldsymbol{\mathcal{A}}}e^{a,v}\bullet\partial_{\boldsymbol{F}}\boldsymbol{\mathcal{A}}^a \tag{85}$$

and similarly for those in phase b, namely

$$\boldsymbol{\mathcal{C}}_e^{b,h}(\boldsymbol{F},\boldsymbol{D}_0) := \partial^2_{\boldsymbol{F}\boldsymbol{F}}e^{b,h}; \qquad \boldsymbol{\mathcal{C}}_e^{b,v}\left(\boldsymbol{F},\boldsymbol{\mathcal{A}}\right) := \partial^2_{\boldsymbol{F}\boldsymbol{F}}e^{b,v} + \partial^2_{\boldsymbol{F}\boldsymbol{\mathcal{A}}}e^{b,v}\bullet\partial_{\boldsymbol{F}}\boldsymbol{\mathcal{A}}^b \tag{86}$$

As it is immediate to see, the right-hand side of above equation (83) is (strictly) positive provided that microscale internal energy functionals e^a and e^b are individually elliptic. Thus, provided that the

hyperelastic contributions of the energy density functions of each phase $e^{a,h}$ and $e^{b,h}$ are defined via CMV functions and that positive definiteness condition in (46) is satisfied, above inequality (83) is fulfilled, and thus existence of solution $\boldsymbol{\alpha}, \boldsymbol{\beta}$ is always guaranteed.

Once the existence of solution $\boldsymbol{\alpha}, \boldsymbol{\beta}$ is shown, its computation can be carried out via a k-iterative Newton-Raphson algorithm, namely

$$\begin{bmatrix}\delta\boldsymbol{\alpha}\cdot & \delta\boldsymbol{\beta}\cdot\end{bmatrix}\begin{bmatrix}\boldsymbol{f}_{\boldsymbol{P}}^{k}\\ \boldsymbol{f}_{\boldsymbol{E}_0}^{k}\end{bmatrix}+\begin{bmatrix}\delta\boldsymbol{\alpha}\cdot & \delta\boldsymbol{\beta}\cdot\end{bmatrix}\begin{bmatrix}D\boldsymbol{f}_{\boldsymbol{P}}^{k}\left[\Delta\boldsymbol{\alpha}\right]\\ D\boldsymbol{f}_{\boldsymbol{E}_0}^{k}\left[\Delta\boldsymbol{\beta}\right]\end{bmatrix}=0;\qquad \boldsymbol{\alpha}^{k+1}=\boldsymbol{\alpha}^{k}+\Delta\boldsymbol{\alpha};\qquad \boldsymbol{\beta}^{k+1}=\boldsymbol{\beta}^{k}+\Delta\boldsymbol{\beta},\tag{87}$$

which can alternatively be written as

$$\begin{bmatrix}\Delta\boldsymbol{\alpha}\\ \Delta\boldsymbol{\beta}\end{bmatrix}=-[\hat{\mathbb{H}}_{e}^{\boldsymbol{N}}]_{k}^{-1}\begin{bmatrix}[\![\boldsymbol{P}]\!]\boldsymbol{N}\\ \boldsymbol{\mathcal{T}}_{\boldsymbol{N}}{}^{T}[\![\boldsymbol{E}_0]\!]\end{bmatrix}_{k},\tag{88}$$

which involves an iterative scheme where microscale amplitude vectors are iterated until convergence (strong satisfaction of jump conditions) is fulfilled.

4.3. Sensitivity of the microscale amplitude vectors with respect to macroscale fields

Let us recall the jump conditions $\boldsymbol{f}_{\boldsymbol{P}}$ and $\boldsymbol{f}_{\boldsymbol{D}_0}$ in equation (80), and let us introduce the following scalar functions

$$\mathcal{R}_{\boldsymbol{F}}=\delta\boldsymbol{\alpha}\cdot\boldsymbol{f}_{\boldsymbol{P}};\qquad \mathcal{R}_{\boldsymbol{D}_0}=\delta\boldsymbol{\beta}\cdot\boldsymbol{f}_{\boldsymbol{D}_0}.\tag{89}$$

From the definition of the jump conditions in (80), and the dependence of $\boldsymbol{F}^{a}$ and $\boldsymbol{F}^{b}$ with respect to $\boldsymbol{F}$ and $\boldsymbol{\alpha}$ (see (65)) and that of $\boldsymbol{D}_0^{a}$ and $\boldsymbol{D}_0^{b}$ with respect to $\boldsymbol{D}_0$ and $\boldsymbol{\beta}$ (see (65)), (89) can be written then as

$$\mathcal{R}_{\boldsymbol{F}}(\boldsymbol{F},\boldsymbol{D}_0)=(\delta\boldsymbol{\alpha}\otimes\boldsymbol{N}):\Big(\boldsymbol{P}^{a}\Big(\boldsymbol{F}^{a}(\boldsymbol{F},\boldsymbol{\alpha}),\boldsymbol{D}_0^{a}(\boldsymbol{D}_0,\boldsymbol{\beta}),\boldsymbol{\mathcal{A}}^{a}\left(\boldsymbol{F}^{a}(\boldsymbol{F},\boldsymbol{\alpha})\right)\Big)\tag{90a}$$

$$-\boldsymbol{P}^{b}\Big(\boldsymbol{F}^{b}(\boldsymbol{F},\boldsymbol{\alpha}),\boldsymbol{D}_0^{b}(\boldsymbol{D}_0,\boldsymbol{\beta}),\boldsymbol{\mathcal{A}}^{b}\left(\boldsymbol{F}^{b}(\boldsymbol{F},\boldsymbol{\alpha})\right)\Big)\Big)=0;\qquad \forall\delta\boldsymbol{\alpha};\tag{90b}$$

$$\mathcal{R}_{\boldsymbol{D}_0}(\boldsymbol{F},\boldsymbol{D}_0)=(\boldsymbol{\mathcal{T}}_{\boldsymbol{N}}\delta\boldsymbol{\beta})\cdot\Big(\boldsymbol{E}_0^{a}\Big(\boldsymbol{F}^{a}(\boldsymbol{F},\boldsymbol{\alpha}),\boldsymbol{D}_0^{a}(\boldsymbol{D}_0,\boldsymbol{\beta}),\boldsymbol{\mathcal{A}}^{a}\left(\boldsymbol{F}^{a}(\boldsymbol{F},\boldsymbol{\alpha})\right)\Big)\tag{90c}$$

$$-\boldsymbol{E}_0^{b}\Big(\boldsymbol{F}^{b}(\boldsymbol{F},\boldsymbol{\alpha}),\boldsymbol{D}_0^{b}(\boldsymbol{D}_0,\boldsymbol{\beta}),\boldsymbol{\mathcal{A}}^{b}\left(\boldsymbol{F}^{b}(\boldsymbol{F},\boldsymbol{\alpha})\right)\Big)\Big)=0;\qquad \forall\delta\boldsymbol{\beta},\tag{90d}$$

which provides a set of equations where the microscale amplitude vectors $\boldsymbol{\alpha}$ and $\boldsymbol{\beta}$ can be expressed in an implicit manner in terms of the macroscale deformation gradient $\boldsymbol{F}$ and electric displacement $\boldsymbol{D}_0$. Computation of the sensitivities of $\{\boldsymbol{\alpha},\boldsymbol{\beta}\}$ with respect to $\{\boldsymbol{F},\boldsymbol{D}_0\}$ can be accomplished therefore by taking advantage of the implicit function theorem. As a result, computation of the directional derivatives $D\mathcal{R}_{\boldsymbol{F}}[\delta\boldsymbol{F}]$, $D\mathcal{R}_{\boldsymbol{D}_0}[\delta\boldsymbol{F}]$, $D\mathcal{R}_{\boldsymbol{F}}[\delta\boldsymbol{D}_0]$ and $D\mathcal{R}_{\boldsymbol{D}_0}[\delta\boldsymbol{D}_0]$ permits to obtain the desired sensitivities as follows

$$\begin{bmatrix}D\boldsymbol{\alpha}[\delta\boldsymbol{F}]\\ D\boldsymbol{\beta}[\delta\boldsymbol{F}]\end{bmatrix}=-[\hat{\mathbb{H}}_{e}^{\boldsymbol{N}}]^{-1}\begin{bmatrix}[\![\boldsymbol{\mathcal{C}}_{e,\boldsymbol{N}\bullet}]\!]\\ \boldsymbol{\mathcal{T}}_{\boldsymbol{N}}{}^{T}[\![\boldsymbol{\mathcal{Q}}]\!]\end{bmatrix}[:\delta\boldsymbol{F}];\qquad \begin{bmatrix}D\boldsymbol{\alpha}[\delta\boldsymbol{D}_0]\\ D\boldsymbol{\beta}[\delta\boldsymbol{D}_0]\end{bmatrix}=-[\hat{\mathbb{H}}_{e}^{\boldsymbol{N}}]^{-1}\begin{bmatrix}\boldsymbol{N}\cdot[\![\boldsymbol{\mathcal{Q}}]\!]^{T}\\ \boldsymbol{\mathcal{T}}_{\boldsymbol{N}}{}^{T}[\![\boldsymbol{\theta}]\!]\end{bmatrix}[\delta\boldsymbol{D}_0],\tag{91}$$

where $(\boldsymbol{\mathcal{C}}_{e,\boldsymbol{N}\bullet})_{ijJ}=(\boldsymbol{\mathcal{C}}_{e})_{iIjJ}N_I$. The reader is referred to Reference [58] for the derivation of the result in (91). The computation of the sensitivities in (91) is always well-defined due to the invertibility of the tangent operator $[\hat{\mathbb{H}}_{e}^{\boldsymbol{N}}]$. Notice that these sensitivities not only are interesting in order to analyse the effect that macroscale fields have on microscale fields, but also are instrumental in order to compute the effective constitutive tensors, as it will be shown in the following section.

4.4. Effective constitutive tensors

Let us recall the term $\mathcal{D}_{\text{int}}$ in the macroscopic dissipation inequality $\mathcal{D}$ in equation (75), i.e.,

$$\mathcal{D}_{\text{int}}=\boldsymbol{P}:\delta\boldsymbol{F}+\boldsymbol{E}_0\cdot\delta\boldsymbol{D}_0.\tag{92}$$

Making use of the relation between the first Piola-Kirchhoff stress tensor and the electric displacement fields in the microscale and the macroscale in equation $(80)_a$, $\mathcal{D}_{\text{int}}$ can be expressed as

$$\begin{aligned}\mathcal{D}_{\text{int}} &= \Big(c^a \boldsymbol{P}^a + c^b \boldsymbol{P}^b\Big) : \delta\boldsymbol{F} + \Big(c^a \boldsymbol{E}_0^a + c^b \boldsymbol{E}_0^b\Big) \cdot \delta\boldsymbol{D}_0; \\ &= \Big(c^a \Big(\boldsymbol{P}^{a,h} + \boldsymbol{P}^{a,v}\Big) + c^b \Big(\boldsymbol{P}^{b,h} + \boldsymbol{P}^{b,v}\Big)\Big) : \delta\boldsymbol{F} + \Big(c^a \boldsymbol{E}_0^a + c^b \boldsymbol{E}_0^b\Big) \cdot \delta\boldsymbol{D}_0.\end{aligned} \tag{93}$$

Careful re-arrangement of (93) yields

$$\mathcal{D}_{\text{int}} = c^a\Big(\underbrace{\boldsymbol{P}^{a,h} : \delta\boldsymbol{F} + \boldsymbol{E}_0^a \cdot \delta\boldsymbol{D}_0}_{\widetilde{\mathcal{D}}_{\text{int}}^{a,h}} + \underbrace{\boldsymbol{P}^{a,v} : \delta\boldsymbol{F}}_{\widetilde{\mathcal{D}}_{\text{int}}^{a,v}}\Big) + c^b\Big(\underbrace{\boldsymbol{P}^{b,h} : \delta\boldsymbol{F} + \boldsymbol{E}_0^b \cdot \delta\boldsymbol{D}_0}_{\widetilde{\mathcal{D}}_{\text{int}}^{b,h}} + \underbrace{\boldsymbol{P}^{b,v} : \delta\boldsymbol{F}}_{\widetilde{\mathcal{D}}_{\text{int}}^{b,v}}\Big), \tag{94}$$

where in above equation we have used the notation $\{\widetilde{\mathcal{D}}_{\text{int}}^{a,h}, \widetilde{\mathcal{D}}_{\text{int}}^{a,v}, \widetilde{\mathcal{D}}_{\text{int}}^{b,h}, \widetilde{\mathcal{D}}_{\text{int}}^{b,v}\}$ to distinguish them from $\{\mathcal{D}_{\text{int}}^a, \mathcal{D}_{\text{int}}^b\}$ in (70). The directional derivative of $\mathcal{D}_{\text{int}}$ in (94) adopts the form, after careful computation following the idea of [58]:

$$D\mathcal{D}_{\text{int}}[\delta\boldsymbol{F}, \delta\boldsymbol{D}_0] = \begin{bmatrix}\delta\boldsymbol{F} : & \delta\boldsymbol{D}_0 \cdot\end{bmatrix} \left([\bar{\mathbb{H}}_e] - [\tilde{\mathbb{H}}_e]\right) \begin{bmatrix} : \delta\boldsymbol{F} \\ \delta\boldsymbol{D}_0 \end{bmatrix}, \tag{95}$$

with $[\bar{\mathbb{H}}_e]$ and $[\tilde{\mathbb{H}}_e]$ given by $[\bar{\mathbb{H}}_e] = c^a[\bar{\mathbb{H}}_e^a] + c^b[\bar{\mathbb{H}}_e^b]$ and

$$[\tilde{\mathbb{H}}_e] = \begin{bmatrix} [\![\boldsymbol{\mathcal{C}}_{e,\bullet\boldsymbol{N}}]\!] & [\![\boldsymbol{\mathcal{Q}}]\!]^T \boldsymbol{\mathcal{T}}_{\boldsymbol{N}} \\ [\![\boldsymbol{\mathcal{Q}}]\!]\boldsymbol{N} & [\![\boldsymbol{\theta}]\!]\boldsymbol{\mathcal{T}}_{\boldsymbol{N}} \end{bmatrix} [\check{\mathbb{H}}_e^{\boldsymbol{N}}]^{-1} \begin{bmatrix} [\![\boldsymbol{\mathcal{C}}_{e,\boldsymbol{N}\bullet}]\!] & \boldsymbol{N} \cdot [\![\boldsymbol{\mathcal{Q}}]\!]^T \\ \boldsymbol{\mathcal{T}}_{\boldsymbol{N}}{}^T [\![\boldsymbol{\mathcal{Q}}]\!] & \boldsymbol{\mathcal{T}}_{\boldsymbol{N}}{}^T [\![\boldsymbol{\theta}]\!] \end{bmatrix}; \quad [\check{\mathbb{H}}_e] = \frac{1}{c^a}[\mathbb{H}_e^a] + \frac{1}{c^b}[\mathbb{H}_e^b] = \begin{bmatrix} \check{\boldsymbol{\mathcal{C}}}_e^h + \check{\boldsymbol{\mathcal{C}}}_e^v & \check{\boldsymbol{\mathcal{Q}}}^T \\ \check{\boldsymbol{\mathcal{Q}}} & \check{\boldsymbol{\theta}} \end{bmatrix}, \tag{96}$$

where $(\boldsymbol{\mathcal{C}}_{e,\bullet\boldsymbol{N}})_{ijJ} = (\boldsymbol{\mathcal{C}}_e)_{iIjJ} N_J$.

Hence, equation (95) reveals that the effective constitutive tensors $\{\boldsymbol{\mathcal{C}}_e, \boldsymbol{\mathcal{Q}}, \boldsymbol{\theta}\}$ can be additively decomposed into two distinct contributions: a simple average of the individual phases in the microscale, and an additional term associated with the sensitivities of the (micro) amplitude vectors $\{\boldsymbol{\alpha}, \boldsymbol{\beta}\}$ with respect to the macroscopic deformation gradient tensor $\boldsymbol{F}$ and electric displacement field $\boldsymbol{D}_0$. We will demonstrate that the first contribution (simple averaging of micro-constituents) complies with the ellipticity condition provided that the hyperelastic contribution of the internal energy density functions $e^{a,h}(\boldsymbol{F}^a, \boldsymbol{D}_0^a)$ and $e^{b,h}(\boldsymbol{F}^b, \boldsymbol{D}_0^b)$ are CMV compliant, since the viscous contribution of the energy density adds an unconditionally elliptic (regularising) contribution for the Backward-Euler, semi-analytical integration, and Forward-Euler methods discussed in Section 3.4. However, for the Crank-Nicolson scheme, the viscous contribution has a regularisation effect provided that condition in equation (47) is satisfied. However, the second term, related with $[\tilde{\mathbb{H}}_e]$ can potentially induce loss of ellipticity of the homogenised tangent operator. Specifically,

$$\begin{aligned}\boldsymbol{\mathcal{C}}_e = &\underbrace{\bar{\boldsymbol{\mathcal{C}}}_e{}^h(c^a, c^b, \boldsymbol{F}^a, \boldsymbol{F}^b, \boldsymbol{D}_0^a, \boldsymbol{D}_0^b) + \bar{\boldsymbol{\mathcal{C}}}_e{}^v(c^a, c^b, \boldsymbol{F}^a, \boldsymbol{F}^b, \boldsymbol{\mathcal{A}}^a, \boldsymbol{\mathcal{A}}^b)}_{\text{(Average) } \textbf{ellipticity-preserving} \text{ contr.}} \\ &- \underbrace{\Big(\tilde{\boldsymbol{\mathcal{C}}}_e{}^h(c^a, c^b, \boldsymbol{F}^a, \boldsymbol{F}^b, \boldsymbol{D}_0^a, \boldsymbol{D}_0^b) + \tilde{\boldsymbol{\mathcal{C}}}_e{}^v(c^a, c^b, \boldsymbol{F}^a, \boldsymbol{F}^b \boldsymbol{\mathcal{A}}^a, \boldsymbol{\mathcal{A}}^b)\Big)}_{\text{Macro } \textbf{ellipticity-breaking} \text{ contr.}}; \\ \boldsymbol{\mathcal{Q}} = &\underbrace{\bar{\boldsymbol{\mathcal{Q}}}(c^a, c^b, \boldsymbol{F}^a, \boldsymbol{F}^b, \boldsymbol{D}_0^a, \boldsymbol{D}_0^b)}_{\text{(Average) } \textbf{ellipticity-preserving} \text{ contr.}} - \underbrace{\tilde{\boldsymbol{\mathcal{Q}}}(c^a, c^b, \boldsymbol{F}^a, \boldsymbol{F}^b, \boldsymbol{D}_0^a, \boldsymbol{D}_0^b)}_{\text{Macro } \textbf{ellipticity-breaking} \text{ contr.}}; \\ \boldsymbol{\theta} = &\underbrace{\bar{\boldsymbol{\theta}}(c^a, c^b, \boldsymbol{F}^a, \boldsymbol{F}^b, \boldsymbol{D}_0^a, \boldsymbol{D}_0^b)}_{\text{(Average) } \textbf{ellipticity-preserving} \text{ contr.}} - \underbrace{\tilde{\boldsymbol{\theta}}(c^a, c^b, \boldsymbol{F}^a, \boldsymbol{F}^b, \boldsymbol{D}_0^a, \boldsymbol{D}_0^b)}_{\text{Macro } \textbf{ellipticity-breaking} \text{ contr.}}.\end{aligned} \tag{97}$$

As for the average-type term in (95), adopting $\delta\boldsymbol{F} = \boldsymbol{u} \otimes \boldsymbol{V}$ and $\delta\boldsymbol{D}_0 = \boldsymbol{V}_\perp$, it is immediate to realise that

$$[\boldsymbol{u} \otimes \boldsymbol{V} : \boldsymbol{V}_\perp \cdot] [\bar{\mathbb{H}}_e] \begin{bmatrix} : \boldsymbol{u} \otimes \boldsymbol{V} \\ \boldsymbol{V}_\perp \end{bmatrix} > 0; \qquad \forall \boldsymbol{u}, \boldsymbol{V}, \boldsymbol{V}_\perp, \tag{98}$$

provided that the the hyperelastic contribution of the internal energy density function, namely $e^{a,h}$ and $e^{b,h}$ are CMV. Proceeding in an analogous manner with the jump-type contribution, it results in

$$[\boldsymbol{u}\otimes\boldsymbol{V}:\boldsymbol{V}_\perp\cdot]\,[\tilde{\mathbb{H}}_e]\begin{bmatrix}:\boldsymbol{u}\otimes\boldsymbol{V}\\ \boldsymbol{V}_\perp\end{bmatrix} = -\underbrace{\begin{bmatrix}\boldsymbol{u}\cdot & \boldsymbol{v}\cdot\end{bmatrix}\begin{bmatrix}[\![\boldsymbol{\mathcal{C}}_{e,\boldsymbol{VN}}]\!] & \boldsymbol{V}\cdot[\![\boldsymbol{\mathcal{Q}}]\!]^T\boldsymbol{\mathcal{T}}_{\boldsymbol{N}}\\ \boldsymbol{\mathcal{T}}_{\boldsymbol{V}}{}^T[\![\boldsymbol{\mathcal{Q}}]\!]\boldsymbol{N} & \boldsymbol{\mathcal{T}}_{\boldsymbol{V}}{}^T[\![\boldsymbol{\theta}]\!]\boldsymbol{\mathcal{T}}_{\boldsymbol{N}}\end{bmatrix}}_{\begin{bmatrix}\boldsymbol{a}\cdot & \boldsymbol{b}\cdot\end{bmatrix}}[\check{\mathbb{H}}_e^{\boldsymbol{N}}]^{-1}\underbrace{\begin{bmatrix}[\![\boldsymbol{\mathcal{C}}_{e,\boldsymbol{NV}}]\!] & \boldsymbol{N}\cdot[\![\boldsymbol{\mathcal{Q}}]\!]^T\boldsymbol{\mathcal{T}}_{\boldsymbol{V}}\\ \boldsymbol{\mathcal{T}}_{\boldsymbol{N}}{}^T[\![\boldsymbol{\mathcal{Q}}]\!]\boldsymbol{V} & \boldsymbol{\mathcal{T}}_{\boldsymbol{N}}{}^T[\![\boldsymbol{\theta}]\!]\boldsymbol{\mathcal{T}}_{\boldsymbol{V}}\end{bmatrix}\begin{bmatrix}\boldsymbol{u}\\ \boldsymbol{v}\end{bmatrix}}_{\begin{bmatrix}\boldsymbol{a}\\ \boldsymbol{b}\end{bmatrix}}$$

$$= -\begin{bmatrix}\boldsymbol{a}\cdot & \boldsymbol{b}\cdot\end{bmatrix}[\check{\mathbb{H}}_e^{\boldsymbol{N}}]^{-1}\begin{bmatrix}\boldsymbol{a}\\ \boldsymbol{b}\end{bmatrix} < 0; \qquad \forall\boldsymbol{u},\boldsymbol{V},\boldsymbol{V}_\perp, \tag{99}$$

where use of the projection operator $\boldsymbol{\mathcal{T}}_{\boldsymbol{V}}$ (i.e., $\boldsymbol{V}_\perp = \boldsymbol{\mathcal{T}}_{\boldsymbol{V}}\boldsymbol{v}$) has been made in the equation above, and vectors $\boldsymbol{a}$ and $\boldsymbol{b}$ have been introduced. It is immediate to realise that above term is negative due to the positive definiteness of the Hessian $[\check{\mathbb{H}}_e^{\boldsymbol{N}}]$. It is at this juncture when it is important to emphasise the use that we have made of [58, Remark 4] in order to drastically simplify the algebra associated with above computation. In summary,

(a) the consideration of CMV (and thus elliptic) constitutive models for the microscale constituents in both phases guarantees that the analytical homogenisation (computation of the micro-amplitude vectors $\{\boldsymbol{\alpha},\boldsymbol{\beta}\}$) can be accomplished for any value of the macroscopic fields $\{\boldsymbol{F},\boldsymbol{D}_0\}$. This is also favoured by the viscous contribution of the energy density, which adds an unconditionally elliptic (regularising) contribution when using the Backward-Euler, semi-analytical integration, and Forward-Euler methods discussed in Section 3.4. However, for the Crank-Nicolson scheme, the viscous contribution has a regularisation effect provided that condition in equation (47) is satisfied.

(b) the high nonlinearity associated with the microscopic problem can result in an intricate dependence of both $\{\boldsymbol{\alpha},\boldsymbol{\beta}\}$ upon $\{\boldsymbol{F},\boldsymbol{D}_0\}$, permitting the contributions $\{\tilde{\boldsymbol{\mathcal{C}}}_e,\tilde{\boldsymbol{\mathcal{Q}}},\tilde{\boldsymbol{\theta}}\}$ in (97) to potentially induce an overall loss of ellipticity (or rank-one convexity condition) of the effective tensors $\{\boldsymbol{\mathcal{C}}_e,\boldsymbol{\mathcal{Q}},\boldsymbol{\theta}\}$, by neutralising, and even counterbalancing, the unconditionally elliptic contribution resulting from the averaging of the micro-constituents $\{\bar{\boldsymbol{\mathcal{C}}}_e,\bar{\boldsymbol{\mathcal{Q}}},\bar{\boldsymbol{\theta}}\}$.

The mathematical connotations associated with point (b) above imply that the homogenisation procedure can eventually jeopardise the well-posedness of the system in (7). From a physical standpoint, as shown in [8], the onset of loss of ellipticity corresponds with the development of localised deformations, and it is an *expected phenomenon* related to the development of long wavelength diffuse modes in the microscale. Indeed, loss of ellipticity can occur in the solely mechanical case, even when (polyconvex) Neo-Hookean strain energies are considered for the constitutive models of the micro-constituents of layered composites (see Reference [29]). In the numerical examples considered in this paper, loss of ellipticity has not been observed.

Finally, it is interesting to observe that the viscous contribution is present not only in the ellipticity-preserving term $[\bar{\mathbb{H}}_e]$ in (95) but also in the ellipticity-breaking contribution associated with $[\check{\mathbb{H}}_e]$. This entails that, although the viscous contribution adds a regularising effect in the first term, i.e., $[\bar{\mathbb{H}}_e]$, it also adds a non-elliptic contribution to the second term. Nonetheless, it is expected that the regularising contribution in the simple averaged term $[\bar{\mathbb{H}}_e]$ will help to delay the ellipticity breaking effect of the homogenisation (second term $[\check{\mathbb{H}}_e]$) and that therefore, the onset of loss of ellipticity when considering visco-elastic effects will occur, in principle, later than in the reversible case (no viscous effects considered). The latter will be explored in the numerical examples section.

5. Variational formulation and finite element implementation

We introduce the functional spaces for the fields $\{\boldsymbol{\phi},\varphi\}\in\mathbb{V}^{\boldsymbol{\phi}}\times\mathbb{V}^{\varphi}$ and the test functions $\{\delta\boldsymbol{\phi},\delta\varphi\}\in\mathbb{V}_0^{\boldsymbol{\phi}}\times\mathbb{V}_0^{\varphi}$, namely.

$$\begin{aligned}
&\mathbb{V}^{\boldsymbol{\phi}} = \left\{\boldsymbol{\phi}:\mathcal{B}_0\to\mathbb{R}^3;\quad (\boldsymbol{\phi})_i\in H^1(\mathcal{B}_0)\ \mid J>0\right\}; && \mathbb{V}^{\varphi} = \left\{\varphi:\mathcal{B}_0\to\mathbb{R}^1;\quad \varphi\in H^1(\mathcal{B}_0)\right\};\\
&\mathbb{V}_0^{\boldsymbol{\phi}} = \left\{\forall\boldsymbol{\phi}\in\mathbb{V}^{\boldsymbol{\phi}};\quad \boldsymbol{\phi}=\boldsymbol{0}\text{ on }\partial_{\boldsymbol{\phi}}\mathcal{B}_0\right\}; && \mathbb{V}_0^{\varphi} = \left\{\forall\varphi\in\mathbb{V}^{\varphi};\quad \varphi=0\text{ on }\partial_{\varphi}\mathcal{B}_0\right\}.
\end{aligned} \tag{100}$$

The weak forms associated with the PDEs in equation (7) can then be recast as

$$\begin{aligned}\mathcal{W}_{\boldsymbol{\phi}} &= \int_{\mathcal{B}_0} \boldsymbol{P} : D\boldsymbol{F}[\delta\boldsymbol{\phi}]\, dV - \int_{\mathcal{B}_0} \boldsymbol{f}_0 \cdot \delta\boldsymbol{\phi}\, dV - \int_{\partial_{\boldsymbol{t}}\mathcal{B}_0} \boldsymbol{t}_0 \cdot \delta\boldsymbol{\phi}\, dA = 0;\\ \mathcal{W}_{\varphi} &= \int_{\mathcal{B}_0} \boldsymbol{D}_0 \cdot \boldsymbol{\nabla}_0 \delta\varphi\, dV + \int_{\mathcal{B}_0} \rho_0^e \delta\varphi\, dV + \int_{\partial_\omega \mathcal{B}_0} \omega_0^e \delta\varphi\, dA = 0,\end{aligned} \tag{101}$$

with $\boldsymbol{D}_0$ obtained making use of equation (80), namely

$$\boldsymbol{E}_0 = -\boldsymbol{\nabla}_0\varphi = c^a \partial_{D_0^a} e^a\Big(\boldsymbol{F}^a, \boldsymbol{D}_0^a, \boldsymbol{\mathcal{A}}^a(\boldsymbol{F}^a)\Big) + c^b \partial_{D_0^b} e^b\Big(\boldsymbol{F}^b, \boldsymbol{D}_0^b, \boldsymbol{\mathcal{A}}^b(\boldsymbol{F}^b)\Big), \tag{102}$$

by means of the consideration of the relationships in (65) between $\{\boldsymbol{F}^a, \boldsymbol{F}^b, \boldsymbol{D}_0^a, \boldsymbol{D}_0^b\}$ with $\{\boldsymbol{F}, \boldsymbol{D}_0\}$, and after solving the amplitude vectors according to Section 4.2. Then, solution of macroscopic field $\boldsymbol{D}_0$ permits to determine the macroscopic first Piola-Kirchhoff stress tensor $\boldsymbol{P}$ according to equation (80), namely

$$\boldsymbol{P} = c^a \partial_{\boldsymbol{F}^a} e^a\Big(\boldsymbol{F}^a, \boldsymbol{D}_0^a, \boldsymbol{\mathcal{A}}^a(\boldsymbol{F}^a)\Big) + c^b \partial_{\boldsymbol{F}^b} e^b\Big(\boldsymbol{F}^b, \boldsymbol{D}_0^b, \boldsymbol{\mathcal{A}}^b(\boldsymbol{F}^b)\Big). \tag{103}$$

A Newton-Raphson scheme can be used for the solution of the weak forms in (101), which implies the following linearisation with respect to incremental fields $\Delta\boldsymbol{\phi} \in \mathbb{V}_0^{\boldsymbol{\phi}}$ and $\Delta\varphi \in \mathbb{V}_0^{\varphi}$

$$0 = \mathcal{W}_{\boldsymbol{\phi}} + \mathcal{W}_{\varphi} + D\mathcal{W}_{\boldsymbol{\phi}}[\Delta\boldsymbol{\phi}] + D\mathcal{W}_{\boldsymbol{\phi}}[\Delta\varphi] + D\mathcal{W}_{\varphi}[\Delta\boldsymbol{\phi}] + D\mathcal{W}_{\varphi}[\Delta\varphi], \tag{104}$$

with

$$\begin{aligned} D\mathcal{W}_{\boldsymbol{\phi}}[\Delta\boldsymbol{\phi}] &= \int_{\mathcal{B}_0} \boldsymbol{\nabla}_0\delta\boldsymbol{\phi} : \boldsymbol{\mathcal{C}} : \boldsymbol{\nabla}_0\Delta\boldsymbol{\phi}\, dV; & D\mathcal{W}_{\boldsymbol{\phi}}[\Delta\varphi] &= \int_{\mathcal{B}_0} \left(\boldsymbol{\nabla}_0\delta\boldsymbol{\phi} : \boldsymbol{\mathcal{P}}^T\right) \cdot \boldsymbol{\nabla}_0\Delta\varphi\, dV;\\ D\mathcal{W}_{\varphi}[\Delta\boldsymbol{\phi}] &= \int_{\mathcal{B}_0} \boldsymbol{\nabla}_0\delta\varphi \cdot (\boldsymbol{\mathcal{P}} : \boldsymbol{\nabla}_0\Delta\boldsymbol{\phi})\, dV; & D\mathcal{W}_{\varphi}[\Delta\varphi] &= -\int_{\mathcal{B}_0} \boldsymbol{\nabla}_0\delta\varphi \cdot (\boldsymbol{\epsilon}\boldsymbol{\nabla}_0\Delta\varphi)\, dV, \end{aligned} \tag{105}$$

with the homogenised tensors $\{\boldsymbol{\mathcal{C}}, \boldsymbol{\mathcal{P}}, \boldsymbol{\epsilon}\}$ related to their homogenised internal energy-based counterparts $\{\boldsymbol{\mathcal{C}}_e, \boldsymbol{\mathcal{Q}}, \boldsymbol{\theta}\}$ in (97) through the relationship in equation (57). Equation (104) permits the update of the solution fields $\boldsymbol{\phi} \in \mathbb{V}^{\boldsymbol{\phi}}$ and $\varphi \in \mathbb{V}^{\varphi}$ at a given Newton-Raphson iteration $k+1$ as

$$\boldsymbol{\phi}^{k+1} = \boldsymbol{\phi}^k + \Delta\boldsymbol{\phi}; \qquad \varphi^{k+1} = \varphi^k + \Delta\varphi. \tag{106}$$

As standard in finite elements, the domain $\mathcal{B}_0$ described in Section 2.1, representing the EAP, is sub-divided into a finite set of non-overlapping elements $e \in \mathbb{E}$ as follows

$$\mathcal{B}_0 \approx \mathcal{B}_0^h = \bigcup_{e\in\mathbb{E}} \mathcal{B}_0^e. \tag{107}$$

The unknown fields $\{\boldsymbol{\phi}, \varphi\}$, and the test functions $\{\delta\boldsymbol{\phi}, \delta\varphi\}$ featuring in (101), are discretised using the functional spaces $\mathbb{V}^{\boldsymbol{\phi}^h} \times \mathbb{V}^{\varphi^h}$ and $\mathbb{V}_0^{\boldsymbol{\phi}^h} \times \mathbb{V}_0^{\varphi^h}$, respectively, defined as

$$\begin{aligned} \mathbb{V}^{\boldsymbol{\phi}^h} &= \left\{ \boldsymbol{\phi} \in \mathbb{V}^{\boldsymbol{\phi}};\quad \boldsymbol{\phi}^h\Big|_{\mathcal{B}_0^e} = \sum_{a=1}^{n_{\text{node}}^{\boldsymbol{\phi}}} N_a^{\boldsymbol{\phi}} \boldsymbol{\phi}_a \right\}; & \mathbb{V}^{\varphi^h} &= \left\{ \varphi \in \mathbb{V}^{\varphi};\quad \varphi^h\Big|_{\mathcal{B}_0^e} = \sum_{a=1}^{n_{\text{node}}^{\varphi}} N_a^{\varphi} \varphi_a \right\};\\ \mathbb{V}_0^{\boldsymbol{\phi}^h} &= \left\{ \forall\boldsymbol{\phi} \in \mathbb{V}^{\boldsymbol{\phi}^h};\quad \boldsymbol{\phi} = \boldsymbol{0} \text{ on } \partial_{\boldsymbol{\phi}}\mathcal{B}_0 \right\}; & \mathbb{V}_0^{\varphi^h} &= \left\{ \forall\varphi \in \mathbb{V}^{\varphi^h};\quad \varphi = 0 \text{ on } \partial_{\varphi}\mathcal{B}_0 \right\}, \end{aligned} \tag{108}$$

where, for any field $\boldsymbol{\mathcal{Y}} \in \{\boldsymbol{\phi}, \varphi\}$, $n_{\text{node}}^{\boldsymbol{\mathcal{Y}}}$ denotes the number of nodes per element of the discretisation associated with the field $\boldsymbol{\mathcal{Y}}$; and $N_a^{\boldsymbol{\mathcal{Y}}} : \mathcal{B}_0^e \to \mathbb{R}$, the a^{th} shape function used for the interpolation of $\boldsymbol{\mathcal{Y}}$. In addition, $\boldsymbol{\mathcal{Y}}_a$ represents the value of the field $\boldsymbol{\mathcal{Y}}$ at the a^{th} node of a given finite element. Consideration of the functional spaces in (108) enables the weak forms $\mathcal{W}_{\boldsymbol{\phi}}$, $\mathcal{W}_{\varphi}$ in (101) to be written in terms of their associated elemental residual contributions, namely

$$\mathcal{W}_{\boldsymbol{\phi}} = \sum_{e=1}^{N} \delta\boldsymbol{\phi}_a \cdot \boldsymbol{R}_{a,e}^{\boldsymbol{\phi}}; \qquad \mathcal{W}_{\varphi} = \sum_{e=1}^{N} \delta\varphi_a R_{a,e}^{\varphi}, \tag{109}$$

where N denotes the number of elements for the underlying discretisation, and where each of the residual contributions $\boldsymbol{R}^{\boldsymbol{\phi}}_{a,e}$ and $R^{\varphi}_{a,e}$ can be expressed as[12]

$$\boldsymbol{R}^{\boldsymbol{\phi}}_{a,e} = \int_{\mathcal{B}^e_0} \boldsymbol{P}\boldsymbol{\nabla}_0 N^{\boldsymbol{\phi}}_a \, dV + \int_{\mathcal{B}^e_0} N^{\boldsymbol{\phi}}_a \boldsymbol{f}_0 \, dV; \qquad R^{\varphi}_{a,e} = \int_{\mathcal{B}^e_0} \boldsymbol{D}_0 \cdot \boldsymbol{\nabla}_0 N^{\varphi}_a \, dV + \int_{\mathcal{B}^e_0} N^{\varphi}_a \rho^e \, dV. \tag{110}$$

Discretisation of the test functions and incremental fields permits equation (105) to be written in terms of their associated elemental stiffness contributions, namely

$$\begin{aligned} D\mathcal{W}_{\boldsymbol{\phi}}[\Delta\boldsymbol{\phi}] &= \sum_{e=1}^{N} \delta\boldsymbol{\phi}_a \cdot \boldsymbol{K}^{\boldsymbol{\phi}\boldsymbol{\phi}}_{ab,e} \Delta\boldsymbol{\phi}_b; \qquad D\mathcal{W}_{\boldsymbol{\phi}}[\Delta\varphi] = \sum_{e=1}^{N} \delta\boldsymbol{\phi}_a \cdot \boldsymbol{K}^{\boldsymbol{\phi}\varphi}_{ab,e} \Delta\varphi_b; \\ D\mathcal{W}_{\varphi}[\Delta\boldsymbol{\phi}] &= \sum_{e=1}^{N} \delta\varphi_a \cdot \boldsymbol{K}^{\varphi\boldsymbol{\phi}}_{ab,e} \Delta\boldsymbol{\phi}_b; \qquad D\mathcal{W}_{\varphi}[\Delta\varphi] = \sum_{e=1}^{N} \delta\varphi_a K^{\varphi\varphi}_{ab,e} \Delta\varphi_b, \end{aligned} \tag{111}$$

where each of the stiffness contributions is expressed as

$$\begin{aligned} \left(\boldsymbol{K}^{\boldsymbol{\phi}\boldsymbol{\phi}}_{ab,e}\right)_{ij} &= \int_{\mathcal{B}^e_0} \left(\boldsymbol{\nabla}_0 N^{\boldsymbol{\phi}}_a\right)_I \left(\boldsymbol{\nabla}_0 N^{\boldsymbol{\phi}}_b\right)_J \mathcal{C}_{iIjJ} \, dV; \qquad \left(\boldsymbol{K}^{\boldsymbol{\phi}\varphi}_{ab,e}\right)_i = \int_{\mathcal{B}^e_0} \left(\boldsymbol{\nabla}_0 N^{\boldsymbol{\phi}}_a\right)_I \left(\boldsymbol{\nabla}_0 N^{\varphi}_b\right)_J (\boldsymbol{\mathcal{P}})^T_{iIJ} \, dV; \\ \boldsymbol{K}^{\varphi\boldsymbol{\phi}}_{ab,e} &= \left(\boldsymbol{K}^{\varphi\boldsymbol{\phi}}_{ab,e}\right)^T; \qquad K^{\varphi\varphi}_{ab,e} = -\int_{\mathcal{B}^e_0} \boldsymbol{\nabla}_0 N^{\varphi}_a \cdot \boldsymbol{\epsilon} \boldsymbol{\nabla}_0 N^{\varphi}_b \, dV. \end{aligned} \tag{112}$$

6. Numerical examples

In this Section, three numerical examples will be presented in order to assess the capability and robustness of the proposed computational framework. The structure of the numerical examples has been chosen similar to that in [58] in order to facilitate the understanding of the effects that the consideration of time-dependent viscoelastic effects in the material has with respect to the hyperelastic case. The first numerical example, restricted to the case of homogeneous deformation, studies the behaviour of the homogenised constitutive model without the need to resort to a finite element discretisation. The rate-dependent response of the material is observed in terms of the orientation of the laminate, with a loading-unloading and a loading-relaxation tests, both of them studied for purely mechanical (no electric effect) and electro-mechanical cases. The second example abandons the assumption of uniform deformation and explores the use of finite elements in the context of a rectangular flexible DE composite film displaying complex actuation patterns through application of electrical stimuli. In addition, a thorough study will be conducted, where different microscopic arrangements will be shown to lead to potentially very different actuating configurations (namely bending, torsion, stretching), and the viscoelastic effects will produce a different response to the (reversible) hyperelastic material, magnifying one mode of deformation with respect to others. Finally, the third numerical example explores the onset of buckling-type instabilities in DE composites, and this will be studied for a square membrane configuration. In this case, the viscous contribution acts as a regularising term that allows the material to reach a larger deformation overcoming some instabilities that happen in the hyperelastic case. The three numerical examples help understand the complex deformation patterns that occur when laminated composites are subjected to electric fields and the effect that introduces the consideration of viscoelasticity.

The hyperelastic properties of the materials considered for all numerical examples are listed in Table 2, being the properties of a widely used dielectric elastomer, VHB-4910. The viscoelastic properties are modelled through Maxwell branches with properties listed in Table 3, following the characterisation in [9].

[12] For simplicity, the external contributions on the boundary of the continuum associated with $\boldsymbol{t}_0$ and ω^e_0 have not been included in (110).

Properties	Phase a		Phase b		Units
Mechanical parameters	μ_1^a	1.4×10^4	μ_1^b	5.7×10^4	Pa
	μ_2^a	0	μ_2^b	0	Pa
	λ^a	4.2×10^4	λ^b	1.7×10^5	Pa
Electrical parameters	ϵ_r^a	4.8	ϵ_r^b	22.6	-
Concentration	c^a	0.5	c^b	0.5	-

Table 2: Numerical examples. Material parameters of the model for each phase (see (25), (26)).

Branch	μ^v (Pa)	τ^v (s)
1	5.8×10^4	6.2×10^{-1}
2	2.1×10^4	1.4×10^1
3	1.3×10^4	2.0×10^2

Table 3: Numerical examples. Properties of Maxwell branches (see (28), (29)).

6.1. Numerical example 1: homogeneous electro-deformation of a multi-layered DE composite with consideration of viscoelastic effects

Through this example we aim to:

- Study the hysteresis effect in rank-one laminated composite materials with the consideration of viscoelastic effects, both for purely mechanical and electromechanical loading, in terms of the properties of the composite material.
- Observe that after a relaxation period the rank-one laminated composite material converges to the hyperelastic response.

First, we consider the prototypical set-up similar to that explored by [9, 41, 42], where no electrical effects are considered. This consists of a rank-one DE laminated film, such as the one depicted in Figure 6, which is subjected to a homogeneous state of deformation.

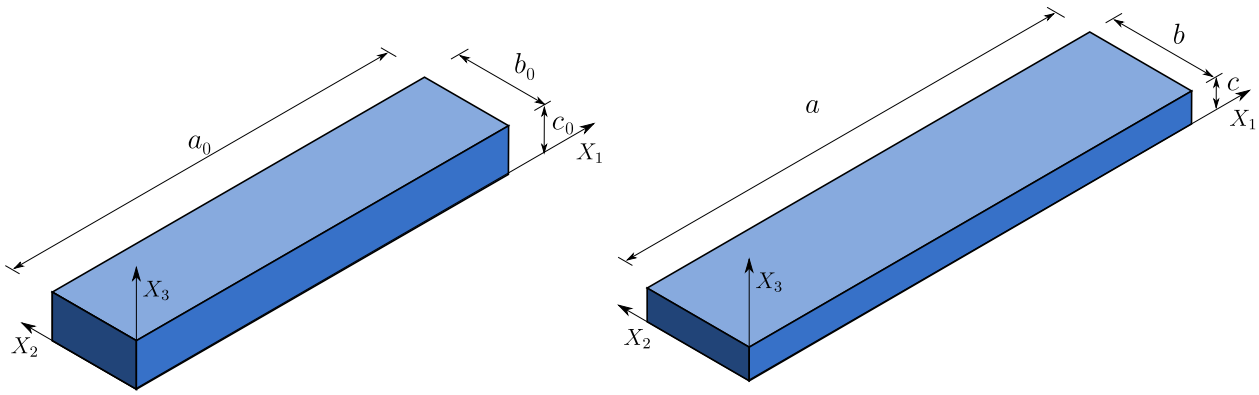

Figure 3: Numerical example 1: First configuration. Experimental set-up. The DE laminated composite material is subjected to a stretch along OX_1 direction.

Maintaining stress-free conditions, there is a state of uniform deformation across the film. This uniform state of deformation is exploited in order to study the response of the DE rank-one laminate from a local point of view, without the need to resort to a finite element discretisation. As a result, in the absence of any further loads, the homogeneous solution to this problem corresponds to the stationary point $\{\boldsymbol{F}^*\}$ of the energy functional defined as

$$\Pi\left(\boldsymbol{F}^*\right) = \inf_{\boldsymbol{F}} \left\{e\left(\boldsymbol{F}\right)\right\}. \tag{113}$$

Thus, the stationary condition of above functional arises as

$$\boldsymbol{\mathcal{R}}_{\boldsymbol{F}}\left(\boldsymbol{F}\right) = \partial_{\boldsymbol{F}} e = \boldsymbol{0}. \tag{114}$$

The above nonlinear stationary condition (114) is solved in terms of unknown $\boldsymbol{F}^*$. Specifically, $\boldsymbol{F}$ is formulated as

$$\boldsymbol{F} = \begin{bmatrix} \lambda & 0 & 0 \\ 0 & 1 & 0 \\ 0 & 0 & F_{33} \end{bmatrix}. \tag{115}$$

First, a loading-unloading experiment is carried out. This experiment is usually used to calibrate the material properties by comparing the result against a real experiment in the lab. The E_{11} component of the Green-Lagrange strain tensor $\boldsymbol{E} = \frac{1}{2}(\boldsymbol{C} - \boldsymbol{I})$ is defined as

$$E_{11} = \frac{1}{2}(\lambda^2 - 1) \Rightarrow \dot{E}_{11} = \lambda\dot{\lambda} \approx \lambda \left(\frac{\lambda - \lambda_n}{\Delta t} \right), \tag{116}$$

where λ_n represents the stretch in the previous time step and Δt the time step used. Re-arrangement of terms in (116) permits to obtain the following second degree equation for the stretch λ in the current time step as

$$\lambda^2 - \lambda_n \lambda - \dot{E}_{11}\Delta t = 0, \tag{117}$$

whose admissible solution is

$$\lambda = \frac{\lambda_n}{2} \left(1 + \sqrt{1 + \frac{4\dot{E}_{11}\Delta t}{\lambda_n^2}} \right). \tag{118}$$

In this example, $\dot{E}_{11} = 0.1 s^{-1}$ is selected, and the loading is applied until the deformation reaches a maximum stretch of $\lambda_{max} = 3$, being then unloaded at the same rate.

In Figure 4, it is shown how the orientation of the laminate affects the deformation of the composite material, for both the change in $\bar{\beta}$ (Figure 4a) and $\bar{\alpha}$ (Figure 4b). The nominal stress is represented in terms of the stretch. It is observed how, the larger the angle of orientation of the laminate $\bar{\beta}$, the smaller the stress attained is. On the contrary, an increase in the $\bar{\alpha}$ angle for fixed $\bar{\beta}$ is translated into an increase in the stretch.

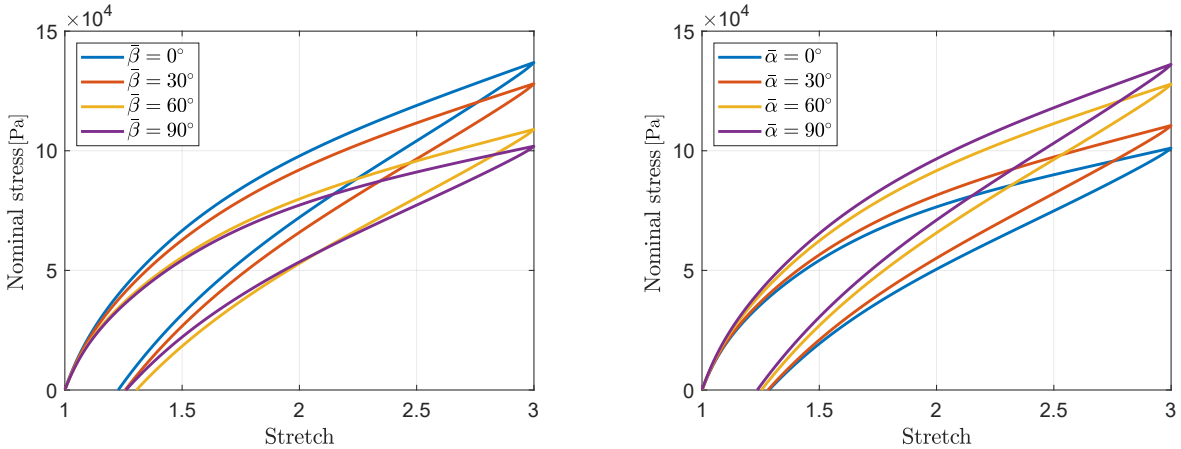

Figure 4: Numerical example 1. Mechanical case. Loading-unloading test for maximum stretch $\lambda_{max} = 3$, strain rate $\dot{E}_{11} = 0.1 s^{-1}$, and orientation of the laminated composite given by angles: (a) $\bar{\alpha} = 0°$ and $\bar{\beta}$ let to vary. (b) $\bar{\beta} = 75°$ and $\bar{\alpha}$ let to vary.

Next, a relaxation experiment is carried out. The material is subjected to a mechanical load until it reaches its maximum value of stretch $\lambda_{max} = 3$, at a strain rate of $\dot{E}_{11} = 0.1 s^{-1}$. Then, the load is kept for enough time for the nominal stress to reach a stationary point. In Figure 5, the effect of the orientation of the laminate is observed, for both the change in $\bar{\beta}$ (Figure 5a) and $\bar{\alpha}$ (Figure 5b). After the loading time, the stress starts to slowly decay until it reaches a convergent value.

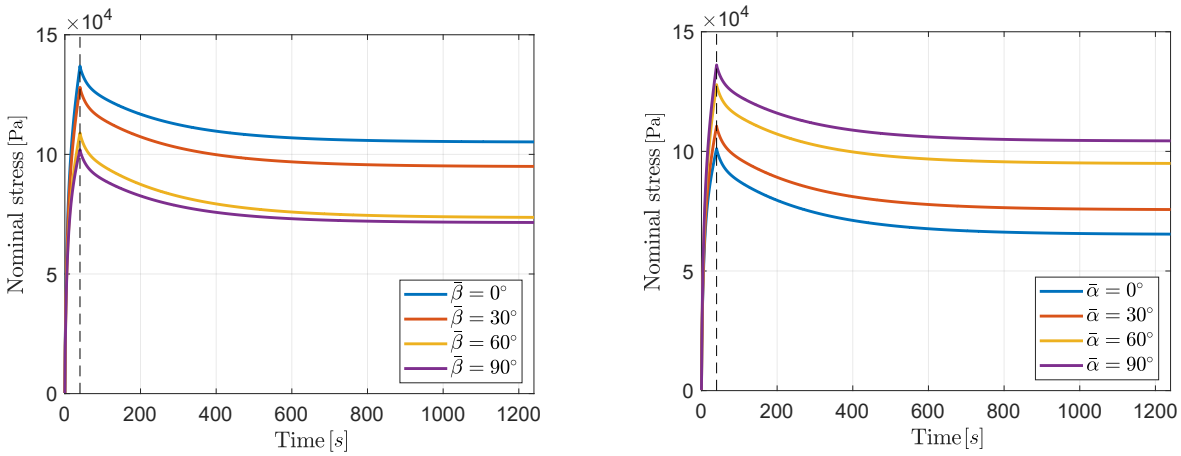

Figure 5: Numerical example 1. Mechanical case. Loading-relaxation analysis for maximum stretch $\lambda_{max} = 3$, strain rate $\dot{E}_{11} = 0.1s^{-1}$, and orientation of the laminated composite given by angles: (a) $\bar{\alpha} = 0°$ and $\bar{\beta}$ let to vary. (b) $\bar{\beta} = 75°$ and $\bar{\alpha}$ let to vary. The vertical dashed line indicates the time in which the loading is finished and the relaxation period starts.

In the following, the rank-one DE laminated film material is subjected to a homogeneous state of deformation and electric field (see Figure 6). Two electrodes are placed at opposite faces of the film and an externally controlled Lagrangian electric field $\boldsymbol{E_0}$ is applied across and orientated along the OX_3 axis, whilst maintaining stress free conditions, in turn, generating a state of uniform deformation and electric displacement across the film. In the absence of any further loads and electric charges, the homogeneous solution to this problem corresponds to the stationary points $\{\boldsymbol{F}^*, \boldsymbol{D}_0^*\}$ of the Helmholtz's free energy functional defined as

$$\Pi(\boldsymbol{F}^*, \boldsymbol{D}_0^*, \boldsymbol{E}_0) = \inf_{\boldsymbol{F}} \inf_{\boldsymbol{D}_0} \{e(\boldsymbol{F}, \boldsymbol{D}_0) - \boldsymbol{E}_0 \cdot \boldsymbol{D}_0\}, \tag{119}$$

where $\boldsymbol{E}_0$ is the externally controlled electric field. Thus, the stationary conditions of above functional arise as

$$\boldsymbol{\mathcal{R}_F}(\boldsymbol{F}, \boldsymbol{D}_0) = \partial_{\boldsymbol{F}} e = \boldsymbol{0}; \qquad \boldsymbol{\mathcal{R}_{D_0}}(\boldsymbol{F}, \boldsymbol{D}_0) = \partial_{\boldsymbol{D}_0} e - \boldsymbol{E}_0 = \boldsymbol{0}. \tag{120}$$

The above nonlinear stationary conditions (120) are solved in terms of unknowns $\boldsymbol{F}^*$ and $\boldsymbol{D}_0^*$ dependent upon the externally controlled electric field $\boldsymbol{E}_0$. Specifically, $\boldsymbol{F}$ and $\boldsymbol{E}_0$ are formulated as

$$\boldsymbol{F} = \begin{bmatrix} F_{11} & 0 & F_{13} \\ 0 & F_{22} & F_{23} \\ 0 & 0 & F_{33} \end{bmatrix}; \qquad \boldsymbol{E}_0 = \begin{bmatrix} 0 \\ 0 \\ E_0 \end{bmatrix}, \tag{121}$$

where F_{11} and F_{22} represent in-plane stretching; F_{13} and F_{23}, possible shearing effects; and F_{33}, the out-of-plane stretching. As in [58], although adding the time-dependent viscoelastic effects, the nonlinear stationary conditions (120) are solved by an iterative Newton-Raphson method.

First, the electric field is applied at an electric field rate of $\dot{E}_0 = 2 \cdot 10^4 V m^{-1} s^{-1}$ until it reaches the maximum value of $E_0 = 10^7 V m^{-1}$. Then, this electric field is decreased at the same rate. In Figure 7, it is observed how the angle of lamination affects the hysteresis effect. On the one hand, for an angle $\bar{\alpha} = 0°$ fixed, an increase in the angle of orientation $\bar{\beta}$ tends to translate into a larger stretch, specially for large values of $\bar{\beta}$. On the other hand, the effect of the variation of the angle $\bar{\alpha}$ is much less significative, being slightly larger the deformation in the case of large values of it.

Next, a loading-relaxation experiment is performed. The electric field is applied at an electric field rate of $\dot{E} = 2 \cdot 10^5 V m^{-1} s^{-1}$, until it reaches the maximum value $E_0 = 10^7 V m^{-1}$ in 50 seconds. Then, that value of eletric field is kept fixed for 2.7 hours (10,000 seconds), until the deformation reaches a stationary point. In Figure 8, the effect of the angle of lamination is observed.

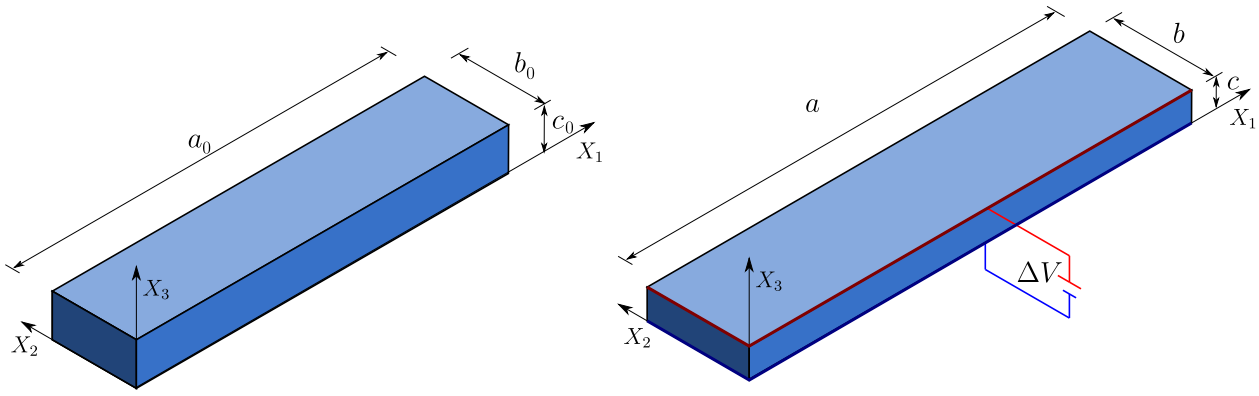

Figure 6: Numerical example 1: Second configuration. Experimental set-up. The application of a uniform electric field along the OX_3 direction causes a stretch of the DE laminated composite along OX_1 direction.

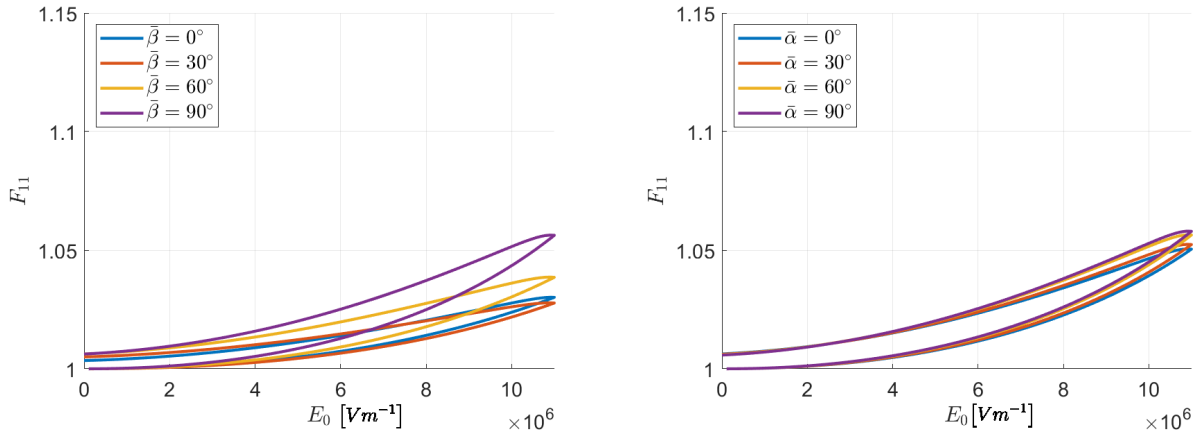

Figure 7: Numerical example 1. Electromechanical case. Loading-unloading test for voltage $E_0 = 10^7 Vm^{-1}$ applied at a rate $\dot{E} = 2 \cdot 10^4 Vm^{-1}s^{-1}$ in 500 seconds in a DE laminated composite material with an orientation given by angles: (a) $\bar{\alpha} = 0°$ and $\bar{\beta}$ left to vary. (b) $\bar{\beta} = 75°$ and $\bar{\alpha}$ left to vary.

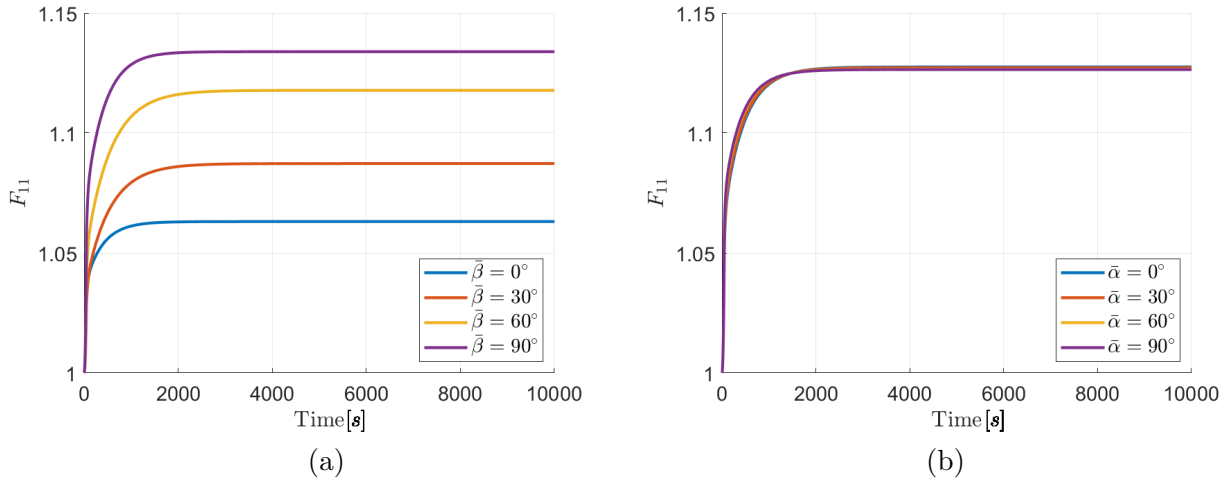

Figure 8: Numerical example 1. Electromechanical case. Loading-relaxation test for voltage $E_0 = 10^7 Vm^{-1}$ applied at a rate $\dot{E} = 2 \cdot 10^5 Vm^{-1}s^{-1}$ in 50 seconds in a material with angles of lamination: (a) $\bar{\alpha} = 0°$ and $\bar{\beta}$ left to vary. (b) $\bar{\beta} = 75°$ and $\bar{\alpha}$ left to vary.

6.2. Numerical example 2: complex deformation of a rectangular multi-layered DE film with viscoelastic effects

We consider a rectangular DE rank-one laminate film of dimensions 0.1 m × 0.03 m × 0.001 m, fully clamped at face $X_1 = 0$ and free everywhere else, as depicted in Figure 9. The geometrical and simulation parameters for this example are collected in Table 4. The domain is discretised using a $40 \times 16 \times 4$ hexahedral structured mesh, with $Q2$ finite elements used to interpolate both displacement and electric potential, being 96, 228 the total number of degrees of freedom of the problem. The solver coupling strategy is monolithic, with a tolerance for the Newton-Raphson method of 10^{-6} in Euclidean norm. Two electrodes are placed at the bottom and mid surfaces of the specimen and a voltage is applied across, which is increased linearly along the time until it reaches a voltage difference of $\Delta V = 4 \times 10^3$ V.

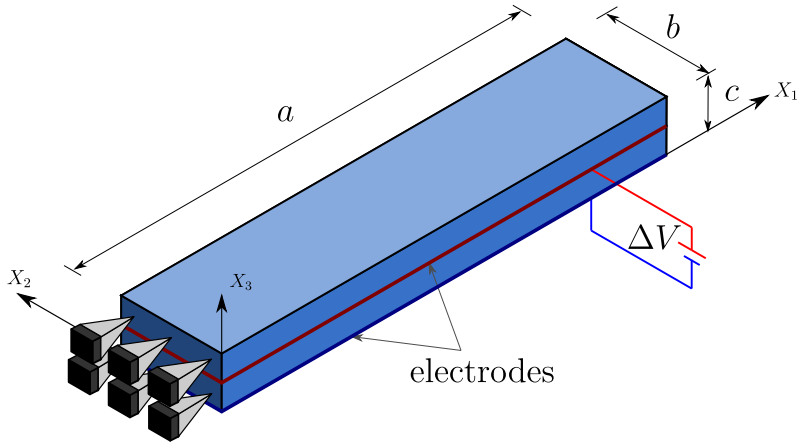

Figure 9: Numerical example 3. Geometry and boundary conditions.

Geometrical parameters	a	0.1	m	Simulation parameters	N_x	40
	b	0.03	m		N_y	16
	c	0.001	m		N_z	4
Voltage applied	ΔV	4	kV	Newton tolerance		10^{-6}

Table 4: Numerical example 2. Geometrical and simulation parameters.

The materials are the ones described at the beginning of Section 6, whose electromechanical and viscoelastic properties are collected in Tables 2 and 3, respectively.

6.2.1. Effect of the laminate orientation

In this example we aim to:

- Capture the various deformation modes that a rank-one DE laminated composite, in the form of a rectangular film, can undergo in response to electric stimuli, with the consideration of viscoelasticity in the material.
- Compare the response of the composite for different orientations of the laminate and provide some simple strain metrics to distinguish actuation deformation modes.

Figure 10 displays the evolution of the deformation along time and for various laminate orientations defined by angles $\{\bar{\alpha}, \bar{\beta}\}$. In all the sub-Figures, the final deformation of the hyperelastic case (disregarding viscoelastic effects on the materials) is shown shaded along with the evolution of the viscoelastic material. Notice that the voltage gradient $\Delta V = 4$ kV has been applied according to a linear ramp spanning 100 seconds. The following important conclusions can be extracted from these figures:

- For $\bar{\beta} = 0°$, Figure 10a displays a clear evolution of the viscous material to a bending type deformation mode denoted as **mode 1**. The final configuration adopted by the viscous material coincides perfectly at $t \to \infty$ with that of the hyperelastic material, hence, the overlapping between the two.

- For $\bar{\beta} = 90°$, Figure 10d displays a clear evolution of the viscous material to a completely different type of bending deformation with a pronounced bending around the longitudinal axis and denoted as **mode 2**. The final configuration adopted by the viscous material coincides perfectly at $t \to \infty$ with that of the hyperelastic material, hence, the overlapping between the two.

- For $\bar{\beta} = 20°$, Figure 10b displays an evolution of the deformed configuration of the viscous material which initially, resembles that of **mode 2**. However, as time evolves, a switch into a **mode 1** type deformation is obtained, coinciding perfectly at $t \to \infty$ with that of the hyperelastic material, hence, the overlapping between the two.

- For $\bar{\beta} = 40°$, Figure 10c shows a situation which is far from being intuitively anticipated. The viscoelastic material starts deforming according to **mode 2**. However, unlike the case with $\bar{\beta} = 20°$, the expected switch into **mode 1** is never obtained irrespectively of the time t. Therefore, for this specific loading scenario (linear ramp over a time of 50 seconds), the expected coincidence between the deformed configurations for both viscoelastic and hyperelastic materials is never achieved. As it will be seen in next section, using a different loading scenario could provide the hyperelastic solution if it includes enough time for the material to relax during the loading.

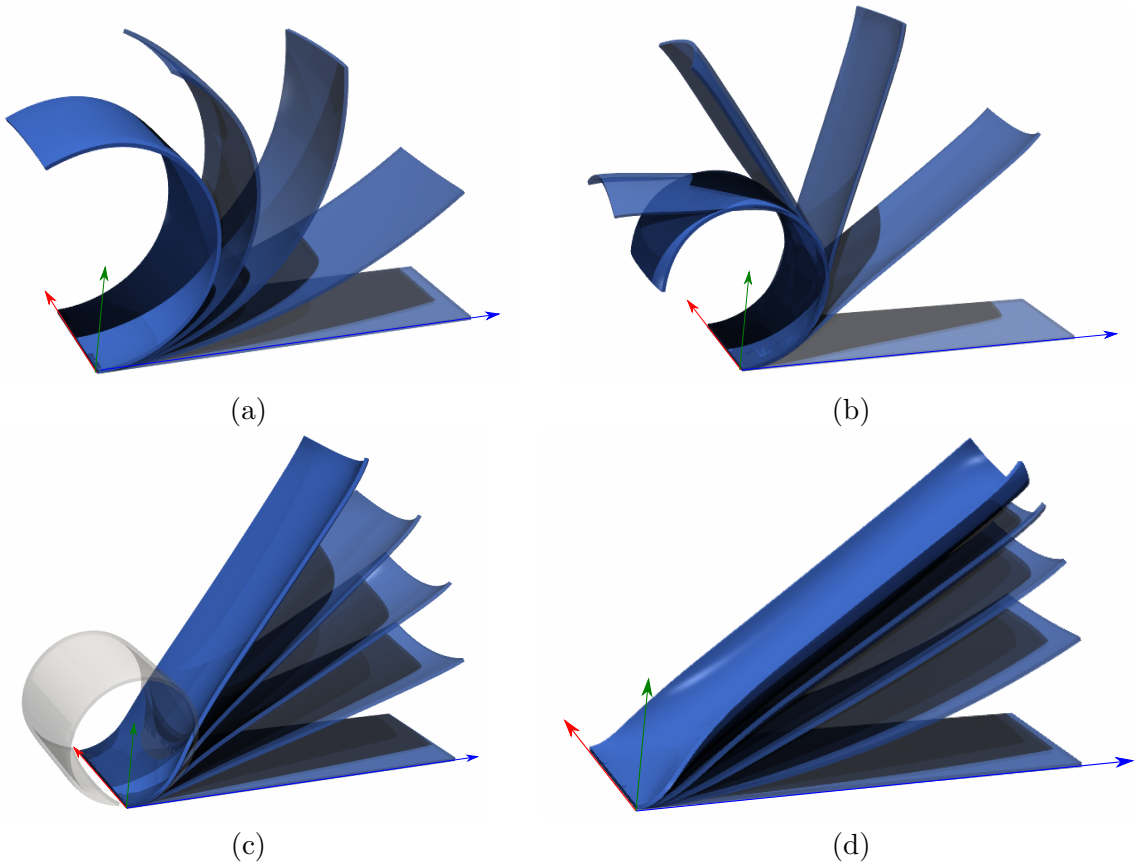

Figure 10: Numerical example 3. Deformation evolution for different orientation of the laminates given by $\bar{\alpha} = 0°$ and $\bar{\beta}$ left to vary: (a) $\bar{\beta} = 0°$ (**mode 1** for both hyperelastic and viscoelastic behaviours at $t = \infty$.), (b) $\bar{\beta} = 20°$ (**mode 1** for both hyperelastic and viscoelastic behaviours at $t = \infty$.), (c) $\bar{\beta} = 40°$ (**mode 1** for hyperelastic behaviour and **mode 2** for viscoelastic behaviour at $t = \infty$.), (d) $\bar{\beta} = 90°$ (**mode 2** for both hyperelastic and viscoelastic behaviours at $t = \infty$.). A ramp of maximum 4 kV has been applied over a time of $t = 100$ seconds.

In order to provide a simple metric for comparison of the two aforementioned deformation modes, namely, the normalised integral value of the Green-Lagrange strain tensor $\boldsymbol{\varepsilon}$ is defined as

$$\boldsymbol{\varepsilon} = \frac{1}{|V|}\int_V \boldsymbol{E} dV; \qquad \boldsymbol{E} = \frac{1}{2}\left(\boldsymbol{F}^T\boldsymbol{F} - \boldsymbol{I}\right). \tag{122}$$

Figure 11a displays the evolution of components ε_{11} and ε_{22} of $\boldsymbol{\varepsilon}$ along time for various laminate orientations defined by angle $\bar{\alpha} = 0°$ and $\bar{\beta}$ left to vary. Crucially, for angles $\bar{\beta} = 20°, 30°, 33°$ metric ε_{11} takes a considerably large period of time during which a progressive switch into a larger value of the metric ε_{11} is obtained. The opposite occurs for metric ε_{22}, as an extremely prolonged over time decay is observed before a stationary solution is obtained. Specifically, for $\bar{\beta} = 33°$, around 8×10^4 seconds are needed in order to obtain a stationary solution for both metrics ε_{11} and ε_{22}. On the contrary, a stationary solution is attained much faster for values of $\bar{\beta}$ which are far below and above a value of $\bar{\beta} = 33.2°$. This result is also appreciated in Figure 11b, displaying the following quantity

$$\bar{\lambda} = \frac{\int_{\mathcal{B}_0} \lambda_1 \, dV}{|\mathcal{B}_0|}; \qquad \lambda_1 = \max(\mathrm{eig}(\boldsymbol{A}_1)), \tag{123}$$

where λ_1 [13] represents the maximum eigenvalue of the internal variable $\boldsymbol{A}_1$. Clearly, for angles $\bar{\beta} = 20°, 30°, 33°$, λ_1 takes a considerably large period of time before a stationary value is obtained.

A more insightful interpretation of these results can be obtained from Figure 11c-d. In these figures, for small values of $\bar{\beta}$ (below approximately $\bar{\beta} = 13.8°$), the response of the viscoelastic material is extremely fast. This can be deduced from the fact that irrespectively of the time considered $t = \{10^3, 5\times10^3, 10^4, 10^5\}$, the value of both metrics ε_{11} and ε_{22} barely changes, hence displaying a stationary condition before $t = 10^3$ seconds. Moreover, the actuation mode displayed by all the configurations in this region ($\bar{\beta} \leq 13.8°$) corresponds with that denoted as **mode 1**.

However, in the approximate interval $13.8° \leq \bar{\beta} \leq 33.2°$, the curve for both ε_{11} and ε_{22} suddenly bifurcates, indicating that the initial trend (for small values of time) of the material is to develop an electrically induced deformation compatible with that of **mode 2**. However, as time evolves, for a fixed value of $\bar{\beta}$, the deformed configuration of the material develops a radical morphological change evolving into a shape compatible with that of **mode 1**. As it can be seen, the mode switching behaviour over time described delays the fast response of the material initially observed in the region $\bar{\beta} \leq 13.8°$, and around 10^5 seconds can be needed before a finally converged deformation compatible with **mode 1** is obtained. Crucially, this mode switching behaviour over time is restricted to this region $13.8° \leq \bar{\beta} \leq 33°$, and does not occur beyond the critical value of $\bar{\beta} = 33°$. Indeed, beyond this region ($\bar{\beta} > 33°$), the material develops a deformed configuration which is compatible with actuation **mode 2** irrespectively of the time considered, yielding again a fast response to the electrical excitation. This is in clear contrast with the response yielded by the hyperelastic material, for which a deformation compatible with that of **mode 2** is obtained only in the case $\bar{\beta} \geq 46.7°$. Therefore, the critical value $\bar{\beta}_{cr}$ for which a finally converged solution compatible with **mode 2** is obtained differs between the viscoelastic and hyperelastic cases, yielding $\bar{\beta}^v_{cr} = 33°$ and $\bar{\beta}^h_{cr} = 46.7°$, respectively. Remarkably, this indicates, contrary to intuition, that the stationary solution reached by the viscoelastic material (i.e., at $t = \infty$) will differ from that obtained by the hyperelastic material when the angle $\bar{\beta}$ lies within the interval $33° < \bar{\beta} \leq 46.7°$.

Figure 12 shreds some information corroborating the previous findings. Specifically, for time steps $t = \{50, 10^3, 5\times10^3, 10^4, 10^5, \infty\}$, the deformed configuration for various values of the angle $\bar{\beta}$ is presented, confirming qualitatively the numerical conclusions inferred from Figure 11.

[13] Note that providing a physical meaning for λ_1 quantity is not necessary in this context, since the aim pursued is to monitor a magnitude related to the internal variables, in order to corroborate if a stationary regime is reached. Other options, such as the L^2-norm of the internal variable $\boldsymbol{A}_1$, could be equally used with the exact purpose.

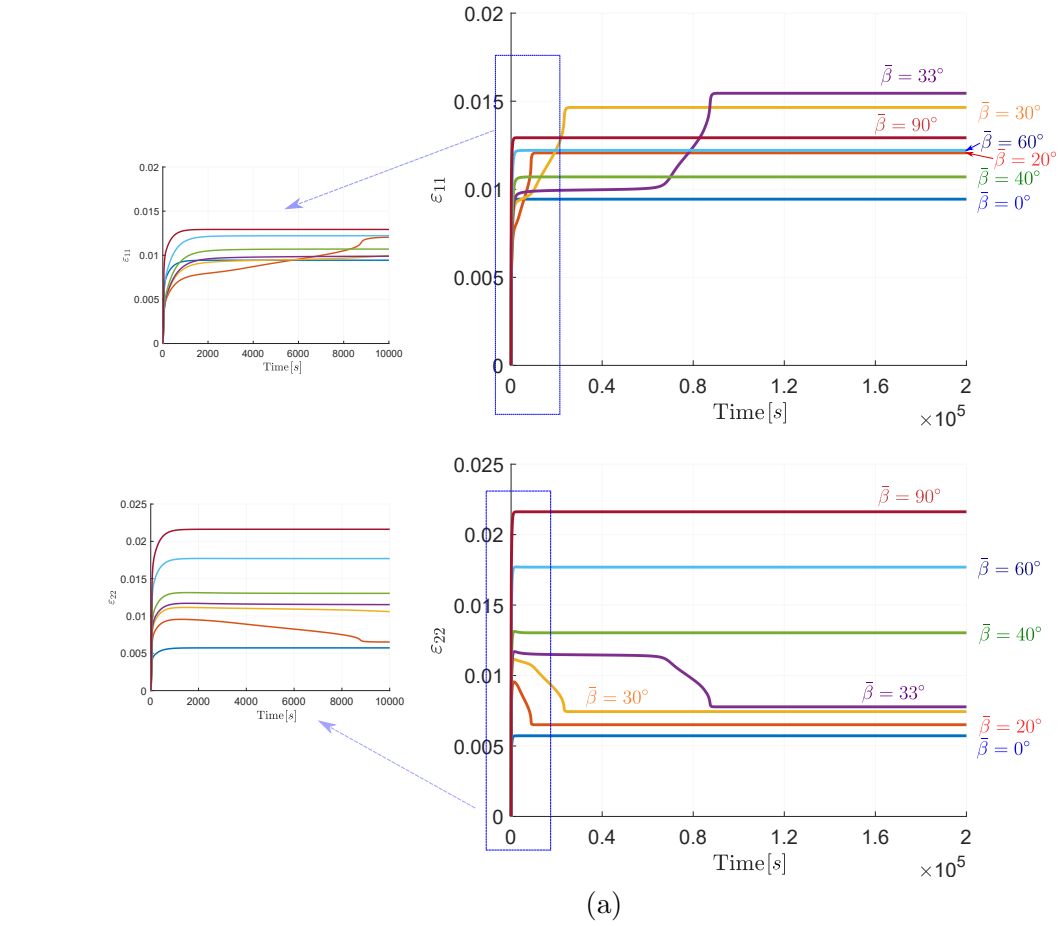

(a)

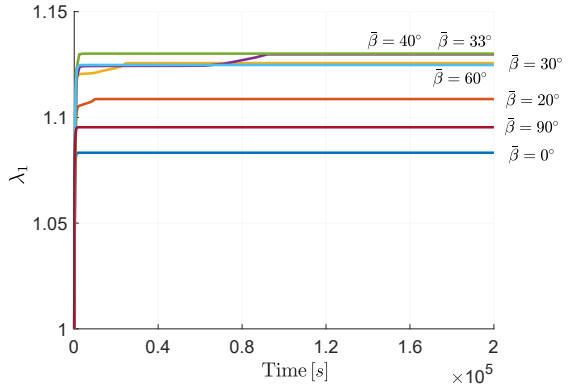

(b)

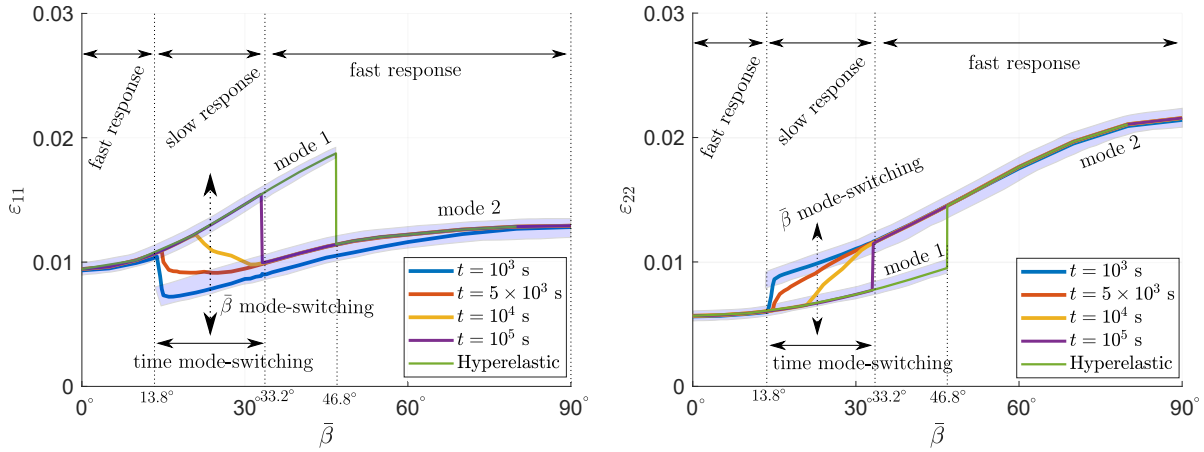

(c) (d)

Figure 11: Numerical example 2. Evolution of: (a) components ε_{11} and ε_{22} of the normalised integral value of the Green-Lagrange strain tensor $\boldsymbol{\varepsilon}$ (122), (b) quantity $\bar{\lambda}$ (123) representing the spatial integral of the maximum eigenvalue of the internal variable $\boldsymbol{A}_1$, for $\bar{\alpha} = 0°$ and $\bar{\beta}$ left to vary. Components (c) ε_{11} and (d) ε_{22} against angle $\bar{\beta}$ (for $\bar{\alpha} = 0°$ fixed) at different time stamps and for the hyperelastic case (without considering viscous effects).

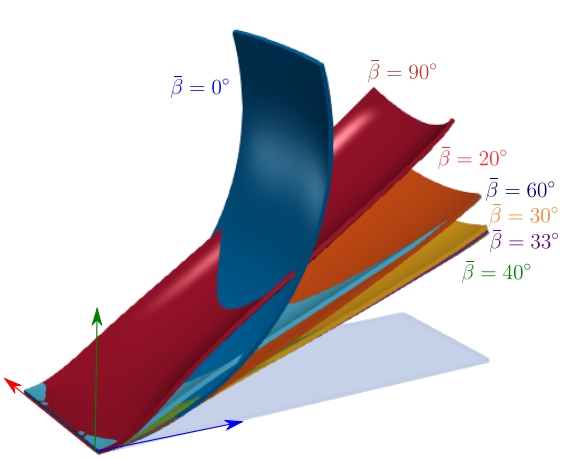

Time $= 50$ s

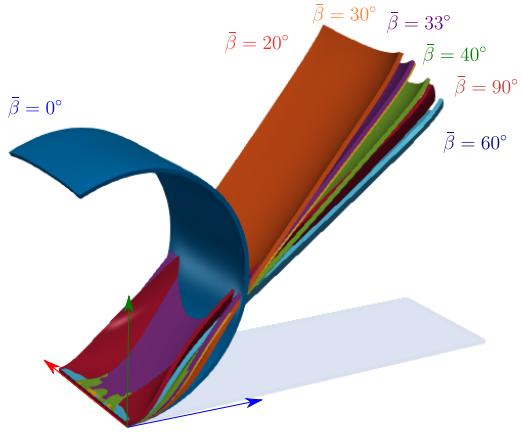

Time $= 10^3$ s

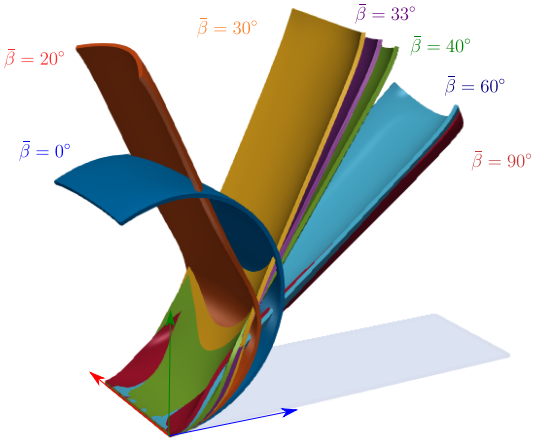

Time $= 5 \times 10^3$ s

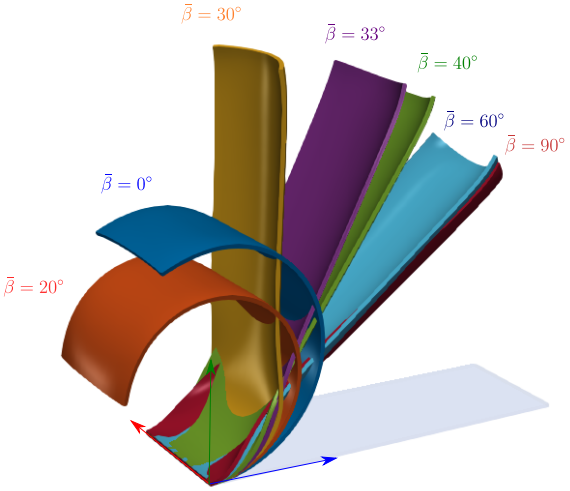

Time $= 10^4$ s

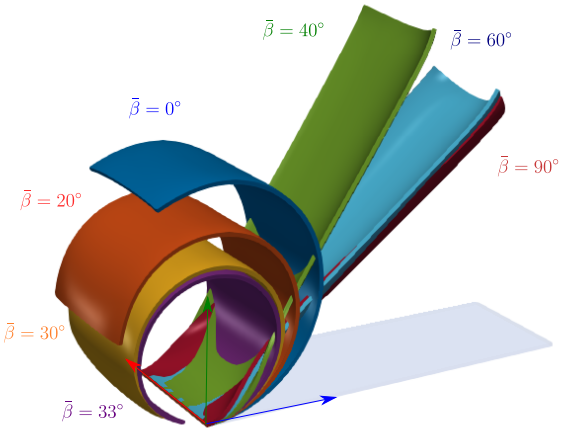

Time $= 10^5$ s

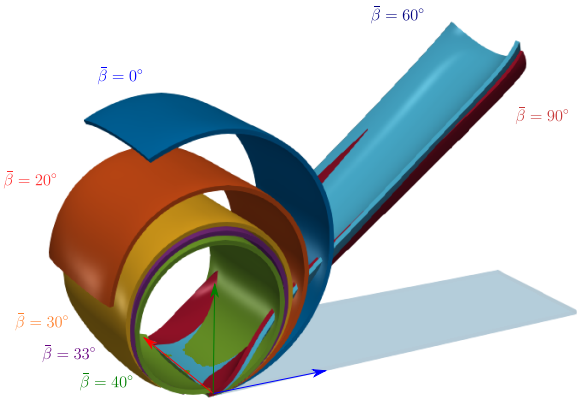

Time $\to \infty$

Figure 12: Numerical example 3. Deformation of the laminate at different times, for different values of orientation angle $\bar{\beta} = \{0°, 20°, 30°, 33°, 40°, 60°, 90°\}$, keeping $\bar{\alpha} = 0°$.

6.2.2. Effect of different time dependent electrical loading

Furthermore, we intend to shred more insightful information regarding the example analysed in Section 6.2.1. In this case, we will focus on different aspects with the aim of:

- Studying the response of the composite when subjected to different time dependent electrical loadings.
- Analysing the possible local loss of macroscopic ellipticity in order to ensure that spurious mesh dependent effects are not developed in the finite element analysis.

Alternatively to the loading condition in Section 6.2.1, where a voltage gradient $\Delta V = 4$ kV was applied according to a linear ramp over a time of 50 seconds, now we explore different loading scenarios and its potential impact on the deformation of the composite. Specifically, we use the different loading scenarios collected in Table 5 and graphically represented in Figure 13, which are characterised by a larger time of application of the final voltage during which a combination of short time periods of load increase with larger time periods of relaxation (load is kept at the same value) is used. We recall from the previous section that, see Figure 11, in terms of the orientation angle $\bar{\beta}$, we can classify the response of the material in three categories: fast response, for $0° \leq \bar{\beta} \leq 13.8°$, slow response, for $13.8° < \bar{\beta} < 46.7°$, and again fast response for $46.7° \leq \bar{\beta} \leq 90°$. In particular, our interest in this section focuses on the intermediate area of slow response, i.e., $13.8° < \bar{\beta} < 46.7°$. In turn, this area is divided into two sub-areas: a) angles $13.8° \leq \bar{\beta} \leq 33°$ for which the material initially seems to deform to **mode 2**, but when the time increases, there is a switch of mode to **mode 1**, to reach the hyperelastic solution; and b) angles $33° \leq \bar{\beta} \leq 46.7°$, for which the material goes to a different deformation **mode 2** and never reaches the hyperelastic solution. To study this two sub-regions, we take a particular value of each of them, in concrete, $\bar{\beta} = 20°$ and $\bar{\beta} = 34°$, keeping $\bar{\alpha} = 0°$ fixed.

The revealing results from this study can be found in Figures 14 and 15. For the first case, Figure 14, it is observed that, using multi-step loading scenarios A and B, a converged solution for both metrics ε_{11} and ε_{22} is obtained after around 3000 and 2000 seconds for both loading conditions, respectively. This is in clear contrast with the approximately 8000 seconds needed to reach a stationary solution for the single-step linear ramp considered in the previous study. Therefore, it seems that the consideration of slower multi-step loading conditions accelerate the response of the composite material with respect to a faster loading scenario, as that characterised by the linear ramp over 50 seconds considered in the previous section. The underlying reason is that, fast loading scenarios can potentially induce deformations in the initial time steps which are compatible with deformation **mode 2**, even when the stationary solution for the hyperelastic counterpart is still compatible with **mode 1**. Recovering from **mode 2** and switching to **mode 1** can take an extraordinary amount of time and can even be irreversible. The latter is confirmed in the case for $\bar{\beta} = 34$ (Figure 15). In this case, it is observed that a quite slow multi-step loading scenario is needed (scenario E), being scenarios C and D insufficient to reach the hyperelastic solution (**mode 2** deformation). Of course, A and B and single-step modes are very far away too.

Therefore, slow loading scenarios preventing the material from undergoing initial deformations compatible with **mode 2** (for the case $\bar{\beta} \leq 46.8$) can ultimately accelerate the response of the composite, as corroborated by Figure 14.

In order to conclude this experiment, a brief study on the variation of the orientation $\bar{\alpha}$ is also carried out. In Figure 17, the evolution of the deformation of the composite for two different laminate orientations is shown. Specifically, angle $\bar{\alpha}$ is responsible for the torsional electrically-induced shown in Figure 17. With regards to the loading scenario, the fast linear ramp of the previous section has been applied.

Taking advantage of this study with respect to the additional angular field $\bar{\alpha}$, we then analyse the possible loss of macroscale ellipticity and convexity of the homogenised response of the material. For the sake of simplicity, we present the results for a specific orientation of the laminate, namely $\bar{\alpha} = 15°$ and $\bar{\beta} = 90°$, and two states of deformation. To study loss of ellipticity, we compute the field distribution of the smallest of the minors of the acoustic tensor for any possible orientation ν, namely

$$\mathrm{I}_{\mathrm{ellip}} = \min_{\boldsymbol{\nu}} q, \tag{124}$$

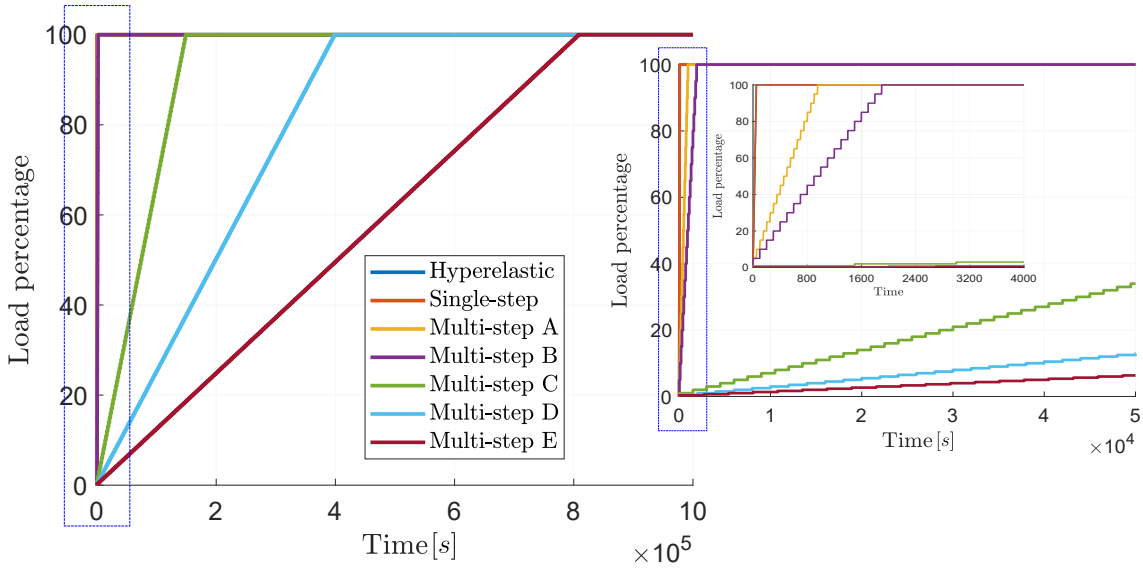

Figure 13: Numerical example 2. Different loading scenarios. The load percentage is represented along time for all the loading scenarios (see Table 5), making zoom in a particular time to observe how the load increases in a multi-step way.

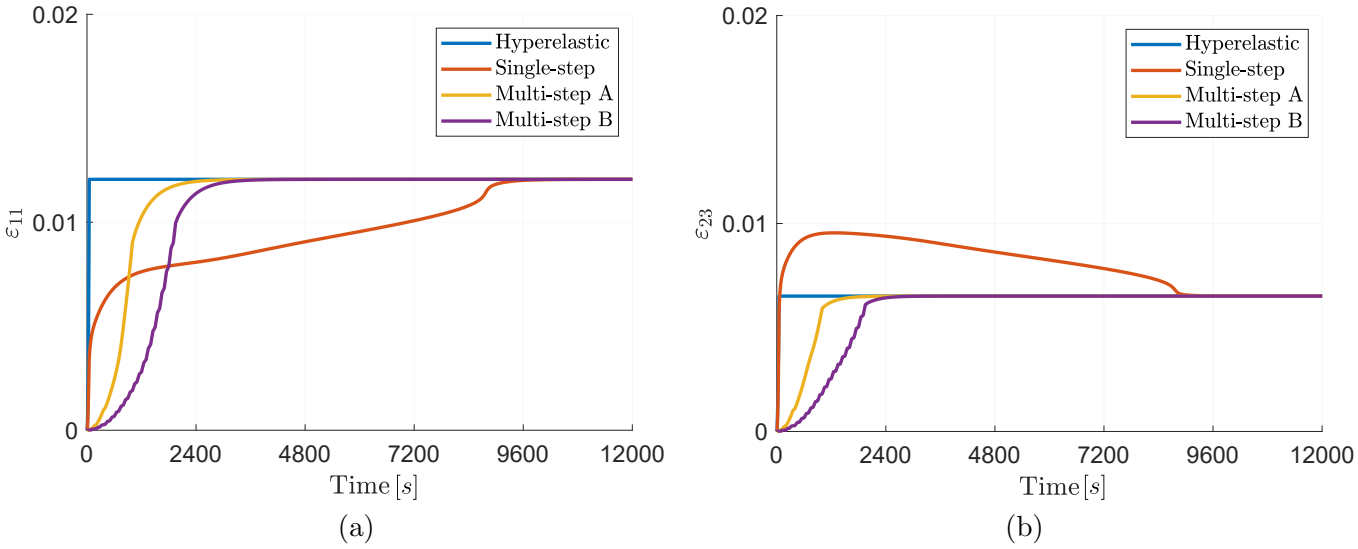

Figure 14: Numerical example 2. Comparation of the evolution of deformation quantities: (a) ε_{11}, (b) ε_{22}; for the cases of single-step and multistep loading. The orientation of the laminate is given by angles $\bar{\alpha} = 0°$, $\bar{\beta} = 20°$.

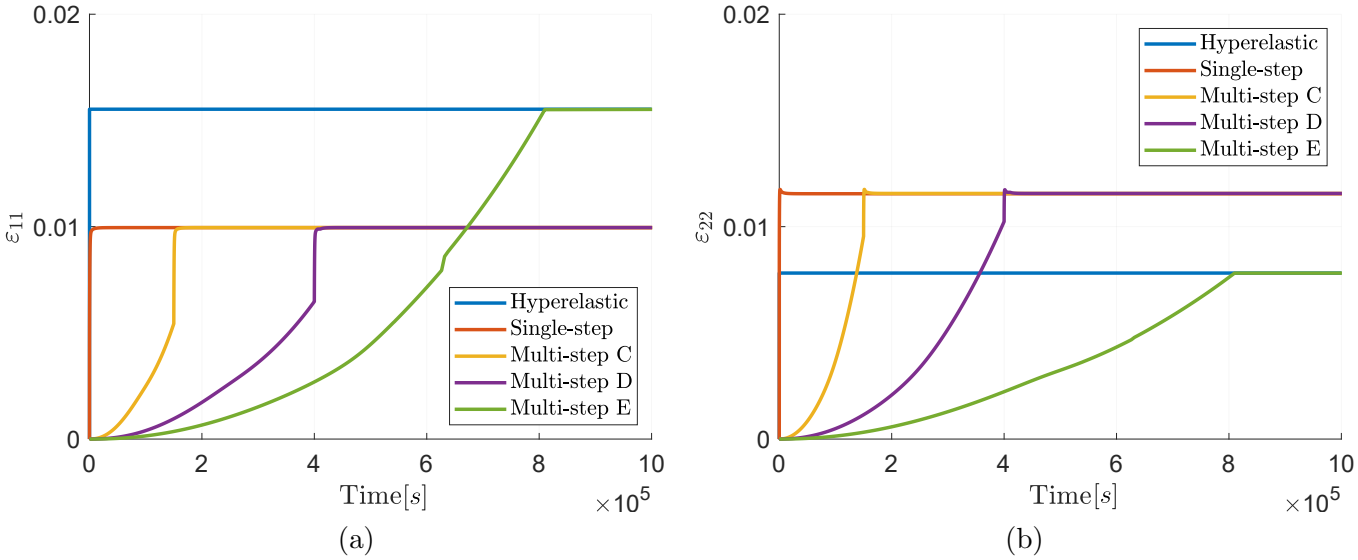

Figure 15: Numerical example 2. Comparation of the evolution of deformation quantities: (a) ε_{11}, (b) ε_{22}; for the cases of single-step and multistep loading. The orientation of the laminate is given by angles $\bar{\alpha} = 0°$, $\bar{\beta} = 34°$.

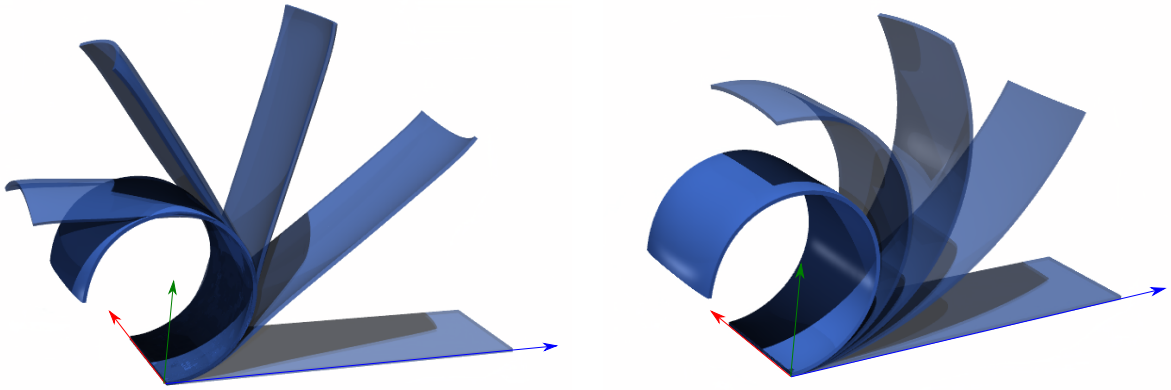

Figure 16: Numerical example 2. Evolution pattern to reach the hyperelastic deformation mode with loading given by: (a) single-step, (b) multi-step type B. The orientation of the laminate is given by $\bar{\alpha} = 0°$, $\bar{\beta} = 20°$.

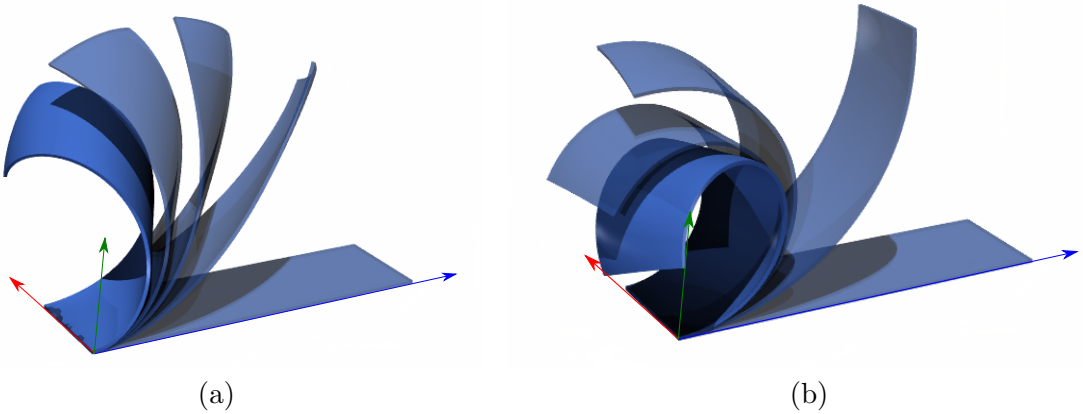

Figure 17: Numerical example 3. Deformation evolution for different orientations of the laminates given by $\bar{\beta} = 90°$ and $\bar{\alpha}$ left to vary: (a) $\bar{\alpha} = 15°$, (b) $\bar{\alpha} = 75°$.

Scenario	Number of steps	Time per step (s) Loading	Relaxation	Total time(s) (approx.)
Single-step	1	50	0	50
Multi-step A	20	1	9	200
Multi-step B	20	1	99	2000
Multi-step C	100	0.5	1500	1.5×10^5
Multi-step D	200	0.5	2000	4×10^5
Multi-step E	300	0.5	2700	8.1×10^5

Table 5: Numerical example 2. Different loading scenarios.

where $\boldsymbol{q}$ is defined as

$$\boldsymbol{q} = q\,\boldsymbol{\nu}; \qquad q = \min\left(\frac{Q_{11}}{\bar{\mu}}, \frac{Q_{11}Q_{22} - Q_{12}Q_{21}}{\bar{\mu}^2}, \frac{\det \boldsymbol{Q}}{\bar{\mu}^3}\right), \tag{125}$$

with $\bar{\mu} = c^a\mu^a + c^b\mu^b$. and the electro-mechanical acoustic tensor $\boldsymbol{Q}$ given by [67]

$$\boldsymbol{Q} = \boldsymbol{\mathcal{C}}_{\boldsymbol{\nu}\boldsymbol{\nu}} - \boldsymbol{\mathcal{Q}}_{\boldsymbol{\nu}}{}^T \boldsymbol{\theta}^{-1} \left(\boldsymbol{I} - \frac{(\boldsymbol{\nu} \otimes \boldsymbol{\theta}^{-1}\boldsymbol{\nu})}{\boldsymbol{\nu} \cdot \boldsymbol{\theta}^{-1}\boldsymbol{\nu}}\right) \boldsymbol{\mathcal{Q}}_{\boldsymbol{\nu}}, \tag{126}$$

and

$$(\boldsymbol{\mathcal{C}}_{\boldsymbol{\nu}\boldsymbol{\nu}})_{ij} = \mathcal{C}_{iIjJ}\nu_I\nu_J, \qquad (\boldsymbol{\mathcal{Q}}_{\boldsymbol{\nu}})_{Ij} = \mathcal{Q}_{IjJ}\nu_J. \tag{127}$$

The quantity $\mathrm{I}_{\mathrm{ellip}}$ in (124) is plotted in Figure 18. It is observed that no areas of macroscale loss of ellipticity arise, indicating that no spurious mesh dependency effects arise. Similar conclusions were observed for the rest of the simulations presented in this section and thus are not included. In addition, a metric is defined in order to measure the potential loss of convexity of the homogenised model, defined as the smallest eigenvalue of the Hessian operator of the homogenised internal energy, namely

$$\mathrm{I}_{\mathrm{conv}} = \frac{1}{\bar{\mu}} \min \mathrm{eig}([\mathbb{H}_e]), \tag{128}$$

with $\bar{\mu} = c^a\mu^a + c^b\mu^b$. This quantity is represented in Figure 19. In this case, some negative values are observed, indicating that local loss of convexity is potentially observed, yet with no impact in the loss of ellipticity.

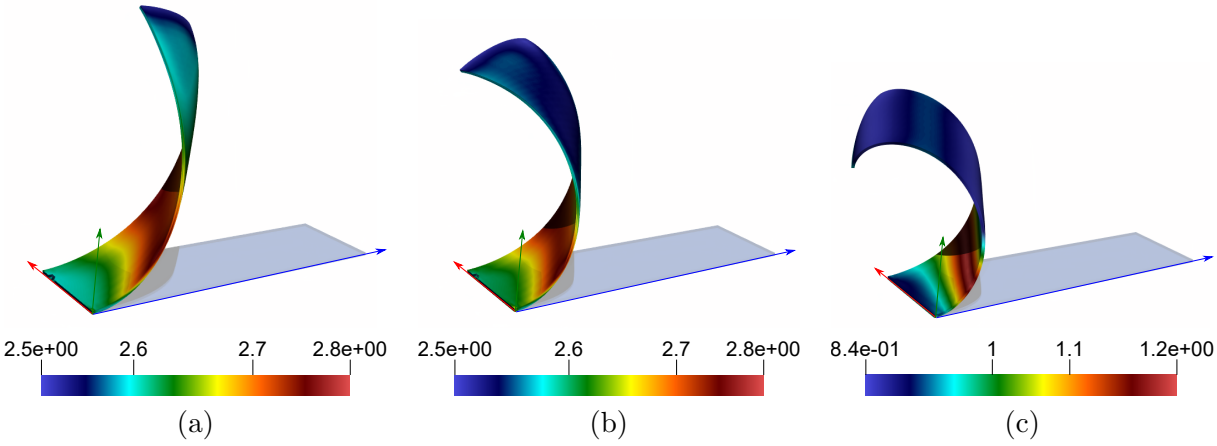

Figure 18: Numerical example 2. Contour plot of $\mathrm{I}_{\mathrm{ellip}}$ (124) for three time stamps: (a) $Time = 33s$, (b) $Time = 47s$, (c) $Time = 61s$. The orientation of the laminate is given by $\bar{\alpha} = 15°$ and $\bar{\beta} = 90°$.

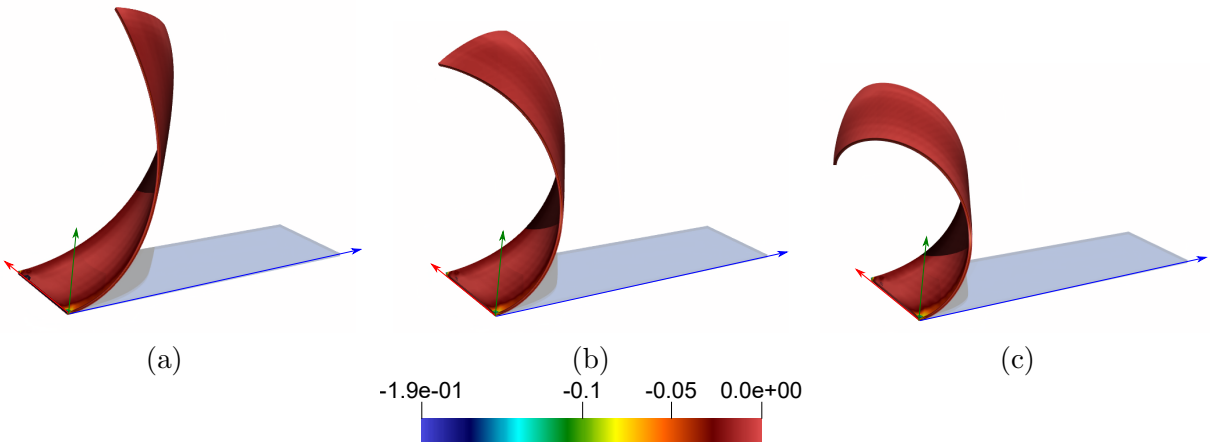

Figure 19: Numerical example 2. Contour plot of $\mathrm{I}_{\mathrm{conv}}$ (128) for three time stamps: (a) $Time = 33s$, (b) $Time = 47s$, (c) $Time = 61s$. The orientation of the laminate is given by $\bar{\alpha} = 15^\circ$ and $\bar{\beta} = 90^\circ$.

6.3. Numerical example 3: buckling on a multi-layered DE square membrane with viscoelastic effects

The objectives of this example are to:

- Detect the onset of instabilities on a rank-one DE laminated composite square membrane, with the consideration of viscoelastic properties of the materials.
- Observe the different patterns of buckling in terms of the microscale configuration.
- Observe the evolution of the deformation in terms of the loading rate, due to the viscoelastic effects.
- Analyse possible local loss of ellipticity and convexity and demonstrate the superior numerical stability properties of the viscoelastic case with respect to the hyperelastic case.

The geometry for this numerical example is given by a square membrane of side $l = 0.06$ m and thickness $h = 0.001$ m, clamped along all its side faces, as represented in Figure 20. The membrane is subjected to a prescribed electric surface charge on its base, while it is grounded to zero potential on its topside. Geometrical and finite element simulation parameters are presented in Table 6. $Q2$ finite elements are used to interpolate both displacement and electric potential, being 104188 the total number of degrees of freedom, and the surface charge is applied incrementally along time.

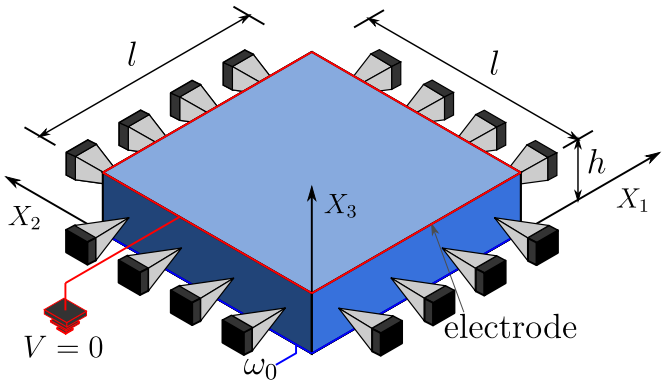

Figure 20: Numerical example 4. Geometry and boundary conditions.

Geometrical parameters	l	0.06	m	Simulation parameters	N_x	60
	h	0.001	m		N_y	60
					N_z	2
Electric charge	ω_0	0.004	C/m^2	Newton tolerance		10^{-6}

Table 6: Numerical example 4. Geometrical and simulation parameters.

The constituents of the laminated composite material are those described at the beginning of Section 6, whose properties are collected in Tables 2 and 3. In the analysis performed in [58], the viscoelastic properties of the material were not considered. In this work, however, we explore their effect in the change of deformation pattern as well as on the numerical stability of the simulations.

Since the square membrane is subjected to an increasing electric potential, it starts to slowly bend upwards until it reaches a point where it develops some initial buckling, marking a drastic change in stiffness. In Figure 21, the equilibrium paths are displayed for different orientations of the laminate, keeping the angle $\bar{\alpha} = 0°$ fixed and varying the angle $\bar{\beta}$ from 0° to 90°. The vertical displacement along the X_3 axis (u_3) is plotted for two sample points on the membrane: test point 1, which corresponds to the centre of the square, and test point 2, which is one close to the boundary. In Figure 21(a), the onset of a first order buckling is captured at approximately a value of the averaged scaled electric potential $\bar{E}_0 < 10^{-5}$, with

$$\bar{E}_0 = \frac{\bar{\varphi}}{\sqrt{\bar{\mu}/\bar{\varepsilon}}}; \qquad \bar{\varphi} = \frac{\int_{\partial\mathcal{B}_0^\star} \varphi \, dA}{\int_{\partial\mathcal{B}_0^\star} dA}; \qquad \bar{\mu} = c^a(\mu_1^a + \mu_2^a) + c^b(\mu_1^b + \mu_2^b); \qquad \bar{\varepsilon} = \varepsilon_0 \left(c^a \varepsilon^a + c^b \varepsilon^b\right), \quad (129)$$

where $\partial\mathcal{B}_0^\star$ represents the boundary located at $\min(X_3)$, namely, where the surface charge is applied. In Figure 21(b), a second-order buckling starting around $\bar{E}_0 = 5 \times 10^{-4}$ is observed. In this case, it is demonstrated that the orientation of the laminate does affect significantly the buckling pattern, being the deformation for angles $0° < \bar{\beta} < 30°$ larger than for higher values of the angle $\bar{\beta}$, after a third-order buckling is developed. The results are similar to those of the hyperelastic case analysed in [58], with small changes in the slope of the curves and some oscillating behaviour for some angles at the very last part (see for instance case $\bar{\beta} = 15$).

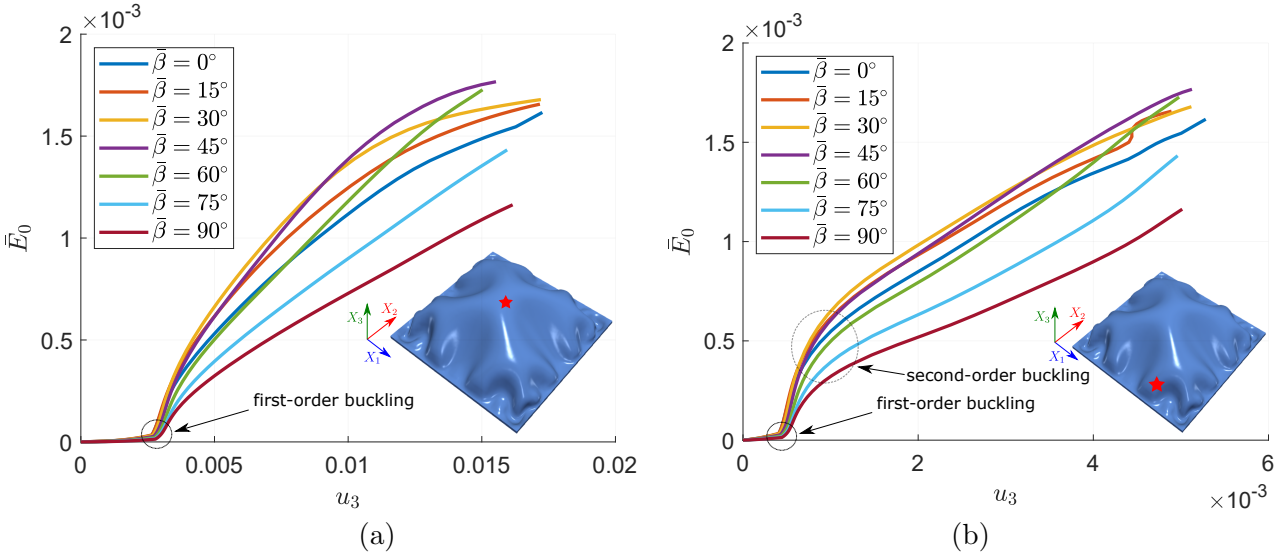

Figure 21: Numerical example 3. Vertical displacement along the X_3 axis of two test points: (a) the centre of the square; (b) a point near the border. The orientation of the laminate is given by $\bar{\alpha} = 0°$ and $\bar{\beta}$ left to vary.

A similar analysis is performed for the variation of the angle $\bar{\alpha}$, whilst keeping the angle $\bar{\beta} = 75°$ fixed. In figures 22, the electric field is represented against the vertical displacement for the same two test points on the square membrane. In this case, it is observed a similar behaviour in terms of the center of the square, but a very different one of the point near the border. For instance, in the case $\bar{\alpha} = 90°, \bar{\beta} = 75°$, the test point 2 starts moving upwards, until approximately $E_0 = 1.2 \times 10^{-3}$, and then moves downwards when the electric field gets higher.

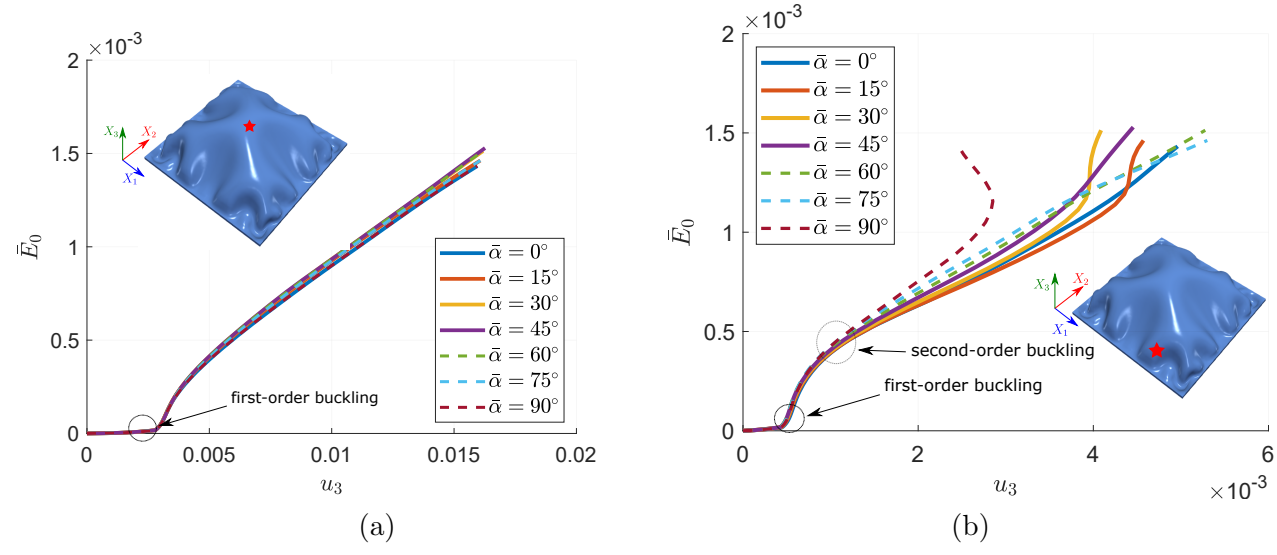

Figure 22: Numerical example 3. Vertical displacement along the X_3 axis of two test points: (a) the centre of the square; (b) a point near the border. The orientation of the laminate is given by $\bar{\beta} = 75°$ and $\bar{\alpha}$ left to vary.

In Figure 23, some snapshots of the deformation evolution of the membrane are represented, for the composite with laminate orientation given by $\bar{\alpha} = 0°$, $\bar{\beta} = 60°$. It is observed how the membrane buckles initially around its centre, and then initially small wrinkles get much more pronounced as $\bar{E}_0$ increases.

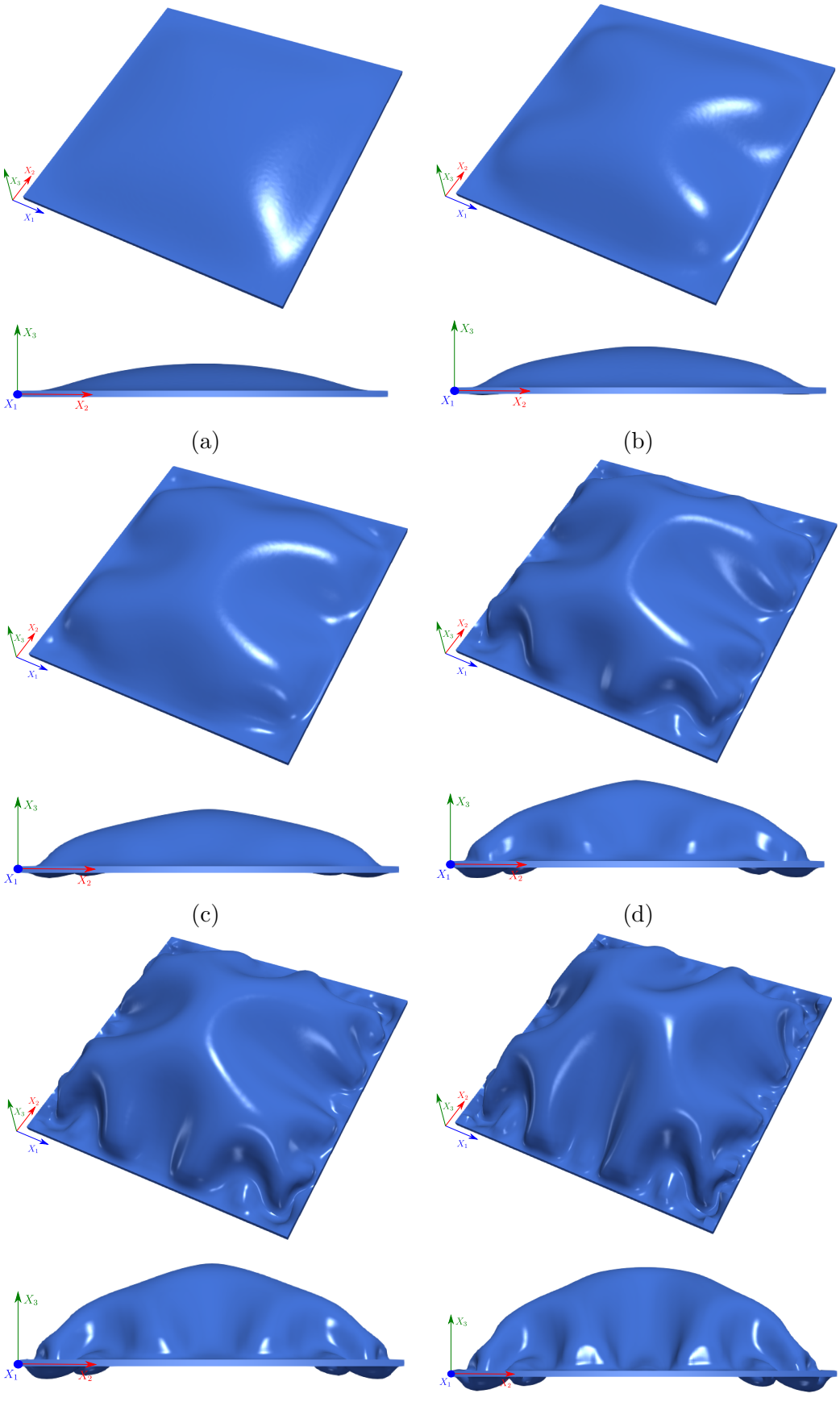

Figure 23: Numerical example 3. Evolution of deformation with the load factor for the case $\bar{\alpha} = 0°, \bar{\beta} = 60°$. From left to right and from top to bottom, the snapshots correspond to the following time stamps: (a) $t = 30s$, (b) $t = 40s$, (c) $t = 45s$, (d) $t = 50s$, (e) $t = 80s$, (f) $t = 200s$.

In Figures 24 and 25, the final aspect of the square membrane after deformation is shown for different laminate orientations of the composite. Figure 24 analyses the effect of the change in orientation angle $\bar{\beta}$ whilst keeping $\bar{\alpha} = 0°$, whereas Figure 25 focuses on the variation of $\bar{\alpha}$ whilst keeping $\bar{\beta} = 60°$. It can be observed that some configurations have a symmetry pattern, as for instance the case $\bar{\alpha} = 0°, \bar{\beta} = 0°$ which is symmetric with respect to both axes X_2 and X_3. When the angle of orientation of the composite is changed, the symmetry over some axes disappears, and a larger density of instabilities seems to happen.

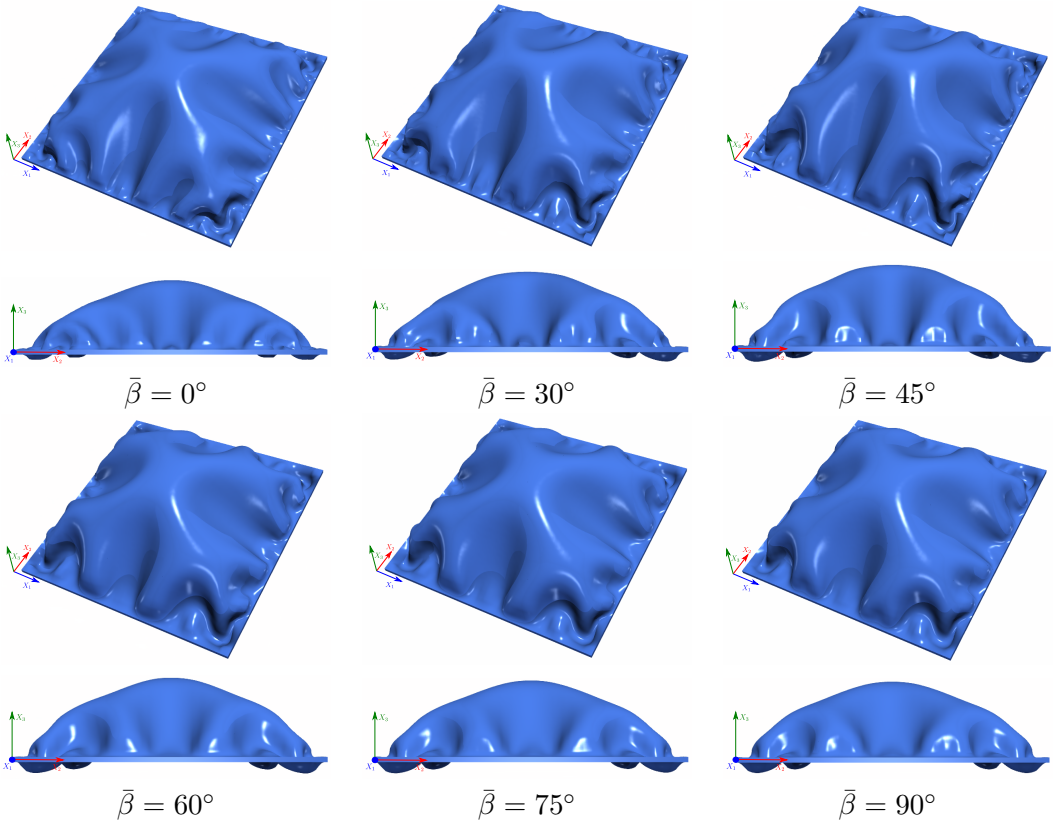

Figure 24: Numerical example 4. Different patterns of buckling for various values of $\bar{\beta} = [0°, 30°, 45°, 60°, 75°, 90°]$ and $\bar{\alpha} = 0°$. The time is $t = 290s$.

6.3.1. Stabilisation effect of the visco-elastic contribution

It is important to remark that the consideration of viscoelasticity in the material contributes to stabilise the deformation under the electric charge. In Figure 26, both hyperelastic and viscoelastic responses are compared. Clearly, the viscoelastic material is able to reach a higher value of the applied electric charge ω_0 before numerical instabilities develop. Specifically, the hyperelastic case is only able to reach a value of $\omega_0 = 2 \times 10^{-3}$ C/m, after which the simulation becomes unstable. However, the viscoelastic case we were able to carry out the numerical simulation even for a value of $\omega_0 = 4 \times 10^{-3}$ without any numerical instability, being able to reach a finally stationary solution (horizontal line in Figure 26).

These findings are corroborated by Figure 27, where the deformed configuration of the hyperelastic material at the onset of numerical instability (i.e. $\omega_0 = 2 \times 10^{-3}$ C/m), and that of the viscoelastic material for a value of $\omega_0 = 4 \times 10^{-3}$ are shown. Clearly, that wrinkles developed over the viscoelastic material are much more pronounced due to the ability to perform the simulations at considerably larger values of the externally applied surface charge ω_0.

The superior numerical stability of the viscoelastic material confirms the analytical findings obtained in Section 3.5, and specifically, in equation (46). In this equation we proved that the mathematical expression for the ellipticity condition (i.e. $D\mathcal{D}_{int,E}[\boldsymbol{u} \otimes \boldsymbol{V}, \boldsymbol{V}_{\perp}]$) in the visco-elastic case, adds an additional unconditionally positive term with respect to the exclusively hyperelastic response. The effect of this positive viscoelastic regularisation contribution is translated into the numerics into the superior numerical stability observed.

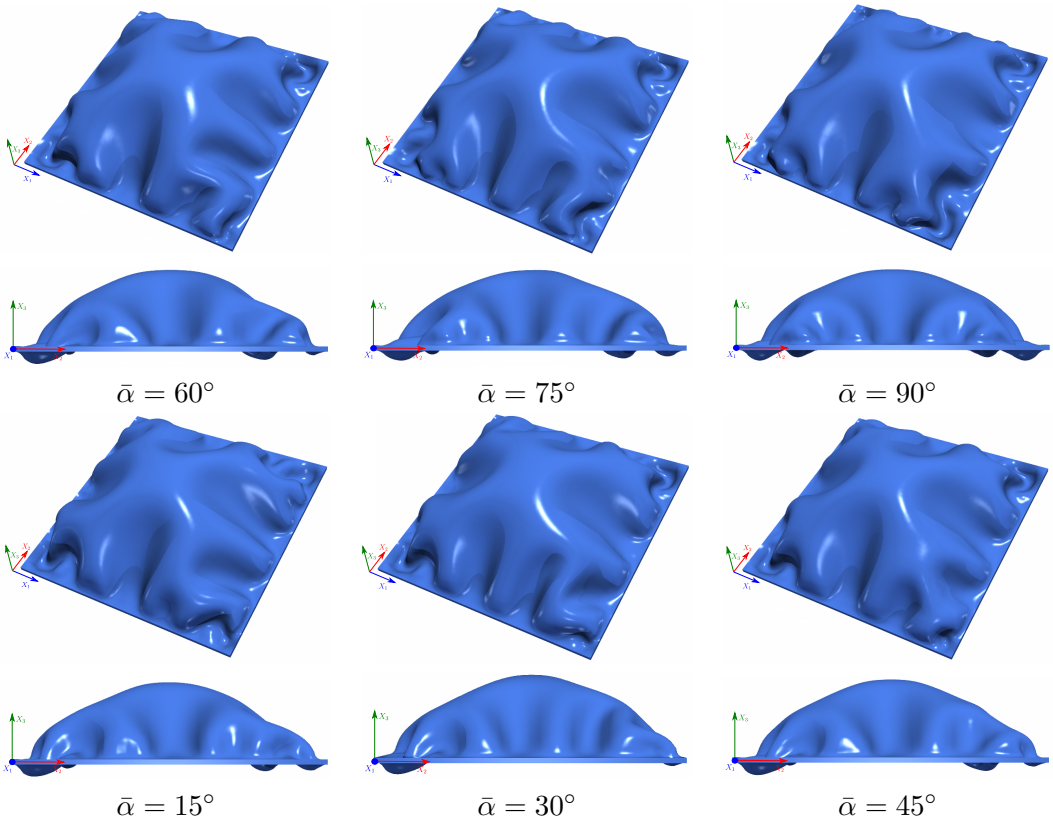

Figure 25: Numerical example 4. Different patterns of buckling for various values of $\bar{\alpha} = [15°, 30°, 45°, 60°, 75°, 90°]$ and $\bar{\beta} = 0°$. The time is $t = 290s$.

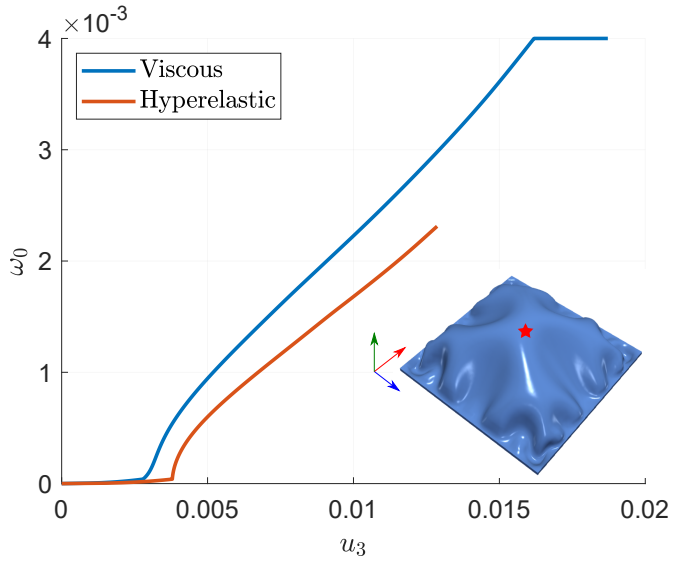

Figure 26: Numerical example 3. Increase of electric charge represented against the displacement achived by the central point of the square membrane, for the hyperelastic and viscoelastic material. The orientation of the laminate is given by $\bar{\beta} = 75°$ and $\bar{\alpha} = 30°$.

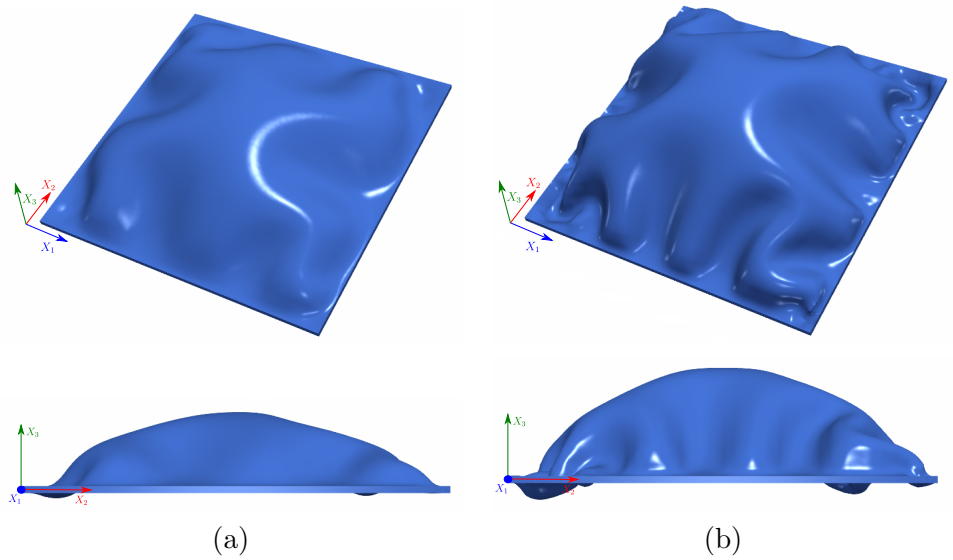

(a) (b)

Figure 27: Numerical example 3. Final deformation state for: (a) hyperelastic , (b) viscoelastic material. The orientation of the laminate is given by $\bar{\beta} = 75^{\circ}$ and $\bar{\alpha} = 30^{\circ}$.

6.3.2. Study of loss of ellipticity and convexity

Finally, a study of the possible loss of ellipticity and convexity is conducted. Figure 28 illustrates the spatial distribution of the smallest of the minors of the acoustic tensor for any unit normal orientation, namely $\mathrm{I}_{\mathrm{ellip}}$ (124), for the deformation states correspondent to three different time instances. It is ascertained that no areas of loss of ellipticity are observed, indicating that no anomalous mesh dependency effects can take place. Notwithstanding, it is observed that there are more areas with low values of the quantity $\mathrm{I}_{\mathrm{ellip}}$ when the time passes, which are formed near the corners of the square membrane.

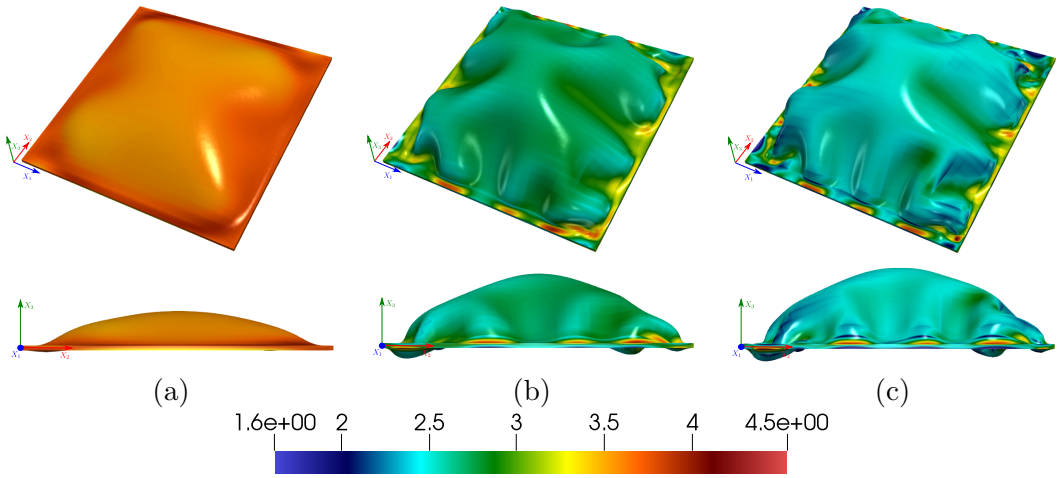

Figure 28: Numerical example 3. Contour plot of $\mathrm{I}_{\mathrm{ellip}}$ (124) for (a) $Time = 36s$, (b) $Time = 390s$, (c) $Time = 3,000s$. The orientation of the laminate is given by $\bar{\alpha} = 30°$, $\bar{\beta} = 75°$.

Likewise, Figure 29 shows a contour plot of the minimum eigenvalue of the homogenised Hessian operator of the internal energy density, $\mathrm{I}_{\mathrm{conv}}$ (128), for the same deformation states. In this case, some negative values are observed near the edges of the square membrane, indicating that loss of convexity is potentially developed, yet with no impact in the loss of ellipticity.

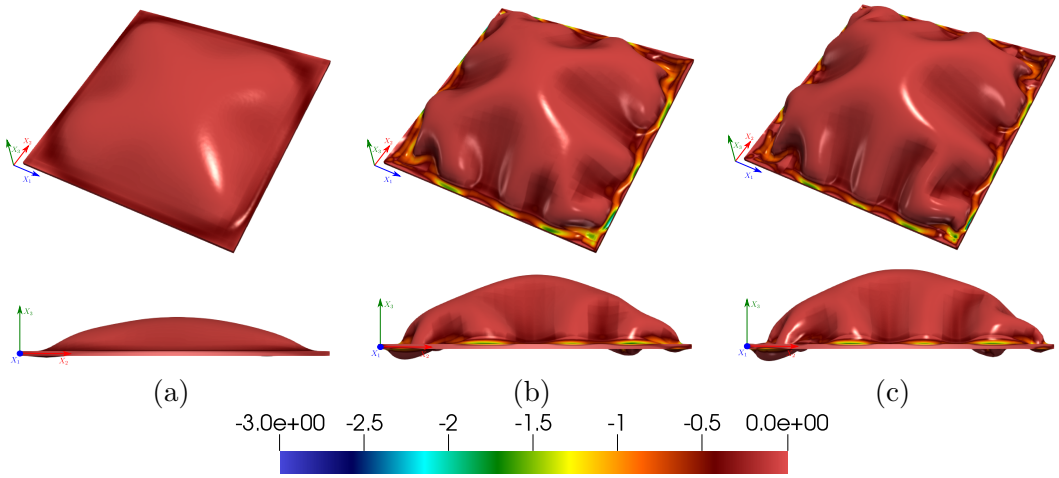

Figure 29: Numerical example 3. Contour plot of $\mathrm{I}_{\mathrm{conv}}$ (128) for (a) $Time = 36s$, (b) $Time = 390s$, (c) $Time = 3,000s$. The orientation of the laminate is given by $\bar{\alpha} = 30°$, $\bar{\beta} = 75°$.

7. Conclusions

In this paper, a new finite element based computational framework for the numerical simulation of rank-one multi-layered electro-active polymers undergoing large deformations and electric fields, with the consideration of viscoelastic effects, has been introduced. Following the well-established homogenisation strategy for rank-n laminates [22, 23], the paper exploits the use of Convex Multi-Variable (CMV) energy density functionals [34] for each of the individual material phase components in order to ensure

the existence of solutions of the microstructure problem, defined in terms of the so-called deformation gradient and electric displacement amplitude vectors $\{\boldsymbol{\alpha}, \boldsymbol{\beta}\}$. The viscoelastic properties are proved to have a regularising contribution which helps to numerically study the deformation behaviour of the rank-one laminated composite materials.

The computational strategy presented enables the exploration of very complex deformation patterns (e.g., combined bending/torsion/stretching), way beyond the onset of geometrical instabilities and without the need to assume any simplifications in the kinematics, such as plane strain or exact incompressibility. The paper includes a series of challenging numerical examples seeking to explore the performance of these composite materials at both micro and macro scales. The effect that the micro-structure composition (specifically, the orientation of the laminate) can potentially have in the response of the composite at different levels of deformation (or electric field) is studied. The effect of the viscoelasticity consideration in the material is compared in all the examples with respect to a hyperelastic (reversible) case. With this in mind, our future lines of work will include the extension of this computational framework to laminated composites of higher order as well as the consideration of possible thermal or magneto effects upon the response of the material.

8. Appendix

8.1. Thermodynamical consistency of the model

Consideration of the evolution equations in (29), in conjunction with the definition of the viscoelastic contribution $e_v\left(\boldsymbol{F}, \boldsymbol{\mathcal{A}}\right)$ in (28), permits to write the dissipation inequality $\mathcal{D}(\boldsymbol{F}, \boldsymbol{\mathcal{A}})$ in (13) as

$$\begin{aligned} \mathcal{D}(\boldsymbol{F}, \boldsymbol{\mathcal{A}}, \dot{\boldsymbol{\mathcal{A}}}) = -\partial_{\boldsymbol{\mathcal{A}}} e^v \bullet \dot{\boldsymbol{\mathcal{A}}} &= \sum_{i=1}^{n_{\text{Maxw}}} \frac{\mu_i^v}{2\tau_i^v} \text{tr}\left(\left(\boldsymbol{A}_i^{-1} - \hat{\boldsymbol{C}}\right)\left(\hat{\boldsymbol{C}}^{-1} - \boldsymbol{A}_i\right)\right) \\ &= \sum_{i=1}^{n_{\text{Maxw}}} \frac{\mu_i^v}{2\tau_i^v} \text{tr}\left(\left(\boldsymbol{I} - \boldsymbol{M}_i\right)\left(\boldsymbol{M}_i^{-1} - \boldsymbol{I}\right)\right); \qquad \boldsymbol{M}_i = \boldsymbol{A}_i \hat{\boldsymbol{C}}. \end{aligned} \tag{130}$$

Since $\hat{\boldsymbol{C}}$ is a positive definite tensor, and so is the identity tensor $\boldsymbol{I}$, the initial value problem in (29) yields positive definite internal variables $\boldsymbol{A}_i$ for every time $t \in [0, \infty)$. Furthermore, since the product of two positive definite tensors yields a positive definite tensor, this entails that both tensors $\boldsymbol{M}_i$ and its inverse $\boldsymbol{M}_i^{-1}$ are positive definite and therefore, admit the following decomposition in terms of their respective eigenvalues $\lambda_{i,\alpha}^2$ and eigenvectors $\boldsymbol{N}_{i,\alpha}$ $(\alpha = \{1, 2, 3\})$

$$\boldsymbol{M}_i = \lambda_{i,\alpha}^2 \boldsymbol{N}_{i,\alpha} \otimes \boldsymbol{N}_{i,\alpha}; \qquad \left(\boldsymbol{M}_i\right)^{-1} = \frac{1}{\lambda_{i,\alpha}^2} \boldsymbol{N}_{i,\alpha} \otimes \boldsymbol{N}_{i,\alpha}; \qquad \boldsymbol{N}_{i,\alpha} \cdot \boldsymbol{N}_{i,\beta} = \delta_{\alpha\beta}. \tag{131}$$

Making use of the decomposition of the identity tensor in terms of the eigenvectors $\boldsymbol{N}_{i,\alpha}$, namely $\boldsymbol{I} = \boldsymbol{N}_{i,\alpha} \otimes \boldsymbol{N}_{i,\alpha}$ and of the orthonormality condition in (131), the dissipation inequality can be finally written as

$$\mathcal{D}(\boldsymbol{F}, \boldsymbol{\mathcal{A}}, \dot{\boldsymbol{\mathcal{A}}}) = \sum_{i=1}^{n_{\text{Maxw}}} \frac{\mu_i^v}{2\tau_i^v} \left(\frac{1 - \lambda_{i,\alpha}^2}{\lambda_{i,\alpha}}\right)^2 \geq 0, \tag{132}$$

which proves the thermodynamical consistency of the model.

8.2. Directional derivative of the internal viscous contribution

The directional derivative of $\mathcal{D}_{\text{int},E}^v$ (45) with respect to rank-one tensors $\boldsymbol{u} \otimes \boldsymbol{V}$ yields the following additive decomposition

$$\begin{aligned} D\left(\mathcal{D}_{\text{int},E}^v\right)[\boldsymbol{u} \otimes \boldsymbol{V}] = D \underbrace{\left(\sum_{i=1}^{n_{\text{Maxw}}} \frac{\mu_i^v}{2} D(J^{-2/3}\boldsymbol{C})[\boldsymbol{u} \otimes \boldsymbol{V}] : \boldsymbol{D}_{i,n}\right)}_{\mathcal{D}_1}[\boldsymbol{u} \otimes \boldsymbol{V}] + \\ + D \underbrace{\left(\sum_{i=1}^{n_{\text{Maxw}}} \frac{\mu_i^v}{2} D(J^{-2/3}\boldsymbol{C})[\boldsymbol{u} \otimes \boldsymbol{V}] : \beta_i J^{2/3} \boldsymbol{C}^{-1}\right)}_{\mathcal{D}_2}[\boldsymbol{u} \otimes \boldsymbol{V}]. \end{aligned} \tag{133}$$

The term $\mathcal{D}_1$ in (133) can be computed as

$$\mathcal{D}_1 = \sum_{i=1}^{n_{\text{Maxw}}} \frac{\mu_i^v}{2} D(J^{-2/3}\boldsymbol{C})[\boldsymbol{u}\otimes\boldsymbol{V}] : \boldsymbol{D}_{i,n} = \sum_{i=1}^{n_{\text{Maxw}}} \frac{\mu_i^v}{2}\Big(-\frac{2}{3}J^{-5/3}\boldsymbol{C}DJ[\boldsymbol{u}\otimes\boldsymbol{V}] + J^{-2/3}D\boldsymbol{C}[\boldsymbol{u}\otimes\boldsymbol{V}]\Big) : \boldsymbol{D}_{i,n}, \tag{134}$$

from which its directional derivative $D\mathcal{D}_1[\boldsymbol{u}\otimes\boldsymbol{V}]$ is obtained as

$$\begin{aligned} D\mathcal{D}_1[\boldsymbol{u}\otimes\boldsymbol{V}] = \sum_{i=1}^{n_{\text{Maxw}}} \frac{\mu_i^v}{2}\Bigg(&\frac{10}{9}J^{-8/3}\boldsymbol{C}\left(DJ[\boldsymbol{u}\otimes\boldsymbol{V}]\right)^2 - \frac{4}{3}J^{-5/3}D\boldsymbol{C}[\boldsymbol{u}\otimes\boldsymbol{V}]DJ[\boldsymbol{u}\otimes\boldsymbol{V}] \\ &+ J^{-2/3}D^2\boldsymbol{C}[\boldsymbol{u}\otimes\boldsymbol{V};\boldsymbol{u}\otimes\boldsymbol{V}]\Bigg) : \boldsymbol{D}_{i,n}. \end{aligned} \tag{135}$$

Introducing in (135) the following notation

$$\begin{aligned} \delta J = DJ[\boldsymbol{u}\otimes\boldsymbol{V}]; \qquad & D\boldsymbol{C}[\boldsymbol{u}\otimes\boldsymbol{V}] = \delta\boldsymbol{F}^T\boldsymbol{F} + \boldsymbol{F}^T\delta\boldsymbol{F}; \\ D^2\boldsymbol{C}[\boldsymbol{u}\otimes\boldsymbol{V};\boldsymbol{u}\otimes\boldsymbol{V}] = 2\delta\boldsymbol{F}^T\delta\boldsymbol{F}; \qquad & \delta\boldsymbol{F} := \boldsymbol{u}\otimes\boldsymbol{V} \end{aligned} \tag{136}$$

permits to re-write (135) as

$$D\mathcal{D}_1[\boldsymbol{u}\otimes\boldsymbol{V}] = \sum_{i=1}^{n_{\text{Maxw}}} \frac{\mu_i^v}{2}\left(\frac{10}{9}J^{-8/3}\boldsymbol{C}\delta J^2 - \frac{4}{3}J^{-5/3}\delta J\left(\delta\boldsymbol{F}^T\boldsymbol{F} + \boldsymbol{F}^T\delta\boldsymbol{F}\right) + 2J^{-2/3}\delta\boldsymbol{F}^T\delta\boldsymbol{F}\right) : \boldsymbol{D}_{i,n}. \tag{137}$$

Careful manipulation of (137) permits to re-write it as

$$D\mathcal{D}_1[\boldsymbol{u}\otimes\boldsymbol{V}] = \sum_{i=1}^{n_{\text{Maxw}}} \frac{\mu_i^v}{J^{8/3}}\left(\frac{1}{2}\Big(\boldsymbol{M}^T\boldsymbol{M} : \boldsymbol{D}_{i,n}\Big) + \frac{1}{9}\delta J^2\left(\boldsymbol{C} : \boldsymbol{D}_{i,n}\right)\right), \tag{138}$$

where $\boldsymbol{M}$ is the second-order tensor defined as

$$\boldsymbol{M} = \frac{2\sqrt{2}}{3}\delta J\boldsymbol{F} - \sqrt{2}J\delta\boldsymbol{F} \tag{139}$$

With regards to the term $\mathcal{D}_2$ in (133), this yields

$$\begin{aligned} \mathcal{D}_2 = \sum_{i=1}^{n_{\text{Maxw}}} \frac{\mu_i^v}{2} D(J^{-2/3}\boldsymbol{C})[\boldsymbol{u}\otimes\boldsymbol{V}] : \beta_i J^{2/3}\boldsymbol{C}^{-1} &= \sum_{i=1}^{n_{\text{Maxw}}} \frac{\mu_i^v\beta_i}{2}\Big(-\frac{2}{3}J^{-5/3}\boldsymbol{C}\delta J + J^{-2/3}D\boldsymbol{C}[\boldsymbol{u}\otimes\boldsymbol{V}]\Big) : J^{2/3}\boldsymbol{C}^{-1} \\ &= \sum_{i=1}^{n_{\text{Maxw}}} \frac{\mu_i^v\beta_i}{2}\Big(-2J^{-1}\delta J + D\boldsymbol{C}[\boldsymbol{u}\otimes\boldsymbol{V}] : \boldsymbol{C}^{-1}\Big). \end{aligned} \tag{140}$$

The second term on the right-hand side of (140) can be equivalently expressed as (see equation (5))

$$D\boldsymbol{C}[\boldsymbol{u}\otimes\boldsymbol{V}] : \boldsymbol{C}^{-1} = \det\boldsymbol{C}^{-1}D\boldsymbol{C}[\boldsymbol{u}\otimes\boldsymbol{V}] : \text{Cof}\boldsymbol{C} = J^{-2}D\det\boldsymbol{C}[\boldsymbol{u}\otimes\boldsymbol{V}]. \tag{141}$$

Since $\det\boldsymbol{C} = J^2$, above equation (141) yields

$$D\boldsymbol{C}[\boldsymbol{u}\otimes\boldsymbol{V}] : \boldsymbol{C}^{-1} = J^{-2}DJ^2[\boldsymbol{u}\otimes\boldsymbol{V}] = 2J^{-1}DJ[\boldsymbol{u}\otimes\boldsymbol{V}]. \tag{142}$$

Introduction of the result in (142) into equation (140) permits to conclude that

$$\mathcal{D}_2 = 0,\ \forall\boldsymbol{F}; \Rightarrow D\mathcal{D}_2[\boldsymbol{u}\otimes\boldsymbol{V}] = 0. \tag{143}$$

9. Acknowledgements

Project supported by the Autonomous Community of the Region of Murcia through the program for the development of scientific and technical research by competitive groups (20911/PI/18), included in the Regional Program for the Promotion of Scientific and Technical Research of Fundación Séneca - Agencia de Ciencia y Tecnología de la Región de Murcia. The first author also acknowledges the support provided by Fundación Séneca - Agencia de Ciencia y Tecnología de la Región de Murcia, for the award of a Postdoc Fellowship with reference 20818/PD/18. The third author also acknowledges the support provided by Ministerio de Ciencia, Innovación y Universidades, for the award of a Juan de la Cierva Formación Fellowship, and by Fundación Séneca - Agencia de Ciencia y Tecnología de la Región de Murcia, through the contract with reference number 21132/SF/19 under the program "Subprograma Regional Saavedra Fajardo de Incorporacion de Doctores a Universidades y Centros de Investigacion de la Region De Murcia". The fourth author acknowledges the financial support received through the European Training Network Protechtion (Project ID: 764636).

References

[1] D. Ahmad and K. Patra. Experimental and theoretical analysis of laterally pre-stretched pure shear deformation of dielectric elastomer. *Polymer Testing*, 75:291–297, 2019.

[2] A. Ask, A. Menzel, and M. Ristinmaa. Electrostriction in electro-viscoelastic polymers. *Mechanics of Materials*, 50:9–21, 2012.

[3] A. Ask, A. Menzel, and M. Ristinmaa. Phenomenological modeling of viscous electrostrictive polymers. *International Journal of Non-Linear Mechanics*, 47(2):156–165, 2012.

[4] J. M. Ball. Convexity conditions and existence theorems in nonlinear elasticity. *Arch Ration Mech Anal*, 63(4):337–403, 1976.

[5] J. M. Ball. Some open problems in elasticity. In *Geometry, Mechanics, and Dynamics*, pages 3–59. Springer-Verlag, 2002.

[6] Y. Bar-Cohen. *EAP history, current status, and infrastructure in Y. Bar-Cohen, Electroactive Polymer (EAP) Actuators as Artificial Muscles*, chapter 1, pages 3–44. SPIE press, 2001.

[7] Y. Bar-Cohen. Electroactive polymers (EAP) as actuators for potential future planetary mechanisms. In *Proceedings. NASA/DoD Conference on Evolvable Hardware, 2004.* IEEE, 2004.

[8] K. Bertoldi and M. Gei. Instabilities in multilayered soft dielectrics. *J Mech Phys Solids*, 59(1): 18–42, 2011.

[9] D. Bishara and M. Jabareen. A reduced mixed finite-element formulation for modeling the viscoelastic response of electro-active polymers at finite deformation. *Mathematics and Mechanics of Solids*, 24(5):1578–1610, 2018.

[10] J. Bonet, A. J. Gil, and R. Ortigosa. On a tensor cross product based formulation of large strain solid mechanics. *International Journal of Solids and Structures*, 84:49–63, 2016.

[11] J. Bonet, A. J. Gil, and R. D. Wood. *Nonlinear Solid Mechanics for Finite Element Analysis: Statics*. Cambridge University Press, 2016. ISBN 1107115795.

[12] E. Bortot, R. Denzer, A. Menzel, and M. Gei. Analysis of viscoelastic soft dielectric elastomer generators operating in an electrical circuit. *Int J Solids Struct*, 78-79:205–215, 2016.

[13] A. Büschel, S. Klinkel, and W. Wagner. Dielectric elastomers - numerical modeling of nonlinear visco-electroelasticity. *International Journal for Numerical Methods in Engineering*, pages n/a–n/a, 2012.

[14] R. Bustamante. Transversely isotropic non-linear electro-active elastomers. *Acta Mech*, 206(3-4): 237–259, 2008.

[15] F. Carpi, D. De Rossi, R. Kornbluh, R. Pelrine, and P. Sommer-Larsen. *Dielectric Elastomers as Electromechanical Transducers*. Elsevier, 2008.

[16] F. Carpi, G. Frediani, S. Turco, and D. De Rossi. Bioinspired tunable lens with muscle-like electroactive elastomers. *Adv Funct Mater*, 21(21):4152–4158, 2011.

[17] R. M. Christensen. A nonlinear theory of viscoelasticity for application to elastomers. *Journal of Applied Mechanics*, 47(4):762–768, 1980.

[18] B. D. Coleman and W. Noll. Foundations of linear viscoelasticity. *Reviews of Modern Physics*, 33 (2):239–249, 1961.

[19] B. D. Coleman and W. Noll. The thermodynamics of elastic materials with heat conduction and viscosity. *Archive for Rational Mechanics and Analysis*, 13(1):167–178, 1963.

[20] R. de Boer. *Vektor-und Tensorrechnung für Ingenieure*. Springer-Verlag, 1982.

[21] E. A. de Souza Neto, D. Peri, and D. R. J. Owen. *Computational Methods for Plasticity*. John Wiley & Sons, Ltd, 2008.

[22] G. deBotton and I. Hariton. High-rank nonlinear sequentially laminated composites and their possible tendency towards isotropic behavior. *J Mech Phys Solids*, 50(12):2577–2595, 2002.

[23] G. deBotton, L. Tevet-Deree, and E. A. Socolsky. Electroactive heterogeneous polymers: Analysis and applications to laminated composites. *Mech Adv Mater Struct*, 14(1):13–22, 2007.

[24] G. deBotton. Transversely isotropic sequentially laminated composites in finite elasticity. *J Mech Phys Solids*, 53(6):1334–1361, 2005.

[25] G. deBotton and L. Tevet-Deree. Electroactive polymer composites: analysis and simulation. In W. D. Armstrong, editor, *Smart Structures and Materials 2006: Active Materials: Behavior and Mechanics*. SPIE, 2006.

[26] A. Dorfmann and R. W. Ogden. Nonlinear electroelasticity. *Acta Mech*, 174(3-4):167–183, 2005.

[27] A. Dorfmann and R. W. Ogden. Nonlinear electroelastic deformations. *J Elast*, 82(2):99–127, 2006.

[28] M. Franke, R. Ortigosa, A. Janz, A. Gil, and P. Betsch. A mixed variational framework for the design of energy–momentum integration schemes based on convex multi-variable electro-elastodynamics. *Comput Methods Appl Mech Eng*, 351:109–152, 2019.

[29] J. Furer and P. Ponte Castañeda. Macroscopic instabilities and domain formation in neo-hookean laminates. *Journal of the Mechanics and Physics of Solids*, 118:98–114, 2018.

[30] G. Gallone, F. Galantini, and F. Carpi. Perspectives for new dielectric elastomers with improved electromechanical actuation performance: composites versus blends. *Polym Int*, 59(3):400–406, 2010.

[31] D. Garcia-Gonzalez. Magneto-visco-hyperelasticity for hard-magnetic soft materials: theory and numerical applications. *Smart Materials and Structures*, 28(8):085020, 2019.

[32] M. Gei and K. C. Mutasa. Optimisation of hierarchical dielectric elastomer laminated composites. *Int J Non Linear Mech*, 106:266–273, 2018.

[33] M. Gei, R. Springhetti, and E. Bortot. Performance of soft dielectric laminated composites. *Smart Mater Struct*, 22(10):104014, 2013.

[34] A. J. Gil and R. Ortigosa. A new framework for large strain electromechanics based on convex multi-variable strain energies: Variational formulation and material characterisation. *Computer Methods in Applied Mechanics and Engineering*, 302:293–328, 2016.

[35] O. Gonzalez and A. M. Stuart. *A First Course in Continuum Mechanics*. Cambridge University Press, 2001.

[36] A. Goshkoderia and S. Rudykh. Electromechanical macroscopic instabilities in soft dielectric elastomer composites with periodic microstructures. *Eur J Mech A Solids*, 65:243–256, 2017.

[37] A. E. Green, R. S. Rivlin, and A. J. M. Spencer. The mechanics of non-linear materials with memory. *Archive for Rational Mechanics and Analysis*, 3(1):82–90, 1959.

[38] M. S. Green and A. V. Tobolsky. A new approach to the theory of relaxing polymeric media. *The Journal of Chemical Physics*, 14(2):80–92, 1946.

[39] T. He and Z. Wang. Electro-viscoelastic performance of a tubular dielectric elastomer actuator. *International Journal of Mechanics and Materials in Design*, 15(2):199–212, 2018.

[40] W. Hong. Modeling viscoelastic dielectrics. *Journal of the Mechanics and Physics of Solids*, 59(3): 637–650, 2011.

[41] M. Hossain, D. K. Vu, and P. Steinmann. Experimental study and numerical modelling of VHB 4910 polymer. *Computational Materials Science*, 59:65–74, 2012.

[42] M. Hossain, D. K. Vu, and P. Steinmann. A comprehensive characterization of the electro-mechanically coupled properties of VHB 4910 polymer. *Archive of Applied Mechanics*, 85(4): 523–537, 2014.

[43] C. Huang and Q. Zhang. Enhanced dielectric and electromechanical responses in high dielectric constant all-polymer percolative composites. *Adv Funct Mater*, 14(5):501–506, 2004.

[44] C. Huang, Q. M. Zhang, G. deBotton, and K. Bhattacharya. All-organic dielectric-percolative three-component composite materials with high electromechanical response. *Appl Phys Lett*, 84 (22):4391–4393, 2004.

[45] M. Itskov and V. N. Khiêm. A polyconvex anisotropic free energy function for electro- and magneto-rheological elastomers. *Mathematics and Mechanics of Solids*, 21(9):1126–1137, 2016.

[46] M. Jabareen. On the modeling of electromechanical coupling in electroactive polymers using the mixed finite element formulation. *Procedia IUTAM*, 12:105–115, 2015.

[47] C. Kadapa and M. Hossain. A robust and computationally efficient finite element framework for coupled electromechanics. *Computer Methods in Applied Mechanics and Engineering*, 372:113443, 2020.

[48] G. Kofod. *Dielectric elastomer actuators : Ph.D. thesis*. Risø DTU - National Laboratory for Sustainable Energy available from Risø National Laboratory, Information Service Department, City, 2001. ISBN 8755029256.

[49] R. D. Kornbluh, R. Pelrine, Q. Pei, S. Oh, and J. Joseph. Ultrahigh strain response of field-actuated elastomeric polymers. In Y. Bar-Cohen, editor, *Smart Structures and Materials 2000: Electroactive Polymer Actuators and Devices (EAPAD)*. SPIE, 2000.

[50] R. D. Kornbluh, R. Pelrine, H. Prahlad, A. Wong-Foy, B. McCoy, S. Kim, J. Eckerle, and T. Low. From boots to buoys: promises and challenges of dielectric elastomer energy harvesting. In Y. Bar-Cohen and F. Carpi, editors, *Electroactive Polymer Actuators and Devices (EAPAD) 2011*. SPIE, 2011.

[51] B. Kussmaul, S. Risse, G. Kofod, R. Waché, M. Wegener, D. N. McCarthy, H. Krüger, and R. Gerhard. Enhancement of dielectric permittivity and electromechanical response in silicone elastomers: Molecular grafting of organic dipoles to the macromolecular network. *Adv Funct Mater*, 21(23):4589–4594, 2011.

[52] S. P. Lacour, H. Prahlad, R. Pelrine, and S. Wagner. Mechatronic system of dielectric elastomer actuators addressed by thin film photoconductors on plastic. *Sens Actuators, A*, 111(2-3):288–292, 2004.

[53] J. Y. Li, C. Huang, and Q. Zhang. Enhanced electromechanical properties in all-polymer percolative composites. *Appl Phys Lett*, 84(16):3124–3126, 2004.

[54] J. Li. Exchange coupling in p(VDF-TrFE) copolymer based all-organic composites with giant electrostriction. *Phys Rev Lett*, 90(21), 2003.

[55] T. Li, C. Keplinger, R. Baumgartner, S. Bauer, W. Yang, and Z. Suo. Giant voltage-induced deformation in dielectric elastomers near the verge of snap-through instability. *J Mech Phys Solids*, 61(2):611–628, 2013.

[56] Z. Liao, M. Hossain, X. Yao, M. Mehnert, and P. Steinmann. On thermo-viscoelastic experimental characterization and numerical modelling of VHB polymer. *International Journal of Non-Linear Mechanics*, 118:103263, 2020.

[57] J. Lubliner. A model of rubber viscoelasticity. *Mechanics Research Communications*, 12(2):93–99, 1985.

[58] F. Marín, J. Martínez-Frutos, R. Ortigosa, and A. Gil. A convex multi-variable based computational framework for multilayered electro-active polymers. *Computer Methods in Applied Mechanics and Engineering*, 374:113567, 2021.

[59] T. McKay, B. O'Brien, E. Calius, and I. Anderson. An integrated, self-priming dielectric elastomer generator. *Appl Phys Lett*, 97(6):062911, 2010.

[60] R. M. McMeeking and C. M. Landis. Electrostatic forces and stored energy for deformable dielectric materials. *J Appl Mech*, 72(4):581–590, 2004.

[61] M. Mehnert and P. Steinmann. On the influence of the compliant electrodes on the mechanical behavior of VHB 4905. *Computational Materials Science*, 160:287–294, 2019.

[62] M. Mehnert, M. Hossain, and P. Steinmann. Numerical modeling of thermo-electro-viscoelasticity with field-dependent material parameters. *International Journal of Non-Linear Mechanics*, 106: 13–24, 2018.

[63] M. Mehnert, M. Hossain, and P. Steinmann. Experimental and numerical investigations of the electro-viscoelastic behavior of VHB 4905tm. *European Journal of Mechanics - A/Solids*, 77: 103797, 2019.

[64] C. Miehe, D. Vallicotti, and D. Zäh. Computational structural and material stability analysis in finite electro-elasto-statics of electro-active materials. *International Journal for Numerical Methods in Engineering*, 102(10):1605–1637, 2015.

[65] M. Molberg, D. Crespy, P. Rupper, F. Nüesch, J.-A. E. Månson, C. Löwe, and D. M. Opris. High breakdown field dielectric elastomer actuators using encapsulated polyaniline as high dielectric constant filler. *Adv Funct Mater*, 20(19):3280–3291, 2010.

[66] A. O'Halloran, F. O'Malley, and P. McHugh. A review on dielectric elastomer actuators, technology, applications, and challenges. *J Appl Phys*, 104(7):071101, 2008.

[67] R. Ortigosa and A. J. Gil. A new framework for large strain electromechanics based on convex multi-variable strain energies: Conservation laws, hyperbolicity and extension to electro-magneto-mechanics. *Comput Methods Appl Mech Eng*, 309:202–242, 2016.

[68] R. Ortigosa and A. J. Gil. A new framework for large strain electromechanics based on convex multi-variable strain energies: Finite element discretisation and computational implementation. *Comput Methods Appl Mech Eng*, 302:329–360, 2016.

[69] R. Ortigosa and A. J. Gil. A computational framework for incompressible electromechanics based on convex multi-variable strain energies for geometrically exact shell theory. *Computer Methods in Applied Mechanics and Engineering*, 317:792–816, 2017.

[70] R. Ortigosa, A. J. Gil, and C. H. Lee. A computational framework for large strain nearly and truly incompressible electromechanics based on convex multi-variable strain energies. *Comput Methods Appl Mech Eng*, 310:297–334, 2016.

[71] R. Pelrine. High-speed electrically actuated elastomers with strain greater than 100%. *Science*, 287(5454):836–839, 2000.

[72] R. E. Pelrine, R. D. Kornbluh, and J. P. Joseph. Electrostriction of polymer dielectrics with compliant electrodes as a means of actuation. *Sens Actuators, A*, 64(1):77–85, 1998.

[73] S. T. J. Peng, K. C. Valanis, and R. F. Landel. Nonlinear viscoelasticity and relaxation phenomena of polymer solids. *Acta Mechanica*, 25(3-4):229–240, 1977.

[74] P. Ponte Castañeda and M. Siboni. A finite-strain constitutive theory for electro-active polymer composites via homogenization. *Int J Non Linear Mech*, 47(2):293–306, 2012.

[75] R. Poya, A. J. Gil, R. Ortigosa, R. Sevilla, J. Bonet, and W. A. Wall. A curvilinear high order finite element framework for electromechanics: From linearised electro-elasticity to massively deformable dielectric elastomers. *Comput Methods Appl Mech Eng*, 329:75–117, 2018.

[76] S. Risse, B. Kussmaul, H. Krüger, and G. Kofod. Synergistic improvement of actuation properties with compatibilized high permittivity filler. *Adv Funct Mater*, 22(18):3958–3962, 2012.

[77] S. Rudykh, K. Bhattacharya, and G. deBotton. Multiscale instabilities in soft heterogeneous dielectric elastomers. *Proceedings of the Royal Society A: Mathematical, Physical and Engineering Sciences*, 470(2162):20130618, 2014.

[78] S. Rudykh and G. deBotton. Stability of anisotropic electroactive polymers with application to layered media. *Zeitschrift für angewandte Mathematik und Physik*, 62(6):1131–1142, 2011.

[79] S. Rudykh, K. Bhattacharya, and G. deBotton. Snap-through actuation of thick-wall electroactive balloons. *Int J Non Linear Mech*, 47(2):206–209, 2012.

[80] S. Rudykh, A. Lewinstein, G. Uner, and G. deBotton. Analysis of microstructural induced enhancement of electromechanical coupling in soft dielectrics. *Appl Phys Lett*, 102(15):151905, 2013.

[81] P. Saxena, M. Hossain, and P. Steinmann. A theory of finite deformation magneto-viscoelasticity. *International Journal of Solids and Structures*, 50(24):3886–3897, 2013.

[82] P. Saxena, M. Hossain, and P. Steinmann. Nonlinear magneto-viscoelasticity of transversally isotropic magneto-active polymers. *Proceedings of the Royal Society A: Mathematical, Physical and Engineering Sciences*, 470(2166):20140082, 2014.

[83] R. A. Schapery. On the characterization of nonlinear viscoelastic materials. *Polymer Engineering and Science*, 9(4):295–310, 1969.

[84] J. Schröder, P. Neff, and D. Balzani. A variational approach for materially stable anisotropic hyperelasticity. *International Journal of Solids and Structures*, 42(15):4352–4371, 2005.

[85] J. Schröder and P. Neff. Invariant formulation of hyperelastic transverse isotropy based on polyconvex free energy functions. *Int J Solids Struct*, 40(2):401–445, 2003.

[86] S. Seifi, K. Park, and H. S. Park. A staggered explicit–implicit finite element formulation for electroactive polymers. *Computer Methods in Applied Mechanics and Engineering*, 337:150–164, 2018.

[87] A. K. Sharma and M. Joglekar. A computationally efficient locking free numerical framework for modeling visco-hyperelastic dielectric elastomers. *Computer Methods in Applied Mechanics and Engineering*, 352:625–653, 2019.

[88] A. K. Sharma and M. Joglekar. A numerical framework for modeling anisotropic dielectric elastomers. *Computer Methods in Applied Mechanics and Engineering*, 344:402–420, 2019.

[89] M. Šilhavý. A variational approach to nonlinear electro-magneto-elasticity: Convexity conditions and existence theorems. *Mathematics and Mechanics of Solids*, 23(6):907–928, 2017.

[90] H. Stoyanov, M. Kollosche, S. Risse, D. N. McCarthy, and G. Kofod. Elastic block copolymer nanocomposites with controlled interfacial interactions for artificial muscles with direct voltage control. *Soft Matter*, 7(1):194–202, 2011.

[91] Z. Suo, X. Zhao, and W. Greene. A nonlinear field theory of deformable dielectrics. *J Mech Phys Solids*, 56(2):467–486, 2008.

[92] L. Tian, L. Tevet-Deree, G. deBotton, and K. Bhattacharya. Dielectric elastomer composites. *J Mech Phys Solids*, 60(1):181–198, 2012.

[93] R. A. Toupin. Stress tensors in elastic dielectrics. *Arch Ration Mech Anal*, 5(1):440–452, 1960.

[94] R. Toupin. The elastic dielectric. *Indiana Univ. Math. J.*, 5:849–915, 1956. ISSN 0022-2518.

[95] F. Vogel, S. Göktepe, P. Steinmann, and E. Kuhl. Modeling and simulation of viscous electro-active polymers. *European Journal of Mechanics - A/Solids*, 48:112–128, 2014.

[96] D. K. Vu, P. Steinmann, and G. Possart. Numerical modelling of non-linear electroelasticity. *Int J Numer Methods Eng*, 70(6):685–704, 2007.

[97] D. Vu and P. Steinmann. Material and spatial motion problems in nonlinear electro- and magneto-elastostatics. *Mathematics and Mechanics of Solids*, 15(2):239–257, 2009.

[98] D. Vu and P. Steinmann. On 3-d coupled BEM–FEM simulation of nonlinear electro-elastostatics. *Comput Methods Appl Mech Eng*, 201-204:82–90, 2012.

[99] D. Vu and P. Steinmann. On the spatial and material motion problems in nonlinear electro-elastostatics with consideration of free space. *Mathematics and Mechanics of Solids*, 17(8):803–823, 2012.

[100] H. Wang. Viscoelastic analysis of a spring-connected dielectric elastomer actuator undergoing large inhomogeneous deformation. *International Journal of Mechanical Sciences*, 136:17–23, 2018.

[101] S. Wang, M. Decker, D. L. Henann, and S. A. Chester. Modeling of dielectric viscoelastomers with application to electromechanical instabilities. *Journal of the Mechanics and Physics of Solids*, 95: 213–229, 2016.

[102] M. Wissler and E. Mazza. Modeling and simulation of dielectric elastomer actuators. *Smart Materials and Structures*, 14(6):1396–1402, 2005.

[103] M. Wissler and E. Mazza. Mechanical behavior of an acrylic elastomer used in dielectric elastomer actuators. *Sensors and Actuators A: Physical*, 134(2):494–504, 2007.

[104] T. Wissler. *Modeling dielectric elastomer actuators*. PhD thesis, Swiss Federal Institute of Technology in Zurich, 2007.

[105] E. Yarali, M. Baniasadi, M. Bodaghi, and M. Baghani. 3d constitutive modeling of electro-magneto-visco-hyperelastic elastomers: a semi-analytical solution for cylinders under large torsion–extension deformation. *Smart Materials and Structures*, 29(8):085031, 2020.

[106] Q. M. Zhang, H. Li, M. Poh, F. Xia, Z.-Y. Cheng, H. Xu, and C. Huang. An all-organic composite actuator material with a high dielectric constant. *Nature*, 419(6904):284–287, 2002.

[107] X. Zhao, S. J. A. Koh, and Z. Suo. Nonequilibrium Thermodynamics of dielectric elastomers. *International Journal of Applied Mechanics*, 03(02):203–217, 2011.